X-ray diffraction from single GaAs nanowires

DISSERTATION
zur Erlangung des Grades eines Doktors
der Naturwissenschaften

vorgelegt von
M. Sc. Andreas Biermanns

eingereicht bei der Naturwissenschaftlich-Technischen Fakultät
der Universität Siegen

Siegen 2012

Gutachter:
Prof. Dr. Ullrich Pietsch
Prof. Dr. Robert Feidenhans'l

Tag der mündlichen Prüfung:
12. November 2012

Gedruckt auf alterungsbeständigem holz- und säurefreiem Papier.

Zusammenfassung

Die Entwicklung neuartiger optischer Komponenten für harte Röntgenstrahlung hat es in den letzten Jahren ermöglicht, hoch intensive, kohärente Röntgenstrahlen mit Durchmessern von 100 nm und darunter zu erzeugen. Zusammen mit der Entwicklung neuer experimenteller Aufbauten sind so nun zerstörungsfreie Röntgenbeugungsexperimente an einzelnen Nanoobjekten möglich.

In der vorliegenden Arbeit werden eine Reihe von Aspekten beim epitaktischen Wachstum von Halbleiter-Nanodrähten mittels Röntgenbeugung untersucht. Besonderes Augenmerk liegt dabei auf der Anwendung neuartiger Methoden der „Nanobeugung“, um einzelne Nanodrähte zu untersuchen.

In einem ersten Schritt wird die Methode der kohhärenten Röntgenbeugung benutzt, um gleichzeitig die Gitterparameter und die 3-dimensionale Form einzelner Galliumarsenid Nanodrähte zu bestimmen, die mittels metallorganischer Gasphasenepitaxie gewachsen wurden. Auf Grund einer hohen Dichte von Rotationszwillingen in der Zinkblende-Struktur des Kristallgitters kommt es zu einer systematischen Abweichung der Gitterparameter im Vergleich zu GaAs Volumenkristallen.

In einem zweiten Beispiel wird insbesondere das Anfangsstadium im selbstassistierten Wachstum von GaAs Nanodrähten auf Silizium (1 1 1) Oberflächen untersucht. Diese mittels Molekularstrahlepitaxie erzeugten GaAs Drähte wachsen vorwiegend in der kubischen Zinkblende-Struktur. Jedoch finden sich Abschnitte der hexagonalen Wurtzit-Struktur kurz oberhalb der Grenzfläche der Drähte zum Substrat, deren exakte Position mittels Nanobeugung bestimmt werden konnte. Da das Kristallgitter von GaAs einen um 4% größeren Gitterparameter besitzt als Silizium, kommt es zu Verspannungen an der Grenzfläche, welche durch den Einschluss von Versetzungen an der Grenzfläche abgebaut werden. Während bei Nanodrähten mit Durchmessern über 100 nm der Abbau der Verspannung komplett durch diese Versetzungen erfolgt, verhindert eine raue Grenzfläche zum Substrat bei Drahtdurchmessern oberhalb von 100 nm eine vollständige Relaxation, so dass ein Teil der Verspannung elastisch entlang der Wachstumsrichtung abgebaut wird.

Zuletzt werden erste experimentelle Ergebnisse zur Relaxation in GaAs - InAs „core-shell“ Nanodraht Heterostrukturen dargestellt und behandelt. In diesem System führt ein unvollständiger plastischer Abbau der Verspannung an der Grenzfläche zu einer elastischen Wechselwirkung zwischen GaAs Kern und InAs Hülle, welche eine signifikante Verzerrung des Kristallgitters im GaAs Kern mit ansteigender Dicke der InAs Hülle hervorruft.

Abstract

In recent years, developments in x-ray focussing optics have allowed to produce highly intense, coherent x-ray beams with spot sizes in the range of 100 nm and below. Together with the development of new experimental stations, x-ray diffraction techniques can now be applied to study single nanometer-sized objects.

In the present work, x-ray diffraction is applied to study different aspects of the epitaxial growth of GaAs nanowires. Besides conventional diffraction methods, which employ x-ray beams with dimensions of several tens of μm, special emphasis lies on the use of nanodiffraction methods which allow to study single nanowires in their as-grown state without further preparation.

In particular, coherent x-ray diffraction is applied to measure simultaneously the 3-dimensional shape and lattice parameters of GaAs nanowires grown by metal-organic vapor phase epitaxy. It is observed that due to a high density of zinc-blende rotational twins within the nanowires, their lattice parameter deviates systematically from the bulk zinc-blende phase.

In a second step, the initial stage in the growth of GaAs nanowires on Si (1 1 1) surfaces is studied. This nanowires, obtained by Ga-assisted growth in molecular beam epitaxy, grow predominantly in the cubic zinc-blende structure, but contain inclusions of the hexagonal wurtzite phase close to their bottom interface. Using nanodiffraction methods, the position of the different structural units along the growth axis is determined. Because the GaAs lattice is 4% larger than silicon, these nanowires release their lattice mismatch by the inclusion of dislocations at the interface. Whereas NWs with diameters below 50 nm are free of strain, a rough interface structure in nanowires with diameters above 100 nm prevents a complete plastic relaxation, leading to a residual strain at the interface that decays elastically along the growth direction.

Finally, measurements on GaAs-core / InAs-shell nanowire heterostructures are presented. In this system, a saturation of the dislocation density at the core-shell interface causes residual stresses at the heterojunction and significant strain in the GaAs core, increasing with the thickness of the InAs shell.

Contents

Glossary

The following abbreviations are used throughout the text

CTR	crystal truncation rod
FEM	finite element method
FWHM	full width at half maximum
FZP	Fresnel zone plate
GID	grazing incidence diffraction
HS	heterostructure
MBE	molecular beam epitaxy
ML	monolayer
MOVPE	metal-organic vapor phase epitaxy
NW	nanowire
RSM	reciprocal space map
SEM	scanning electron microscopy
(HR) TEM	(high resolution) transmission electron microscopy
VLS	vapor liquid solid growth mechanism
WZ	wurtzite crystal structure
XRD	x-ray diffraction
ZB	zinc-blende crystal structure
[**h k l**]	crystallographic direction
(**h k l**)	lattice plane or corresponding Bragg reflection
{**h k l**}	set of equivalent lattice planes or Bragg reflections
(**hkl**)$^{\mathbf{c}}$	^{c} denotes the cubic coordinate system
(**hkl**)$^{\mathbf{h}}$	^{h} denotes the hexagonal surface coordinate system
(**hkl**)$^{\mathbf{WZ}}$	^{WZ} denotes the hexagonal wurtzite coordinate system

1 Introduction

Semiconductor nanowires (NWs) are promising candidates for the fabrication of future electronic or optoelectronic devices and have attracted increasing interest in recent years [149]. Amongst others, possible applications range from light emitting diodes [138] and NW lasers [58, 148], over photovoltaic applications in solar cells [48] to electronic devices like field effect transistors [135, 26] or even sensors for gases [101] or proteins [153]. Using different growth techniques, it is possible to grow a large variety of nanowires on different substrates. However, many fundamental aspects of nanowire growth are not fully understood yet, and major drawbacks remain to be solved.

A first challenge is the control of the nanowires crystal structure. Many nanowires, e.g. from group III-V materials, grow along the cubic [1 1 1] direction, and due to only small energetic differences during growth, commonly cubic zincblende and hexagonal wurtzite crystal structures are observed which frequently mix in individual nanowires [51, 34]. Although remarkable control on crystal structure has been obtained in specific systems and special growth conditions, a general understanding of factors influencing this polytypism is missing.

A second unresolved issue is the fabrication of epitaxial, free-standing nanowires on allocated positions on the substrate together with a control on the nanowire dimensions. Commonly, nanowires grow after the initial self-organized formation of catalytic particles, whose positions and sizes vary and can only be controlled to a certain extend, leading to a similar spread in NW position and dimensions. Depending on the growth mechanism, a high level of control can be obtained by the use of structured masks that are deposited on the surface of the substrate [56, 2, 103, 110], or the controlled deposition of catalytic particles [35, 13]. However, both methods are technically demanding and may lead to specific changes in the growth conditions of the nanowires.

Finally, the formation of heterostructures in nanowires is not fully understood and the fabrication of defect free, sharp heterointerfaces in nanowires is a major challenge for the production of future devices[10, 68]. This relates both to heterointerfaces within nanowires, but also to the interface between the nanowires and the underlying substrate, in particular if both are made of highly lattice mismatched materials. In fact, the combinations of highly lattice mismatched materials in a nanowire geometry is one of the driving forces for the increasing interest in NW growth, as it is expected that the NW geometry allows to relieve strains more effectively by elastic deformations compared to thin film growth, leading to an increase of the critical thicknesses for pseudomorphic integration of devices [50, 152].

Common tools to study the morphology and structure of nanowires are scanning- and transmission electron microscopy. Whereas SEM gives fast access to the size and shape of NWs and their distribution on the surface, TEM can be used to map the crystal structure of selected NWs or chemical compositions and strains along interfaces [77, 137, 33]. However, the detection of small strains in TEM is difficult, and the destructive method usually allows to study a limited number of NWs only. In addition, due to the destructive nature the simultaneous determination of size and shape becomes difficult.

Alternatively, x-ray diffraction can be used to study crystal structures and strains in nanowires [85, 41, 71, 83, 40, 84, 74]. In addition, time-resolved diffraction experiments have been used to measure vibrational modes of NWs and to address their mechanical behavior [82]. However, whereas conventional techniques use a broad x-ray beam and allow to study large ensembles of nanowires simultaneously, the fluctuation of both structure and size of different NWs grown simultaneously leads to an unavoidable averaging of structural information[66]. Recent developments in x-ray optics and instrumentation have allowed to produce x-ray beams with focal sizes in the order of 100 nm and below, and enable to perform diffraction experiments on single nanostructures[96, 18, 122, 32, 42, 43]. Because this new method of nanodiffraction allows to probe the morphology of the diffracting objects simultaneously with the crystal structure and lattice strains, nanodiffraction does not suffer from the broadening of diffraction signals usually observed in ensembles with varying sizes.

Aim of this work is the application of x-ray diffraction methods for the characterization semiconductor nanowires, with emphasis on the use of nano-focussed x-ray beams. In different examples, the method will be applied to address different questions in the growth of GaAs nanowires.

In particular, coherent x-ray diffraction will be applied to measure simultaneously the 3dimensional shape and lattice parameters of individual GaAs nanowires grown by metal-organic vapor phase epitaxy in a patterned array. Here, we will address differences between different NWs grown simultaneously under identical conditions, and observe how a high density of growth faults can change the average lattice parameter of the nanowires. Secondly, we will study the initial stage in GaAs nanowire growth on Si (1 1 1) substrates using a Ga-assisted growth mechanism in molecular beam epitaxy. We will determine how the lattice parameter difference between silicon and GaAs is accommodated in the beginning of growth and follow the structural evolution of the nanowires. Finally, as an outlook first measurements on the strain distribution and relaxation process in GaAs-core / InAs-shell nanowire heterostructures will be discussed.

The text is structured as follows: In chapter 2, the epitaxial growth of semiconductor nanowires will be reviewed, together with their crystal structures and known structural properties. In chapter 3, the used x-ray diffraction methods are introduced, together with the experimental instrumentation and imposed limitations by the use of x-ray nanodiffraction. In chapters 4 - 6, the different aspects of nanowire growth discussed above will be addressed and summarized in chapter 7.

List of own publications

Most of the results summarized in this thesis have been published before in separate articles. This list gives an overview of the articles related to this thesis as well as other articles which are not directly covered here or related to other topics.

Principal publications related to this work

[I] A. Biermanns, A. Davydok, H. Paetzelt, A. Diaz, V. Gottschalch, T. H. Metzger and U. Pietsch, *Individual GaAs nanorods imaged by coherent X-ray diffraction*
Journal of Synchrotron Radiation **16**, 796 (2009) (chapter 4.3)

[II] A. Biermanns, S. Breuer, A. Davydok, L. Geelhaar and U. Pietsch, *Structural evolution of self-assisted GaAs nanowires grown on Si(111)*
Physica Status Solidi RRL **5**, 156 (2011) (chapter 5.3)

[III] A. Biermanns, S. Breuer, A. Davydok, L. Geelhaar and U. Pietsch, *Structural polytypism and residual strain in GaAs nanowires grown on Si(111) probed by single-nanowire x-ray diffraction*
Journal of Applied Crystallography **45**, 239 (2012) (chapters 5.5 / 5.6)

[IV] A. Biermanns, S. Breuer, A. Trampert, A. Davydok, L. Geelhaar and U. Pietsch, *Strain accommodation in Ga-assisted GaAs nanowires grown on Silicon(111)*
Nanotechnology **23**, 305703 (2012) (chapters 5.7 / 5.8)

Other and co-authored publications

[V] A. Biermanns, U. Pietsch, J. Grenzer, A. Hanisch, S. Facsko, G. Carbone and T.H. Metzger, *X-Ray scattering and diffraction from ion beam induced ripples in crystalline silicon*
Journal of Applied Physics **104**, 044312 (2008)

[VI] A. Biermanns, A. Hanisch, J. Grenzer, T.H. Metzger and U. Pietsch, *Tuning the shape and damage in ion-beam induced ripples on silicon*
Physica Status Solidi A **208**, 2608 (2011)

[VII] O. Plantevin, R. Gago, L. Vázques, A. Biermanns and T.H. Metzger, *In situ x-ray scattering study of self-organized nanodot pattern formation on GaSb (001) by ion beam sputtering*
Applied Physics Letters **91**, 113105 (2007)

[VIII] A. Keller, A. Biermanns, G. Carbone, J. Grenzer, S. Facsko, O. Plantevin, R. Gago and T.H. Metzger, *Transition from smoothing to roughening of ion-eroded GaSb surfaces*
Applied Physics Letters **94**, 193103 (2009)

[IX] D. Carbone, A. Biermanns, B. Ziberi, F. Frost, O. Plantevin, U. Pietsch and T.H. Metzger, *Ion-induced nanopatterns on semiconductor surfaces investigated by grazing incidence x-ray scattering techniques*
Journal of Physics: Condensed Matter **21**, 224007 (2009)

[X] J. Grenzer, A. Biermanns, A. Mücklich, S.A. Grigorian and U. Pietsch, *Ripple structures on surfaces and underlying crystalline layers in ion beam irradiated Si wafers*
Physica Status Solidi A **206**, 1731 (2009)

[XI] A. Davydok, A. Biermanns, U. Pietsch, J. Grenzer, H. Paetzelt, V. Gottschalch, and J. Bauer, *Submicron resolution X-ray diffraction from periodically patterned GaAs nanorods grown onto Ge [1 1 1]*
Physica Status Solidi A **206**, 1704 (2009)

[XII] J. Bauer, U. Pietsch, A. Davydok, A. Biermanns, J. Grenzer, V. Gottschalch and G. Wagner, *X-ray investigation of the interface structure of free standing InAs nanowires grown on GaAs* $[\bar{1}\,\bar{1}\,\bar{1}]B$
Applied Physics A **96**, 851 (2009)

[XIII] A. Davydok, A. Biermanns, U. Pietsch, J. Grenzer, H. Paetzelt and V. Gottschalch, *X-Ray Diffraction from Periodically Patterned GaAs Nanorods Grown onto GaAs[111]B*
Metallurgical and Materials Transactions A **41**, 1191 (2010)

[XIV] A. Hanisch, A. Biermanns, J. Grenzer, S. Facsko and U. Pietsch, *Xe-ion beam induced rippled structures on differently oriented single-crystalline Si surfaces*
Journal of Physics D: Applied Physics **43**, 112001 (2010)

[XV] A. Davydok, S. Breuer, A. Biermanns, L. Geelhaar and U. Pietsch, *Lattice parameter accommodation between GaAs(111) nanowires and Si (111) substrate after growth via Au-assisted molecular beam epitaxy*
Nanoscale Research Letters **7**, 109 (2012)

2 Semiconductor nanowires

In this chapter, we will discuss general aspects of the epitaxial growth of free-standing semiconductor nanowires (NWs). In section 2.1, different growth mechanisms are discussed. Whereas in the past most often gold particles were used to catalyze NW growth, we will introduce how growth can be obtained without the use of gold, either by using one of the NW constituents to induce NW growth, or by the use of side-selective growth mechanisms, allowing to additionally control the position of NWs on a surface. In 2.2, the crystal structures of Si and GaAs are discussed, the materials that will be of interest later on. Whereas in particular GaAs in its bulk phase adapts the cubic zinc-blende structure, in NWs often a second polytype, the hexagonal wurtzite phase, is observed (section 2.3). Control about this different crystal structures is a major challenge in NW growth, and frequently mixtures of both structures and additional *stacking faults* are observed within the NWs.

2.1 Epitaxial nanowire growth

In the last years, various methods have been applied to grow semiconductor nanowires (NWs). First of all, two different scenarios can be distinguished, in which the grown NWs are obtained in the form of isolated, powder-like particles, or as free-standing NWs grown on an underlying substrate, respectively. Throughout this work, we focus solely on the latter, in particular on GaAs NWs grown on silicon and GaAs substrates.

Tho most common way to grow nanowires on a semiconductor substrate is the vapor-liquid-solid (VLS) growth mechanism, employing a metallic seed particle [142]. Using the VLS approach, many types of semiconductor NWs can be grown, from pure group IV materials [97, 67, 143] up to group III-V (references later on) and II-VI compounds [58, 8]. The general growth scheme is the same for all those growth methods and is sketched here: In a first step, gold particles are deposited on the substrates surface. A common way to achieve this is the deposition of a gold-film, followed by an annealing above the melting temperature of the Au, leading to a subsequent dewetting of the Au film and the formation of droplets. Alternatively, gold particles can be deposited directly, allowing to additionally control the size of the gold particles [35, 13]. After the temperature of the substrate has been adjusted to the desired growth temperature (typically several hundreds °C), atoms of the growing species (e.g. Si or Ga and As) are supplied through the vapor phase and solved in the liquid Au particle. Whenever the concentration of the growing species within the liquid phase exceeds a critical value, the difference in chemical potential between the solved particles in the droplet and the surface below the droplet (*supersaturation*) favors the formation of a solid monolayer at the interface between the droplet and the underlying material. In this way, a new layer of atoms is added to the nanowire, lifting the droplet upwards from the surface, which is again enriched with atoms of the growing species and so on.

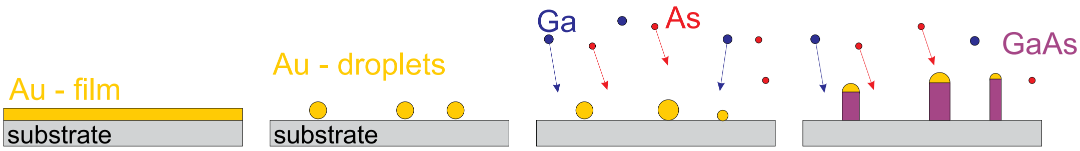

Figure 2.1: Schematic representation of the Au-assisted vapor-liquid-solid growth. In a first step, liquid Au droplets are deposited on a bare substrate surface, usually by annealing of an initially deposited Au film. If the growing species, e.g. Ga and As, are supplied from the vapor phase, they can be collected in the Au droplet, until the supersaturation of the droplet leads to the crystallization of a nanowire at the liquid-solid interface.

Different techniques exist to supply the growing species. In vapor phase epitaxy, growth is carried out in a laminar gas flow at elevated temperatures and medium high pressures in the range of several 10s to 100s mbar. In metal-organic vapor phase epitaxy (MOVPE), the growing agent is bond to a precursor material, that has to be cracked by a catalytic process in the first step to release the atoms on the surface or the liquid particle. Alternatively, physical processes can be used, in which the atoms are readily supplied in their native state or in the form of molecules (e.g. As^2 or As^4) , and no further chemical reaction is involved. Among them are physical-vapor-deposition (PVD) and molecular beam epitaxy (MBE). Whereas a possible advantage of the chemical growth schemes is their relatively high growth rate, enabling the growth or processing of large surfaces in a very short time, MBE is significantly slower, but is considered to allow for more precise structures and higher purity, as the growth is performed in ultra high vacuum.

Although the growth scheme using Au-particles as sketched above is highly successful, and also limitations like the random position and size distribution of the initial gold particles can be overcome [102], the Au-assisted approach suffers from the drawback that for most large scale, commercial production processes the use of Au has to be strictly avoided. In particular, gold catalysts are incompatible with Si based devices and standard CMOS technology, because Au traps electrons and holes in silicon [21]. Furthermore, Au can be incorporated into the NW or on the NW sidewalls, forming deep levels in the band gap of the material and thus deteriorate the device performance [117]. For the special case of GaAs nanowires grown on Si, a comparison of charge carrier lifetimes in photoluminescence showed that the use of Au seed particles compared to a Ga-assisted growth scheme (see below) reduced the minority carrier lifetime by four orders of magnitude, making them less favorable for technological applications [15]. Nevertheless, the detailed influence of Au particles on electronic or optical performance is currently a matter of intense debate, and to date no final conclusion of the detailed influence of Au on the NW's performance can be drawn [4, 63].

Another important factor is the control of the crystalline phase of the growing nanowires. Au-assisted GaAs NWs grow usually in the hexagonal wurtzite (WZ) structure [134], although cubic zinc-blende (ZB) wires can be obtained under specific conditions [131]. Either way, typically a large number of stacking faults, inclusions of the other polytype or zinc-blende twins are observed[34, 133]. However, the possible device performance and electronic structure of the NWs crucially depend on the crystal structures, for example the WZ phase is observed to exhibit a larger band gap compared to the ZB phase, leading to type II heterostructures within single NWs when those polytypes mix [29, 133, 57, 64]. Therefore, understanding and control of these structural changes are crucial to tailor the electronic structure of NWs.

As an alternative, there exist different approaches for NW growth without the use of Au particles, two of which will be of importance in this work. In the case of III-V semiconductor NWs, the Au particle can be replaced by droplets formed directly by the group III metal. For the case of GaAs, this was first demonstrated by Fontcuberta et al. on an oxide covered GaAs surface [46, 24]. The process is illustrated in figure 2.2. In a first step, the substrate is covered by a thin oxide layer. This oxide layer can either be the native oxide, for example in the case of a Si substrate, or may be deposited by thermal or chemical treatment of the surface. In a next step, Ga and As are supplied in the growth chamber at the desired growth temperature. Whereas As initially desorbs from the surface, Ga atoms can accumulate on the surface and form droplets. It is assumed that these droplets are pinned at defects within the surface layer, occurring at random positions. At this positions, the Ga can partially dissolve the oxide layer, leading to a direct contact with the underlying substrate, on which heteroepitaxial growth can start. In the following, this growth mode will be denoted as *Ga-assisted VLS growth*.

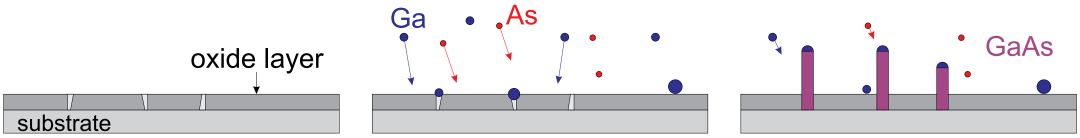

Figure 2.2: Schematic representation of the Ga-assisted growth of GaAs nanowires in MBE. In this case, growth is initiated on an substrate covered by a thin oxide layer, that can be a native oxide or an artificially deposited layer. If Ga and As are supplied in the vapor phase, Ga droplets form on the surface and are bond to defects or inhomogeneities in the oxide layer. Subsequently, vapor-liquid-solid growth leads to the formation of GaAs nanowires.

This growth scheme naturally avoids a possible incorporation of impurity atoms into the NW, as no other atoms are present during growth. In addition, NWs obtained using the self-assisted approach are frequently found to grow in the cubic ZB structure , however the wurtzite structure and mixtures of both are observed as well [133, 109, 75, 64].

A second possibility to avoid the use of seed particles is to replace the catalyzed growth by a side-selective growth on a substrate that is partially covered by a mask, on which no growth occurs. In this case, the growth parameters (temperatures, pressures, fluxes etc.) are chosen to favor the growth along one direction, typically corresponding to a [1 1 1] B direction. For example, GaAs nanowires can be grown using selective-area MOVPE throughout openings in a SiO_x or SiN_x layer, that has been patterned by electron beam lithography and etching of small openings in the oxide layer. In this case, NWs will only form at places where the mask has been removed, allowing to realize arbitrary arrangements of NWs [56, 2, 60, 103].

2.2 Crystal structures of Si and GaAs

Throughout this work, most experiments focus on the investigation of GaAs nanowires, either grown on GaAs or Si substrates. Silicon crystallizes in the diamond crystal structure. This structure can be visualized as a face centered cubic (fcc) lattice with lattice parameter a^c, together with a basis of two atoms at the coordinates $(0,0,0)$ and $\left(\frac{1}{4}, \frac{1}{4}, \frac{1}{4}\right) a^c$ in the cubic unit cell. We can therefore also think of two fcc lattices, displaced by $\left(\frac{1}{4}, \frac{1}{4}, \frac{1}{4}\right) a^c$ along the space diagonal. Figure 2.3(a) shows the crystal structure in the cubic unit cell[1]. Each of the atoms in the diamond structure is bond to four other atoms in a tetrahedral arrangement. GaAs, in its bulk form, crystallizes in the cubic zinc-blende phase (ZB). This crystal structure is very similar to the diamond one, but in this case the two sublattices at $(0,0,0)$ and $\left(\frac{1}{4}, \frac{1}{4}, \frac{1}{4}\right) a^c$ are occupied by Gallium and Arsenic atoms, respectively (figure 2.3(b)).

Whereas the Si structure has an inversion center at $\left(\frac{1}{8}, \frac{1}{8}, \frac{1}{8}\right) a^c$, this inversion symmetry is broken in the GaAs ZB structure. When viewed along the space diagonal of the cubic cell (the [1 1 1] direction) in fig. 2.3(b), two different arrangements are possible, either with the group III metal atom (Ga) below the group V atom (As) or vice versa. To distinguish between those two cases, the directions are labeled [1 1 1]A and [1 1 1]B, respectively[2]. The growth of GaAs nanowires usually occurs along the [1 1 1]B direction, although occasionally [1 1 1]A wires are observed as well [141].

When viewed along the space diagonal of a fcc crystal, we see that the crystal is composed by a stack of atomic planes containing atoms in a hexagonal arrangement, representing the maximum filling factor possible. Two of this *hexagonal close packed* layers are indicated for the fcc sublattice at (0,0,0) in figure 2.3(b). The third layer contains the atom at (0,0,0) and is not shown. The distance a^h between atoms in this hexagonal layers is given by $a^h = 1/\sqrt{2}\, a^c$, and will be denoted as *in-plane lattice parameter* later on. The atoms in two subsequent of this layers are not located above each other, but displaced in order to form a close packed structure. If the first layer is labeled 'A', there are

---

[1] Whereas the description of diamond and zinc-blende structures in a cubic unit cell is the most common one, both structures can also be described by a hexagonal unit cell, compare section 3.3 and appendix A.

[2] Alternatively, A and B directions are labeled according to the polarity of the corresponding surface, assuming the crystal terminates at one of the shaded (1 1 1) planes in fig. 2.3. The surface terminated by group III atoms is labeled A, the group V surface B.

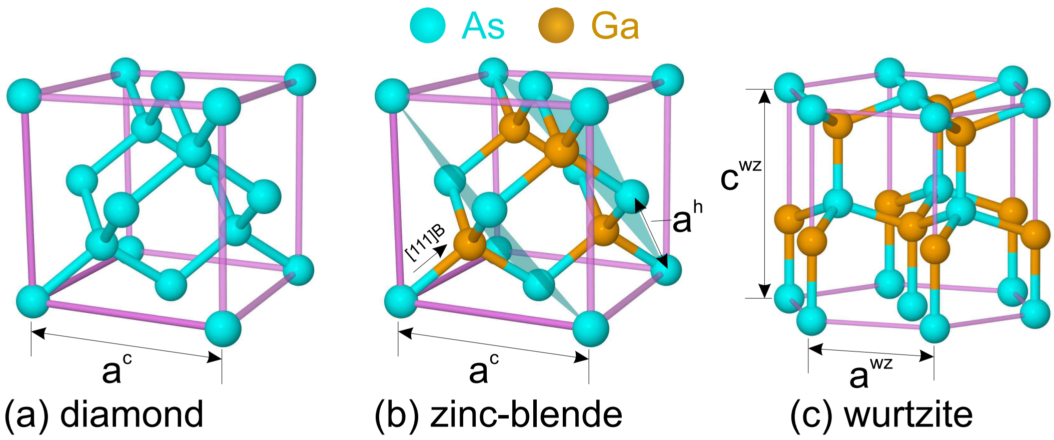

Figure 2.3: (a) The diamond-structure as adapted by silicon consists of two fcc-lattices displaces by $\left(\frac{1}{4}, \frac{1}{4}, \frac{1}{4}\right) a^c$ along the space diagonal. In the zinc-blende lattice (b), both fcc lattices are occupied by different atoms, e.g. Ga and As. The structure can be thought of as bilayers of Ga-As stacked in a sequence ABCABC... . The hexagonal wurtzite structure (c) is build from bilayers stacked in a sequence ABAB... .

two different ways to arrange the second layer above the first on, denoted as 'B' and 'C' in figure 2.4. In the ZB structure, the crystal naturally adapts a stacking sequence of the order 'ABCABC'. This stacking can also be described by a hexagonal structure with lattice parameters a^h and $c^h = \sqrt{3}\,a^c$ (cf. appendix A). Besides this fcc-type of stacking, two subsequent layers may also order in an alternating manner like 'ABABAB', known as *hexagonal closed packing* (hcp)[3]. The unit cell of this structure can only be described by a hexagonal Bravais lattice. In the binary compounds like GaAs, the corresponding structure is of the *wurtzite* (WZ) type and displayed in figure 2.3(c). Due to the reduced number of layers, the geometrical lattice parameter c^{wz} of this structure is by 2/3 shorter than the cubic one. In addition, GaAs and other III-V materials are expected to exhibit small deviations in lattice parameters in the WZ phase compared to the ZB one (see below).

Table 2.1 summarizes the bulk lattice parameters of the cubic and hexagonal structures of Si and GaAs, respectively[79]. The bulk materials have a lattice mismatch of $\frac{a^c_{GaAs} - a^c_{Si}}{a^c_{Si}} = 4.1\%$.

---

[3] In a model of hard spheres, both fcc and hcp structures have the same filling factor of 74%.

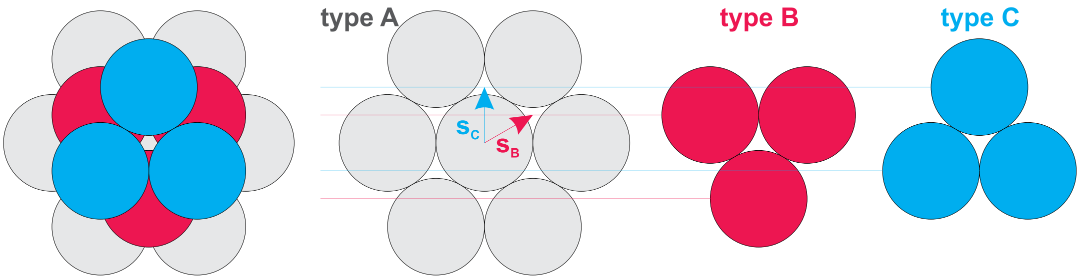

Figure 2.4: Stacking-sequence of the cubic close packed structure, corresponding to a view along the [111] direction of a fcc structure.

	a^h / Å	$a^h = \frac{1}{\sqrt{2}}\, a^c$ / Å	$c^h = \sqrt{3}\, a^c$ / Å
Si	5.43102	3.8403	9.4068
GaAs	5.6536	3.9977	9.7923

Table 2.1: Bulk lattice parameters of silicon and GaAs at room temperature [from [79]].

2.3 Zinc-blende - wurtzite polytypism

In its bulk phase, GaAs adapts the cubic zinc-blende structure as presented in section 2.2. Figure 2.5(left) shows a view of this structure along the $[1\,0\,\bar{1}]^c$ direction, visualizing the stacking sequence ABCABC. The structure consists of pairs of Ga and As atoms, whose coordinates differ only along the $[1\,1\,1]$ direction (e.g. the rows (a) and (a') or (b) and (b')). For the sake of simplicity, this pairs of atomic planes will be denotes as *monolayers* (ML), which are then stacked in a sequence ABCABC... to form the ZB structure.

Because NW growth proceeds in a layer-by-layer scheme along the cubic $[1\,1\,1]$ direction, often *stacking faults* and rotational *twins* are observed. A rotation twin is a special type of stacking fault in the ZB lattice, by which the stacking sequence is inverted at a *twin boundary*, corresponding to a rotation of the initial ZB lattice by 180° along the growth direction. A rotational twin changes the initial sequence in the form (ABC[AB|A]CBA), with the twin boundary indicated by the vertical line. As we see, a twin boundary leads to the formation of one layer (layer B in above example) in a hexagonal environment, denoted by square bracket. The defect is shown in the second view of figure 2.5.

In principal, twin boundaries can be inserted into the crystal after every monolayer. If two twin boundaries occur at subsequent monolayers, the initial stacking sequence is preserved after the faulted segment. If a twin boundary occurs after each monolayer, the entire ZB structure is transformed into the hexagonal wurtzite structure with stacking sequence ABABAB, shown in figure. 2.5(right).

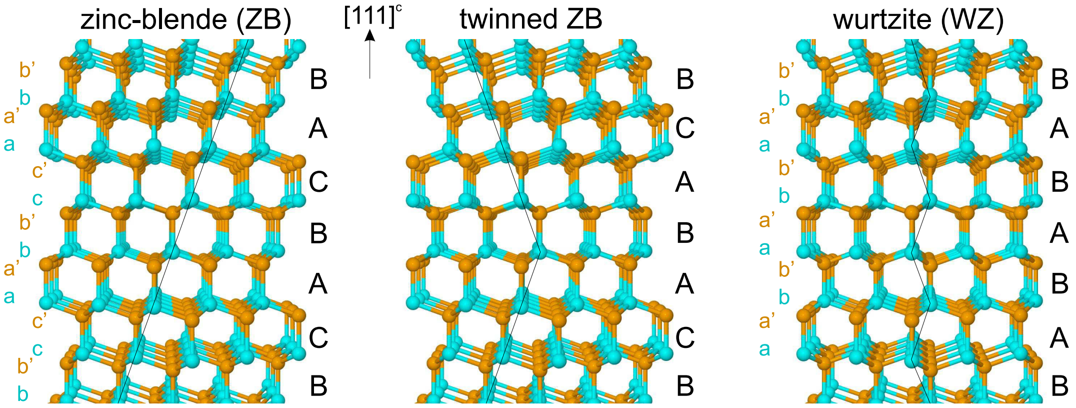

Figure 2.5: View along the $[1\,0\,\bar{1}]^c$ direction on the zinc-blende structure (ZB), a twinned ZB structure and the corresponding direction in a hexagonal wurtzite (WZ) structure.

For NWs grown using the VLS mechanism, it is assumed that the nucleation process of the growing MLs strongly influences which of the different polytypes grows. As first calculated by Glas et al. [51], the formation of the one or other polytype can be related to the change in supersaturation during growth, which is affected by the side-wall energies of the forming NW facets together with the contact angle of the liquid droplet. Controlling the density of growth faults is one of the main issues in NW growth.

Hexagonality Besides the cubic zinc-blende and the hexagonal wurtzite phase, other periodic structures with larger unit-cells are possible if the stacking sequence can change arbitrarily. For example, the *4H* structure has a unit-cell of four bilayers, arranged in a sequence ABCBABCB. To classify these structures, it is convenient to define the *hexagonality*, given by the fraction of bilayers in the unit-cell that are arranges in a hexagonal environment, i.e. layers stacked between equal layers on either side [106]. In this respect, the cubic ZB structure has a hexagonality of 0%, the 4H structure 50% (the layers C and A) and the

WZ structure 100%. If we assume that the initial structure is the ZB one (0% hexagonality), the hexagonality can also be calculated as the inverse distance of subsequent twin-boundaries.

Based on density functional theory (DFT) calculations it was predicted that for III-V compounds like GaAs, InAs or InP, the *c/a-ratio* , given by two times the distance of the hexagonal close packed planes divided by the in-plane atomic distance a^h, increases as function of the *hexagonality* from the ideal value of 1.633 for the zinc-blende structure. This increase is realized by a relative decrease of the in-plane lattice parameter a^h and an increase in the lattice plane spacing along the c axis [106]. For InAs and InSb NWs, Kriegner et al. studied the lattice parameters of the cubic zinc-blende phase as well as the hexagonal 4H and the wurtzite structure. They showed that in accordance with DFT calculations, the vertical lattice parameter increases gradually for a transition from ZB to WZ, whereas the in-plane lattice parameter decreases at the same time. The transition in lattice parameter was found to be an almost linear function of the hexagonality[74]. For the specific case of GaAs nanowires, different values have been reported in literature, and in particular the functional dependence on the hexagonality was not observed yet (cf. chapter 5).

3 Kinematic x-ray diffraction

In this chapter we describe the basic principles of x-ray diffraction from crystals in the kinematic approximation, i.e. neglecting multiple scattering and diffraction effects that become important for highly perfect, large crystals and are described by the dynamical theory of x-ray diffraction [6]. The kinematic approximation is sufficient to describe the diffraction experiments from small nanostructures performed in this work.

For the sake of completeness, in section 3.1 the definitions of the crystal lattice, lattice planes as well as the reciprocal lattice are briefly introduced. In section 3.2, the necessary principles of x-ray diffraction are introduced, followed by a definition of reciprocal space coordinates in the special case of hexagonal structures, allowing to describe the diffraction from nanowires with arbitrary stacking sequences of hexagonal close packed layers in section 3.3. Finally, the realization of the diffraction experiments at synchrotron sources is described in section 3.4, including the focussing of x-rays to the nanometer regime, data acquisition and the experimental constraints imposed by the nanodiffraction setup.

3.1 Crystals and the reciprocal lattice

A crystal is characterized by a periodic *lattice* and a *basis*, attached to each lattice point. Here, the basis is in the simplest form a single atom, but can also be a large group of atoms or a complex molecule. This basis is arranged periodically in space at a set of lattice points (the *lattice*), which is defined by the set of vectors $\mathbf{r}$ that can be expressed as

$$\mathbf{r} = u\,\mathbf{a}_1 + v\,\mathbf{a}_2 + w\,\mathbf{a}_3 \tag{3.1}$$

with integers u, v and w. The vectors $\mathbf{a}_{1,2,3}$ are called primitive translation vectors of the lattice. The choice of these vectors is not unique, as many different sets of translation vectors can define the same set of lattice points. The parallelepiped defined by the vectors $\mathbf{a}_{1,2,3}$ is called primitive unit cell if it contains only one lattice point. As we will see below, for the description of crystals it is often convenient to replace the primitive lattice vectors by a set of vectors that more directly represents the symmetry of the crystal. In this case, the primitive translations and unit cell can be replaced by a set of crystal axes together with a basis of more than one atoms. In this case, the unit cell spanned by the crystal axes is not primitive anymore and contains more than one atom or lattice point, respectively.

Atomic planes in crystals

The periodic arrangement of lattice points in a crystal allows to systematically define *lattice planes* that make up a crystal. The orientation of a lattice plane with respect to the crystallographic axes is characterized by the *Miller indices* $(h\,k\,l)$, which are obtained by first determining the intercepts of the plane with the crystal axes in terms of the lattice constants $a_{1,2,3}$, then taking the reciprocal of these values and finding integers (h k l) having the same ratio. If a plane runs parallel to one of the crystal axes, the corresponding index is 0. Figure 3.1 demonstrates this principle for exemplary planes of a cubic crystal. The set of symmetry equivalent planes in a crystal, for example the side-planes of a cube in a cubic crystal, is denoted by curly brackets (e.g. $\{1\,0\,0\}$ for the cubic side-planes).

The distance between two subsequent planes with Miller indices (h k l) can be calculated, if the lattice constants and type of the underlying Bravais lattice are known. For the cubic and hexagonal lattice, the distances can be calculated according to

$$d^c_{hkl} = \frac{a}{\sqrt{h^2+k^2+l^2}} \quad ; \quad d^h_{hkl} = \frac{a}{\sqrt{\frac{4}{3}\left(h^2+h\,k+k^2\right)+\left(\frac{a}{c}\right)^2 l^2}} \tag{3.2}$$

Similar to the definition of lattice planes, a direction in a crystal is denoted by indices obtained from the coordinates of the directional unit vector with respect to the crystal axes. These indices are written in square brackets [h k l]. For example, the [1 0 0] direction is parallel to the $\mathbf{a}_1$ axis, whereas the [1 1 1] direction in a cubic crystal points along the space diagonal. By construction, the direction [h k l] is perpendicular the plane with the same indices (h k l).

As a peculiarity, in order to account for the symmetry of a hexagonal crystal, the indices and directions in the hexagonal system are denoted by four indices

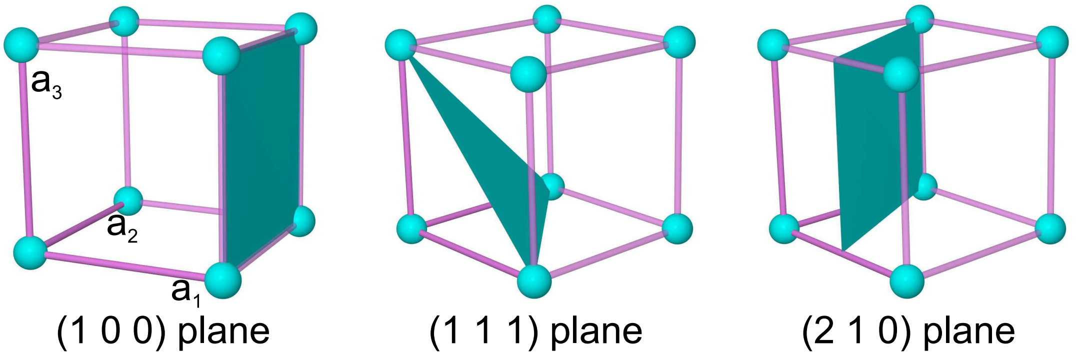

Figure 3.1: The orientation of the planes with Miller indices (1 0 0), (1 1 1) and (2 1 0) in the cubic unit cell.

(h k i l), where i=-(h+k). The concept is depicted in figure 3.2, where besides the crystal axes $\mathbf{a}_1$ and $\mathbf{a}_2$ (corresponding to the indices h and k) a third direction $\mathbf{a}_i$ is introduced, referred to by the index i. By obeying the relation for i, the direction parallel to $\mathbf{a}_1$ is referred to as $[2\,\bar{1}\,\bar{1}\,0]$, whereas the direction $[1\,0\,\bar{1}\,0]$ is rotated by 30° with respect to $\mathbf{a}_1$ and 90° compared to $\mathbf{a}_2$. As we will see, this construction is consistent with the corresponding reciprocal lattice of a hexagonal lattice.

The reciprocal lattice

Closely related with every crystal structure is the *reciprocal lattice*. If the lattice structure in real space is characterized by the set of vectors $\mathbf{R}$, then the reciprocal lattice is defined as the set of *reciprocal lattice vectors* $\mathbf{G}$, that fulfill the condition

$$e^{i\,\mathbf{G}\cdot\mathbf{R}} = 1\,. \tag{3.3}$$

Therefore, the scalar product $\mathbf{G}\cdot\mathbf{R}$ needs to be an integer multiple of 2π. If the vectors $\mathbf{R}$ are defined as a linear combination of the primitive translation vectors $\mathbf{a}_{1,2,3}$, then the vectors $\mathbf{G}$ can be expressed by a linear combination of primitive vectors of the reciprocal lattice $\mathbf{b}_{1,2,3}$ according to

$$\mathbf{G}_{hkl} = h\,\mathbf{b}_1 + k\,\mathbf{b}_2 + l\,\mathbf{b}_3 \tag{3.4}$$

with

$$\mathbf{b}_1 = 2\pi\frac{\mathbf{a}_2\times\mathbf{a}_3}{\mathbf{a}_1\cdot(\mathbf{a}_2\times\mathbf{a}_3)}\;;\quad \mathbf{b}_2 = 2\pi\frac{\mathbf{a}_3\times\mathbf{a}_1}{\mathbf{a}_1\cdot(\mathbf{a}_2\times\mathbf{a}_3)}\;;\quad \mathbf{b}_3 = 2\pi\frac{\mathbf{a}_1\times\mathbf{a}_2}{\mathbf{a}_1\cdot(\mathbf{a}_2\times\mathbf{a}_3)} \tag{3.5}$$

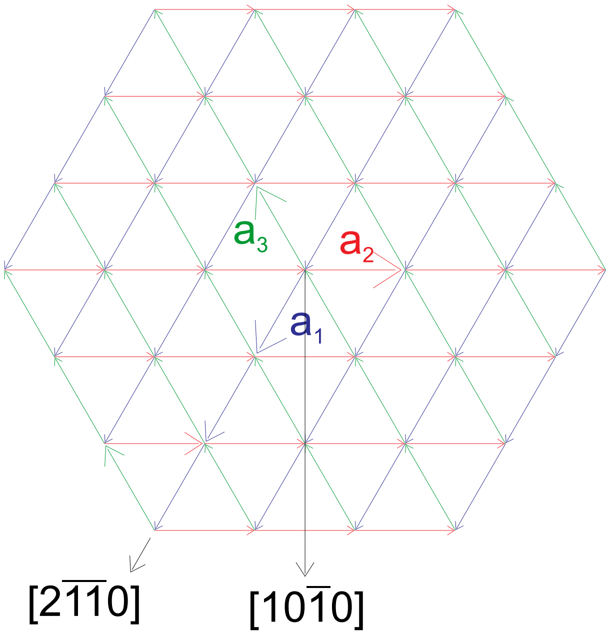

Figure 3.2: Representation of directions in the hexagonal coordinate system using three indices h, k and i=-(h+k). In this formalism, a direction along the basis-vector $\mathbf{a}_1$ is indexed as $[2\,\overline{1}\,\overline{1}\,0]$, whereas the description $[1\,0\,0\,0]$ is not allowed. (adapted from [73])

The set of the reciprocal vectors **G** defines the *reciprocal lattice*. It can be shown that the reciprocal lattice vector $\mathbf{G}_{hkl}$ is perpendicular to the plane (h k l), and the magnitude G_{hkl} is inversely proportional to the lattice plane spacing according to $G_{hkl} = \frac{2\pi}{d_{hkl}}$.

3.2 X-ray diffraction from nanostructures

The scattering of x-rays from a single free electron is described by the Thomson scattering. In a classical picture, a charged free electron is accelerated by the incoming electromagnetic wave. The resulting oscillation of the electron leads to reemission of a spherical wave with the same frequency as the original wave and a dipole angular distribution. At large distance R of the electron from the observer, the amplitude of the scattered wave is given by [125]

$$A_{rad}(\mathbf{r}, R) = r_o P A_0 e^{i\mathbf{k_i}\cdot\mathbf{r}} \frac{e^{ikR}}{R} \tag{3.6}$$

where P is a polarisation factor depending on the scattering geometry, and elastic scattering is considered with $|\mathbf{k_i}| = k = 2\pi/\lambda$. The equation holds for both electric and magnetic field amplitudes.

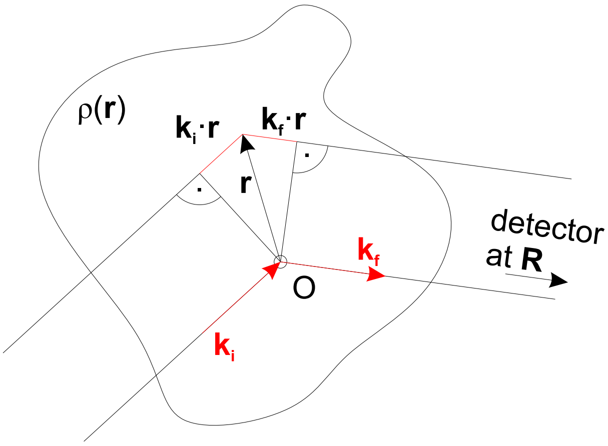

Figure 3.3: The scattering of a incoming wave with wave vector $\mathbf{k}_i$ at different positions $\mathbf{r}$ in a volume V with electron density $\rho(\mathbf{r})$ leads to a phase difference $\mathbf{r} \cdot (\mathbf{k}_f - \mathbf{k}_i)$ and therefore interference between the scattered waves in a large distance $\mathbf{R}$. (adapted from [72])

In the kinematic approach, multiple scattering is neglected and the total scattered amplitude is given by a coherent summation over all scattered partial waves, described by the objects electron density $\rho(\mathbf{r})$ (compare figure 3.3):

$$A_{rad}(\mathbf{R}) = A_0 r_0 P \int \rho(\mathbf{r}) e^{i\mathbf{k_i}\cdot\mathbf{r}} \frac{e^{ik|\mathbf{r}-\mathbf{R}|}}{|\mathbf{r}-\mathbf{R}|} \mathrm{d}\mathbf{r}. \tag{3.7}$$

The integration is performed over the coherently illuminated volume.

In case that the distance between sample and detector $\mathbf{R}$ is much larger than the size of the coherently illuminated sample $(\mathbf{r})$, the Fraunhofer approximation can be applied and equ. (3.7) becomes:

$$A(\mathbf{q}) = A_0 r_0 P \frac{e^{ikR}}{R} \int \rho(\mathbf{r}) e^{i\mathbf{q}\cdot\mathbf{r}} \mathrm{d}\mathbf{r} \tag{3.8}$$

where $\mathbf{q}$ is the scattering vector defined as:

$$\mathbf{q} = \mathbf{k_f} - \mathbf{k_i} \tag{3.9}$$

We thus see that the scattered amplitude is proportional to the Fourier transform of the object's electron density. In a infinite, perfect periodic lattice, (3.8) leads to sharp *Bragg peaks* in reciprocal space because the integral vanishes whenever $\mathbf{q}$ is not equal to a reciprocal lattice vector $\mathbf{G}_{hkl}$. The description of the diffraction condition $\mathbf{q} = \mathbf{G}_{hkl}$ is equivalent to *Bragg's law*, describing the constructive interference of partially reflected x-ray waves at lattice planes with distance d_{hkl} by the necessary diffraction condition

$$\text{Bragg's law:} \quad n\,\lambda = 2\,d_{hkl}\,\sin\theta_B, \tag{3.10}$$

with n being an integer number and θ_B the *Bragg angle*.

Taking into account that the scattering centers in a solid are given by the location of the electrons, for a crystal of finite size the integral can be replaced by a summation over all electrons. To this end, it is convenient to write

$$\mathbf{r} = \mathbf{r}_{\mathrm{cell}} + \mathbf{r}_{\mathrm{n}} + \mathbf{r'}_n,$$

where $\mathbf{r}_{\mathrm{cell}}$ is the position of the different unit cells in the crystal, $\mathbf{r}_{\mathrm{n}}$ is the position of atom n in the unit-cell and $\mathbf{r'}_n$ describes the electron-distribution around atom n. This replaces the integral by a summation of all atoms in the unit-cell and a sum over all unit cells:

$$A(\mathbf{q}) \propto \sum_n \underbrace{\left(\int \rho(\mathbf{r}'_n)\, e^{i\,\mathbf{q}\cdot\mathbf{r'}_n} d\mathbf{r'}_n \right)}_{\text{atomic form factor} f_n(\mathbf{q})} e^{i\,\mathbf{q}\cdot\mathbf{r}_n} \sum_{\text{cells}} e^{i\,\mathbf{q}\cdot\mathbf{r}_{cell}} \tag{3.11}$$

$$= \underbrace{\sum_n f_n(\mathbf{q}) e^{i\,\mathbf{q}\cdot\mathbf{r}_n}}_{\text{structure factor } F(\mathbf{q})} \underbrace{\sum_{\text{cells}} e^{i\,\mathbf{q}\cdot\mathbf{r}_{cell}}}_{\text{lattice sum}} \tag{3.12}$$

Here, the integral of the electron density of the atom n in the unit cell has been replaced by the *atomic form factor* f_n.[4]. The first sum, the *structure factor* $F(\mathbf{q})$, determines the intensity of a certain Bragg reflection, whereas the second *lattice sum* defines the possible locations of reflections in reciprocal space whenever $\mathbf{q}$ equals a reciprocal lattice vector $\mathbf{G}_{hkl}$. In appendix A, the structure factors of the zinc-blende and wurtzite crystal structures are discussed.

Any deviation from a perfect infinite lattice leads to intensity away from the exact Bragg position. Even for the most perfect available crystals, the introduction of a surface truncates the periodic lattice into one half of the space, as a consequence leading to so called *crystal truncation rods* (CTR) perpendicular to the surface [123].

Another deviation from the perfect infinite lattice is given if the diffracting object has a finite size or the atoms within the structure are displaces from their ideal positions, for example if the crystal is strained. To encounter for this effects, a nanoobject is usually described by a *shape function* $\Omega(\mathbf{r})$, defined as unity inside the volume of the object and zero outside. If the object

---

[4] Tabulated parametric functions for the atomic form factors of the elements can be found in the International Tables for Crystallography [115].

is additionally strained, the displacement of the atoms from their unstrained reference positions can be described by a displacement field $\mathbf{u}(\mathbf{r})$, depending on the position $\mathbf{r}$ itself. In this case, 3.8 is written as.

$$A(\mathbf{q}) = A_0 r_0 P \frac{e^{ikR}}{R} \int \rho(\mathbf{r})\, \Omega(\mathbf{r})\; e^{i\mathbf{q}\cdot(\mathbf{r}+\mathbf{u}(\mathbf{r}))} \mathrm{d}\mathbf{r} \tag{3.13}$$

For elastically strained objects, we can assume that the extend of the displacement field is much larger than the size of a unit cell and approximate that all atoms in the unit cell are displaced by the same amount. For a nanoobject of volume V, the diffracted intensity in the vicinity $\Delta\mathbf{q}$ of a reciprocal lattice point $\mathbf{G}$ can then be expressed as [140]

$$I_{\mathbf{G}}(\Delta\mathbf{q}) = \frac{|F(\mathbf{G})|^2}{V^2} |A_G(\Delta\mathbf{q})|^2 \tag{3.14}$$

with

$$A_G(\Delta\mathbf{q}) = \int \Omega(\mathbf{r})\, e^{i\,\mathbf{G}\cdot\mathbf{u}(\mathbf{r})} e^{i\Delta\mathbf{q}\cdot\mathbf{r}} \mathrm{d}\mathbf{r}. \tag{3.15}$$

Here, $F(\mathbf{G})$ is the *structure factor* of the Bragg reflection $\mathbf{G}$. We thus see that this *diffuse intensity* can be obtained by a Fourier transformation of the displacement field, projected onto the probed reciprocal lattice vector $\mathbf{G}$.

In a common approach to simulate the diffracted intensity from a strained nanostructure, the displacement field $\mathbf{u}(\mathbf{r})$ is obtained within a finite element method (FEM) simulation of the elastic deformation in the structure, subjected to an external perturbation, e.g. a tensile or compressive stress at the heterointerface between two different materials or applied electric fields (cf. section 6.3).

For a strain-free object of finite size, the scattered amplitude is given by the Fourier transform of the objects shape, and hence the measured intensity will show characteristic modulations whose distance is inversely proportional to the object's size. As example, this is illustrated in figure 3.4, showing a 2-dimensional hexagon of constant electron density and the square modulus of its Fourier transform (b), which is proportional to the expected intensity distribution around a reciprocal lattice point. The intensity shows characteristic streaks of intensity, arising from the side-facets of the hexagon, together with modulations of the intensity whose distances are inversely proportional to the diameter of the hexagon (fig. 3.4(c)).

Figure 3.4: (a) A regular hexagon with diameter of D=500 nm and constant, homogeneous density and (b) the square modulus of its Fourier transformation, which is equivalent to the intensity distribution around a reciprocal lattice point. (c) A Line profile along the q_x direction (dashed line in (b)). Thickness-fringes measure the diameter of the hexagon.

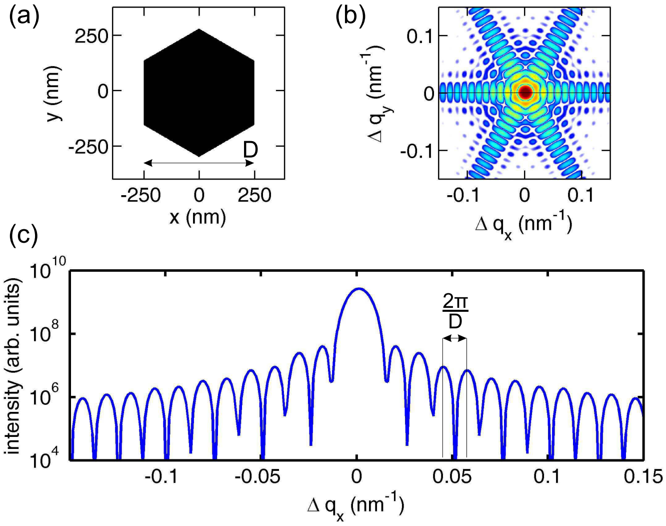

Coherent x-ray diffraction

From equation (3.8) we see that a precise measurement of the scattered amplitude should allow to retrieve the object's election density by an inverse Fourier transformation. However, in a conventional x-ray diffraction experiment only the intensity, given by the squared modulus of the amplitude, can be measured, thus the phase-information is lost and a direct inversion of the measured data impossible. This problem is also known as the phase-problem in crystallography. In recent year, many attempts have been made to overcome this issue. One key experiment for future free electron lasers (FELs) will be the measurement of the coherently scattered intensity from single molecules, allowing to reconstruct the molecules' structure without the need of a prior crystallization [19, 129]. Various methods have been proposed to retrieve the full information of an object's amplitude and phase from a measured intensity pattern. The most prominent of those methods rely on either the direct encoding of the phase information using holographic methods [47, 17], or on the reconstruction of the phase information based on the measured amplitude and certain constraints, like a known maximum size or symmetries, of the scattering objects or ptychographic methods [49, 93, 124, 122, 52]. Important for a successful reconstruction is the coherence of the illuminating x-ray beam, ensuring that all scattered photons have a common phase relation and produce an interference pattern with high visibility. Synchrotron sources provide partially coherent radiation. Here, a fully coherent illumination of an object can be obtained if the size of the incoming x-ray beam is reduced to the coherent volume, given by the properties of the synchrotron-source [88]. In *coherent x-ray diffraction*, the three-dimensional amplitude around a selected Bragg peak is measured with high resolution, while the sample is illuminated with a fully coherent x-ray beam. In order to retrieve the amplitude and phase information of the diffracting object, iterative algorithms can be applied, as will be further discussed in section 4.3.

3.3 Indexing reciprocal lattice points

Later on, x-ray diffraction from nanowires grown on GaAs $(1\,1\,1)$ and silicon $(1\,1\,1)$ surfaces will be described. Due to an epitaxial relation with the substrate, also the nanowires have the same principal orientation, i.e. they consist of hexagonal close packed atomic layers stacked along the $[1\,1\,1]$ direction. To encounter for the hexagonal symmetry in the $(1\,1\,1)$ planes, it is convenient to index the reciprocal lattice points in a *surface-coordinate system* that exhibits the hexagonal symmetry. In the following, we will use the superscript c to refer to the cubic coordinate system and the superscript h to refer to the corresponding hexagonal surface-coordinate system *of the cubic structure.*

Following usual definitions, it is possible to relate the cubic and the hexagonal surface-coordinate systems using a matrix transformation. Given the basis of the cubic structure by the vectors $\mathbf{a}_1^c = a_0\hat{\mathbf{x}}$, $\mathbf{a}_2^c = a_0\hat{\mathbf{y}}$ and $\mathbf{a}_3^c = a_0\hat{\mathbf{z}}$, an appropriate basis in the surface coordinate system is given by [44]

$$
\begin{aligned}
\mathbf{a}_1^h = & \ \frac{1}{2}\left(\mathbf{a}_1^c - \mathbf{a}_3^c\right) = \frac{1}{2}a_0\left(\hat{\mathbf{x}} - \hat{\mathbf{z}}\right) \\
\mathbf{a}_2^h = & \ \frac{1}{2}\left(-\mathbf{a}_1^c + \mathbf{a}_2^c\right) = \frac{1}{2}a_0\left(-\hat{\mathbf{x}} + \hat{\mathbf{y}}\right) \\
\mathbf{a}_3^h = & \left(\mathbf{a}_1^c + \mathbf{a}_2^c + \mathbf{a}_3^c\right) = a_0\left(\hat{\mathbf{x}} + \hat{\mathbf{y}} + \hat{\mathbf{z}}\right).
\end{aligned}
\tag{3.16}
$$

This vectors describe a hexagonal system with $a_1^h = a_2^h = a_0/\sqrt{2}$, $a_3^h = \sqrt{3}\,a_0$ and angles $\angle(\mathbf{a}_1^h, \mathbf{a}_2^h) = 120°$ and $\angle(\mathbf{a}_1^h, \mathbf{a}_3^h) = \angle(\mathbf{a}_2^h, \mathbf{a}_3^h) = 90°$. Using equations

(3.5), the reciprocal lattice vectors of this lattice are calculated as

$$\begin{aligned}\mathbf{b}_1^h =& \ \frac{2}{3}\left(\mathbf{b}_1^c + \mathbf{b}_2^c - 2\mathbf{b}_3^c\right) = \frac{2\pi}{a_0}\frac{2}{3}\left(\hat{\mathbf{x}} + \hat{\mathbf{y}} - 2\hat{\mathbf{z}}\right)\\ \mathbf{b}_2^h =& \frac{2}{3}\left(-\mathbf{b}_1^c + 2\mathbf{b}_2^c - \mathbf{b}_3^c\right) = \frac{2\pi}{a_0}\frac{2}{3}\left(-\hat{\mathbf{x}} + 2\hat{\mathbf{y}} - \hat{\mathbf{z}}\right)\\ \mathbf{b}_3^h =& \ \frac{1}{3}\left(\mathbf{b}_1^c + \mathbf{b}_2^c + \mathbf{b}_3^c\right) = \frac{2\pi}{a_0}\frac{1}{3}\left(\hat{\mathbf{x}} + \hat{\mathbf{y}} + \hat{\mathbf{z}}\right).\end{aligned} \tag{3.17}$$

This vectors describe again a hexagonal system with $b_1^h = b_2^h = \frac{4\pi}{a_0}\sqrt{\frac{2}{3}}$, $b_3^h = \frac{2\pi}{\sqrt{3}a_0}$ and angles $\angle(\mathbf{b}_1^h, \mathbf{b}_2^h) = 60°$ and $\angle(\mathbf{b}_1^h, \mathbf{b}_3^h) = \angle(\mathbf{b}_2^h, \mathbf{b}_3^h) = 90°$. Compared to the initial lattice, the reciprocal lattice is rotated by $\angle(\mathbf{b}_1^h, \mathbf{a}_1^h) = 30°$. This is consistent with the introduction of directions in the hexagonal notation, showing that the $[10\bar{1}0]$ direction in the hexagonal notation is rotated by 30° with respect to the $\mathbf{a}_1^h$ axes.

Using equations (3.17) for the transformation of the reciprocal lattice in the hexagonal coordinate system, the indices $(h\,k\,l)^h$ of a reciprocal lattice point in this coordinate system can be related to the indices $(h'\,k'\,l')^c$ in the cubic system via the matrix transformation [81]:

$$\begin{pmatrix} h \\ k \\ l \end{pmatrix}_h = \begin{pmatrix} 1/2 & 0 & -1/2 \\ -1/2 & 1/2 & 0 \\ 1 & 1 & 1 \end{pmatrix} \begin{pmatrix} h' \\ k' \\ l' \end{pmatrix}_c \tag{3.18}$$

and the inverse relation

$$\begin{pmatrix} h' \\ k' \\ l' \end{pmatrix}_c = \begin{pmatrix} 2/3 & -2/3 & 1/3 \\ 2/3 & 4/3 & 1/3 \\ -4/3 & -2/3 & 1/3 \end{pmatrix} \begin{pmatrix} h \\ k \\ l \end{pmatrix}_h \tag{3.19}$$

It is common to add the third index $i = -(h + k)$ for the description of the reciprocal space vectors in the hexagonal surface coordinate system, compare the concept introduced for the directions in the real space lattice [5]. Figure

---

[5] For the description of a vector in reciprocal space, the third index i can not be visualized by an additional vector as shown in the real-space representation of fig. 3.2. However, the third index i is very convenient, because all symmetry equivalent reciprocal lattice vectors can be obtained by permutations of the indices (h,k,i) and (-h,-k,-i).

3.5 schematically displays the relation between real and reciprocal space in the hexagonal coordinate-system.

Throughout this text, we will use notations $(\mathrm{h\,k\,l})^c$ with the superscript c if the indices refer to the cubic coordinate system of the bulk material and notation $(\mathrm{h\,k\,i\,l})^h$ with four indices and superscript h if we refer to the hexagonal surface-coordinate system of the cubic lattice.

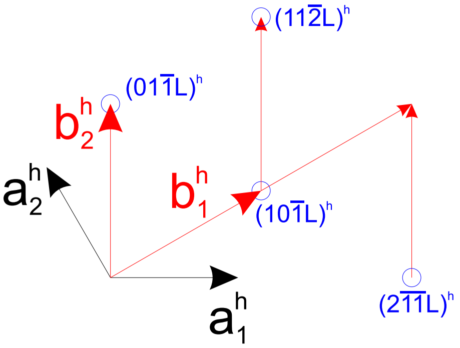

Figure 3.5: Relation between real lattice ($\mathbf{a}_1^h$, $\mathbf{a}_2^h$) and reciprocal lattice ($\mathbf{b}_1^h$, $\mathbf{b}_2^h$) in the hexagonal coordinate system. Exemplarily, four reciprocal lattice points are shown. They correspond to planes with the same indices.

Figure 3.5 shows the arrangement of reciprocal lattice vectors in the $(\mathrm{h\ k})^h$ plane. Possible Bragg reflections line up along *truncation rods* perpendicular to this plane along the L direction, and the structure factors F determine the position and intensity of allowed Bragg reflections. For a given choice of basis vectors of the reciprocal coordinate system, which can for example be given by the orientation of the substrate, zinc-blende type NWs may grow in the same orientation (*non-twinned*) or *twinned*, both structures having different positions of allowed Bragg reflections in reciprocal space. The resulting positions of allowed Bragg reflections for both ZB orientations and the WZ structure are sketched in figure 3.6 for different truncation rods.

Whereas the in-plane structure of the wurtzite lattice is equivalent to the zinc-blende one, the c axis is by a fraction of $2/3$ shorter than the native c axis of the zinc-blende structure (cf. figure A.1). Consequently, the reciprocal lattice vector $\mathbf{b}_3^{WZ}$ of the WZ structure is $3/2$ longer than $\mathbf{b}_3^h$ of the ZB structure in the surface coordinates. Hence, the reciprocal lattice points of the WZ structure are found at multiples of $1.5\,L$ in the surface coordinate system. To distinguish the different length of the $\mathbf{b}_3^{WZ}$ vector, the corresponding indices are denoted as $(\mathrm{h\,k\,i\,l})^{WZ}$ with superscript WZ.

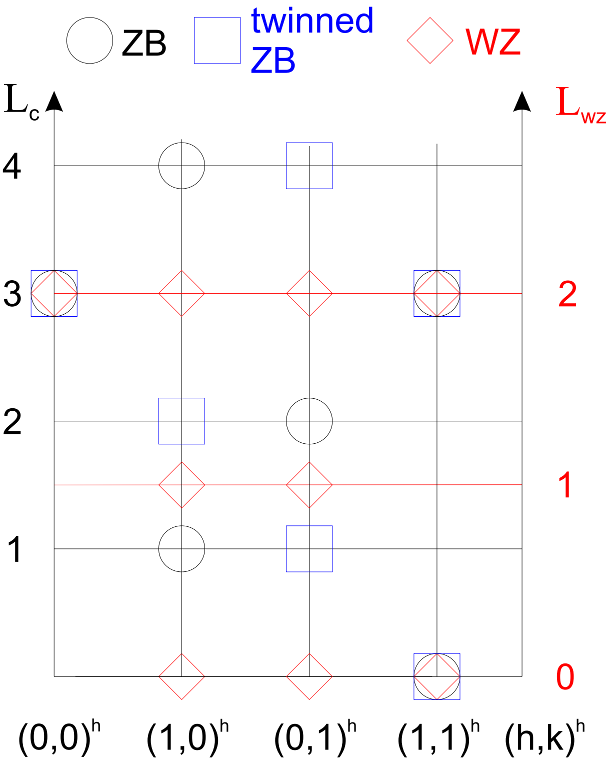

Figure 3.6: Locations of Bragg peaks of the zinc-blende, twinned zinc-blende and wurtzite structure on different (h,k,l)-rods in the surface coordinate system. Due to the different c lattice-parameter, Bragg peaks of the wurtzite structure arise at multiples of 1.5 in the coordinate system of the ZB phase. (adapted from [81])

Diffraction from structures with arbitrary stacking sequence

In nanowires grown along the cubic [1 1 1] direction often stacking faults are observed (cf. section 2.3). In this case, usually no strictly periodic structure is obtained, and the definition of unit-cells for stacking sequences 'ABCABC' or 'ABAB' breaks down. Hence, equation (3.12) can not directly be used for the calculation of the diffracted intensity. Instead, it is convenient to rewrite (3.12) for the specific arrangement of atoms. For a finite number of atoms, equation (3.12) can explicitly be written as.

$$A\,(\mathbf{q}) \propto \sum_{\text{atoms}\,n} f_n(\mathbf{q})\, e^{i\,\mathbf{q}\cdot\mathbf{r}_n} \tag{3.20}$$

We now rewrite the sum in the above equation in order to retrieve an expression that depends on the stacking-sequence of monolayers in the nanowire. To be able to calculate the scattered intensity from an arbitrary arrangement of layers, we first note that the origin of the coordinate system can be chosen arbitrarily, as a constant offset of all atomic position leads to a constant phase-shift at a given value of $\mathbf{q}$ that can not be observed in the intensities.

In general, any nanowire is composed by M monolayers stacked in a distance $d_{111} = a^c/\sqrt{3}$ above each other. Each monolayer consists of a Ga and an As atom, displaced by a quarter of the hexagonal unit-cell ($d(\mathrm{Ga}-\mathrm{As}) = \sqrt{3}a^c/4$) along the growth direction direction. In addition to the vertical displacement, the atoms in subsequent monolayers are shifter laterally with respect to each other, depending on the stacking. Figure 2.4 depicts the three different arrangements of atoms in layers of type A, B and C, respectively. Compared to the first layer, which we arbitrarily define as being of type A, the layers B and C are shifted laterally by the vectors $\mathbf{s}_B = \left(\frac{2}{3}\,a^h\,,\frac{1}{3}\,a^h\,,0\right)^h$ and $\mathbf{s}_C = \left(\frac{1}{3}\,a^h\,,\frac{2}{3}\,a^h\,,0\right)^h$ in the hexagonal surface-coordinate system, respectively. The position $\mathbf{r}_n = \mathbf{r}_{in-plane} + \mathbf{r}_{plane}$ of each atom can thus be decomposed into a vector lying in the hexagonal close packed plane $\mathbf{r}_{in-plane}$ and the position of the plane with respect to the origin, which we can define as the center of the first atomic layer of the NW:

$$\mathbf{r}_{plane} = m\,d_{111}\hat{\mathbf{c}} + \mathbf{s}_m, \text{ with } \mathbf{s}_m = \begin{cases} \mathbf{0} & \text{layer m is of type } A \\ \left(\frac{2}{3}\,a^h\,,\frac{1}{3}\,a^h\,,0\right)^h & \text{layer m is of type } B \\ \left(\frac{1}{3}\,a^h\,,\frac{2}{3}\,a^h\,,0\right)^h & \text{layer m is of type } C \end{cases} \tag{3.21}$$

Here, m is an integer number counting the MLs in the NW. Using this definition for the positions of the atoms, we obtain

$$A\,(\mathbf{q}) \propto \sum_{\text{bilayers}} \left(\sum_{\text{atoms}} f_n(\mathbf{q})\, e^{i\,\mathbf{q}\cdot\mathbf{r}_{in-plane}} \right) e^{i\,\mathbf{q}\cdot\mathbf{r}_{plane}} \tag{3.22}$$

We now assume that apart from this lateral shift, each layer of atoms is identical to the previous one and write

$$A\,(\mathbf{q}) \propto S_{\text{layer}}(\mathbf{q}) \sum_{m=0}^{N} e^{i\,\mathbf{q}\cdot(m\,d_{111}\hat{\mathbf{c}}+\mathbf{s}_m)} \tag{3.23}$$

with the in-plane structure factor $S_{\text{layer}}(\mathbf{q})$ containing the information about the lateral arrangement of the atoms in the bilayers. For our purpose this approximation is sufficient, but the exact orientation of the nanowire's side facets is neglected. In fact, different types of facets can be observed in NWs [34, 85] and they play a vital role in the growth process, as the surface energy of the side facets is one of the most important parameters in the kinetic description of NW growth [51, 38].

Equation (3.23) allows us to determine Bragg reflections that are independent from the exact stacking-sequence and hence stacking-faults. If we use the translation vectors $\mathbf{s}_B$ and $\mathbf{s}_C$, we realize that the stacking sequence leads to phase-factors in the amplitude in the form of $\phi_B = e^{i(2\pi/3)(2h+k)}$ or $\phi_C = e^{i(2\pi/3)(h+2k)}$, respectively. This terms vanish, whenever

$$h - k = 3N \quad N \in \mathbb{Z} \quad : \text{reflection independent of stacking faults} \tag{3.24}$$

All reflections for which (3.24) does not hold are sensitive to stacking faults and depending on the reflection and the exact stacking-sequence, they broaden in reciprocal space [145, 7]. For a coherent illumination of a single nanowire containing stacking faults, the phase shifts lead to a complex interference pattern (*speckles*)[43], as will be observed in section 4.4.

3.4 Experimental realization

The most appropriate tool to perform x-ray scattering and diffraction measurements from small samples with high accuracy and statistics is the use of third generation synchrotron radiation. Here, x-ray radiation is generated in a dedicated electron storage ring, making use of the fact that accelerated electrons emit radiation. This happens whenever their path is bend, either in a *bending-magnet* used to force the electrons around the circular synchrotron, or in dedicated *insertion-devices* installed on straight sections of the storage ring. In this *wigglers* or *undulators*, an alternating series of opposite magnets is used to force the electrons on an undulating track, enhancing the intensity of the radiation emitted in the forward direction. General introductions to synchrotron radiation can be found in [5, 94]. Prior the experimental station, x-ray optical elements are used to select a wavelength of the radiation for the experiment or to shape the beam by focussing elements or apertures. For the former, pairs of Bragg reflections on highly perfect crystals (often silicon) are used in order to obtain a monochromatic x-ray beam for diffraction experiments. The working principle of focussing elements and the general layout of the experimental station are discussed in the following.

Focussing synchrotron radiation

The conventional size of the synchrotron x-ray beams at the position of the sample is in the order of several 10 to 100s of μm. Whereas this beam size is convenient to study ensembles of nanostructures on a surface, the x-ray beam needs to be focussed down to the nm regime in order to probe single nanostructures. Besides the requirements of a small focal size, important properties like the coherence of the x-ray beam should not be affected and the setup should allow for a reliable alignment. A common way to achieve small focal spots is the use of fresnel zone plates (FZPs) [65] or compound refractive lenses (CRLs) [132]. Whereas the former uses the diffraction of the electromagnetic waves, the latter relies on geometrical refraction effects to focus the x-ray beam.

Here, a FZP has been employed to focus the x-ray beam on the sample position. Figure 3.7 shows a SEM image of a FZP similar to the one used in the experiments and a sketch of the experimental setup. In general, a FZP can be regarded as a circular diffraction grating [105]. It is composed by *zones* of decreasing radius r_n designed in such way, that the optical path difference between waves emerging from subsequent zones towards the focal point is $\lambda/2$. The out-of-phase portion of the wave in every second zone is either absorbed or phase-shifted to add up constructively at the focal point. For wavelengths much smaller than the focal distance, the radius of the n'th zone is given by $r_n = \sqrt{n\,f\,\lambda}$ and the width of the n'th zone is $\Delta r_n = r_n/(2n)$. The minimum, *diffraction limited* focal size Δs of the first order diffracted beam that can be achieved for a given FZP can be calculated using the Rayleigh-criterion to be

$$\Delta s = 1.22 \Delta r_n \tag{3.25}$$

For a given wavelength, the FZP creates several focal points, located at the focal distance f and odd-integer fractions $\pm f/3$, $\pm f/5$.... To produce a well defined beam that illuminates the sample, in an experimental realization all but the first diffraction orders are blocked by a spherical order-sorting aperture (OSA).

Figure 3.7 shows a sketch of the experimental setup with a central beamstop and the OSA, placed before and after the FZP, respectively. Using this setup, all higher diffraction orders and the transmitted direct beam are blocked by the apertures. Prior the experiment, special care has to be taken in order to align all elements on the optical axis. As the focal length depends on the used x-ray wavelength, the correct distance can be determined experimentally before the experiment by determining the minimum beam size as function of FZP-sample distance. Unavoidably, focussing the x-ray beam to a smaller size leads to a large divergence of the incident x-ray beam if the full aperture of the FZP is illuminated. The effect on the resolution in reciprocal space is discussed in appendix B.

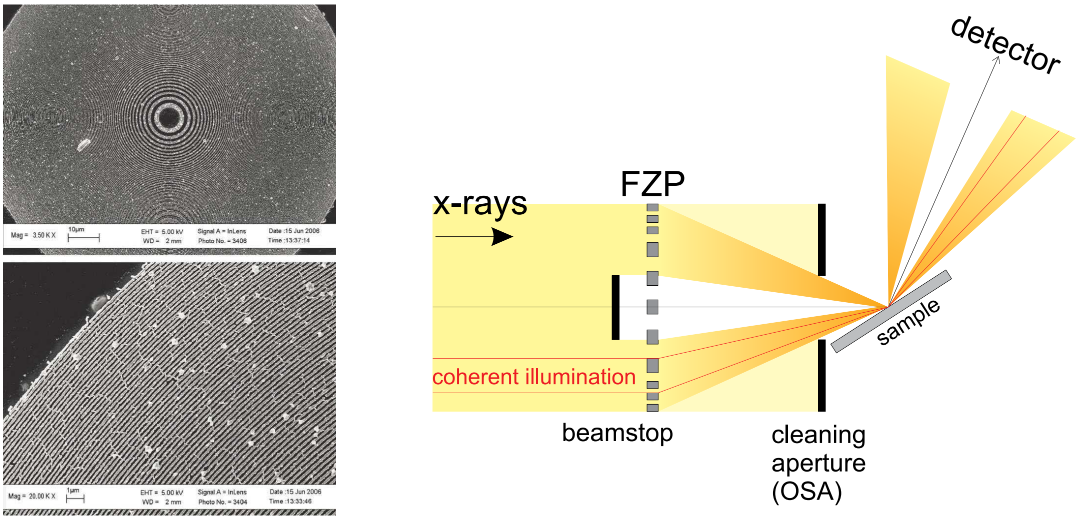

Figure 3.7: (left) Scanning electron micrographs (overview and outermost region) of a Fresnel zone plate similar to the one used in the experiment. The zones are made of Au with a height of 1 μm and an outermost zonewidth of 100 nm [from [65]]. (right) Schematic view of the experimental setup. The FZP focusses the beam on the sample. A central beamstop and a circular aperture are used to block the transmitted beam and all but the first diffraction order. Slits in front of the FZP can be used to select the coherent volume of the synchrotron beam (red).

The FZP used in the experiments in this work has been made of Au with 200 μm diameter and 100 nm outermost zone width. For a coherent illumination, a coherent size of 60 $\mu\text{m} \times 20\,\mu\text{m}$ (vertical × horizontal), given by the properties of the synchrotron beam [31, 88], has been selected by a set of slits from the total acceptance of the FZP. As indicated in figure 3.7, this reduces the divergence of the x-ray beam[6]. The dependence of the wavefront curvature in the focal

---

[6] The sketch in figure 3.7 only illustrates the principle, but does not represent the actual situation for coherent illumination. Due to the smaller horizontal coherence length of the synchrotron beam, a segment of the FZP that is displaced along the horizontal axis is illuminated in practice, although the figure shows a segment that is displaced vertically.

plane as well as the focal spot size and focal depth as function of the selected aperture before the FZP was studied in [88], showing that the wavefront can be used for coherent diffraction experiments and that the focal depth is in the order of hundreds of μm at the used apertures (290μm focal depth for a fully illuminated FZP).

Diffractometers and diffraction geometries

As introduced in section 3.2, the diffracted intensity from crystalline objects is concentrated around distinct points in reciprocal space, and experiments are performed by adjusting the incident beam ($\mathbf{k}_i$) and the x-ray detector ($\mathbf{k}_f$) such that the momentum transfer $\mathbf{q} = \mathbf{k}_f - \mathbf{k}_i$ maps a certain region in reciprocal space around a reciprocal lattice vector $\mathbf{G}_{\mathrm{hkl}}$. For single crystalline material, this requires high accuracy and control about all degrees of freedom. Figure 3.8 depicts the general setup of a diffractometer used in the experiments. After passing the monochromator and possible other optical elements of the beamline, the x-ray beam from the synchrotron hits the center of rotation of the diffractometer, in which the sample is placed with the help of translation stages (x,y,z). Usually, three rotation axes are available for the rotation of the sample (ω, χ, ϕ). Depending on the diffractometer, additional rotation stages (goniometer movements, μ) are available to adjust small miss-orientations, for example to align the orientation of the surface normal with one the main axes. The detector is usually mounted in a distance of $\approx 1\,\mathrm{m}$ from the sample and can be rotated in both vertical (2θ) and horizontal (η) direction. Additionally, a 2-dimensional detector covers the angles (ν, δ) within the detector plane. By a precise mechanical construction, all rotation axes intersect in a common point, the *center of rotation*. In the experiment, both x-ray beam and sample (the surface or a single nanostructure) are aligned in this point as well.

Restrictions in diffraction geometry

In this work, most experiments have been performed in a quasi coplanar diffraction geometry, in which the diffracted wave $\mathbf{k}_f$ lies approximately in the plane defined by the incident x-ray beam $\mathbf{k}_i$ and the surface normal of the sample. In this geometry, the scattering angle is mainly determined by 2θ, and the angle ν (cf. fig. 3.8) is small ($\nu \lessapprox 2°$, $\eta = 0°$.) This restriction was imposed by the use of the highly-focussed x-ray beam and the required experimental setup,

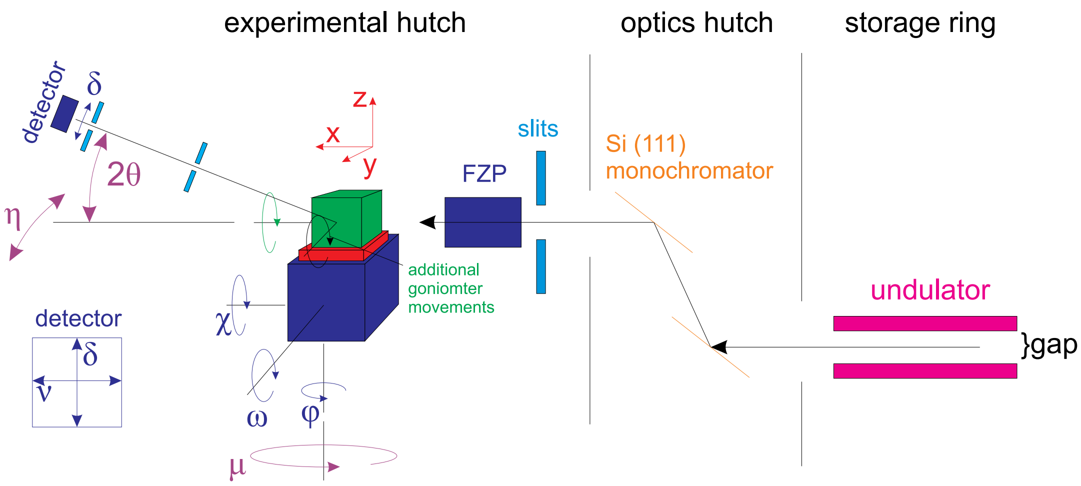

Figure 3.8: Sketch of the important beamline components and angles of the diffractometer. a monochromatic x-ray beam, produced by an undulator in the storage ring, is obtained by a crystal monochromator, for example a Si (111) channel-cut crystal. Slits or a Fresnel zone plate (FZP) define the size of the incident beam on the sample. The sample, depicted by the central cube, can be translated in all directions (x,y,z) and rotated by the angles (ω, φ, χ). The detector can be rotated in the vertical (2θ) and horizontal (η) plane. Additionally, a 2-dimensional detector covers the angles (ν, δ) within the detector plane. For horizontal scattering, an additional angle (μ) can be used. Depending on the details of the setup, some angles might not be available in an experiment. Additional components like beam monitors or attenuators have been omitted.

aiming to reduce mutual vibrations between sample and optical elements. In general, this strongly restricts the region accessible in reciprocal space and not all possible Bragg reflections can be accessed. Figure 3.9 depicts two diffraction geometries possible in this case. Besides lattice planes parallel to the sample surface (*symmetric diffraction*), lattice planes inclined to the surface can be probed in an *asymmetric diffraction* geometry, if the angle of the probed lattice plane towards the surface (Φ) is smaller than the Bragg angle θ_B of the lattice plane, fulfilling the Bragg condition either for an incidence angles of $\theta_B - \Phi$ (grazing incidence case) or $\theta_B + \Phi$ (grazing exit case, shown in the figure).

Due to the restriction $\Phi < \theta_B$ and the used x-ray energies between 8 keV and 10 keV, only a small number of all possible Bragg reflections are accessible in the

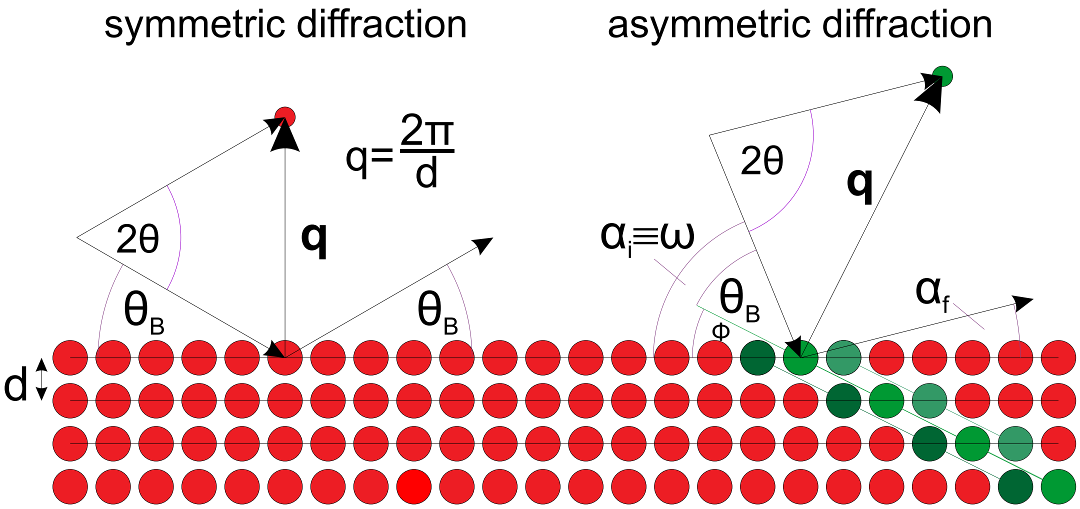

Figure 3.9: Sketch of the symmetric and asymmetric diffraction geometry. Symmetric describes the diffraction at lattice planes parallel to the surface of the crystal. In the asymmetric case, Bragg's law is fulfilled at lattice planes inclined by an angle Φ with respect to the surface, subsequently increasing or decreasing incidence and exit angles, respectively.

experiment. In the surface coordinate system introduced above, the accessible region in reciprocal space is sketched in fig. 3.10. For both $(1\,0\,\mathrm{L})^h$ and $(0\,1\,\mathrm{L})^h$ truncation rods, a region between L=7 and L=8 could be measured, giving access to two reflections allowed in the two different twin-orientations of the ZB lattice, as well as one reflection uniquely sensitive to the wurtzite structure. For the cubic zinc-blende structure, these reflections correspond to the $\{3\,3\,1\}^c$ and $\{4\,2\,2\}^c$ type of reflections, whereas the indices in the WZ notation are $\{1\,0\,\bar{1}\,5\}^{wz}$, respectively[7]. In addition, the $\{1\,1\,\bar{2}\,9\}^h$ type of reflections could be accessed, corresponding to the $\{3\,5\,1\}^c$ reflections. Compared to the $(1\,0\,\mathrm{L})^h$ type of reflections, this reflection is not influenced by the stacking sequence of the structure and allowed for all possible crystal types.

Due to the restriction to a quasi coplanar geometry, it is convenient to define a *diffractometer-related* coordinate system in such a way, that the z axis is parallel to the surface normal of the sample, the x-axis parallel to the projection of the

---

[7] Here, curly brackets around the indices are used in order to emphasize that all symmetry equivalent reflections in the hexagonal surface plane are accessible for different azimuthal orientations of the sample.

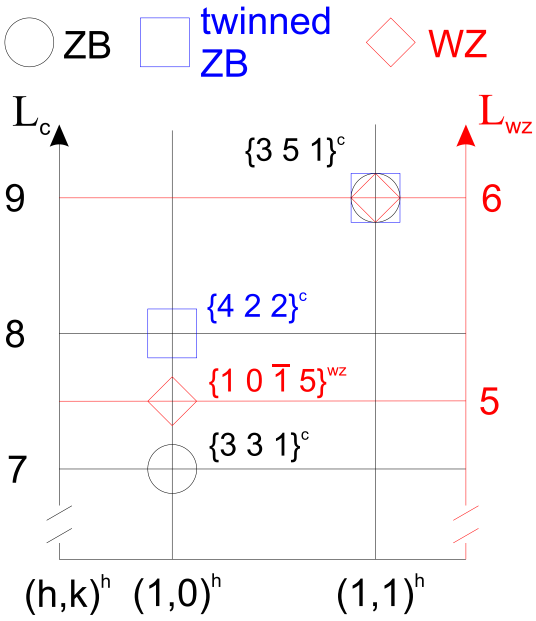

Figure 3.10: Locations of Bragg peaks of the zinc-blende, twinned zinc-blende and wurtzite structure that can be accessed in a coplanar asymmetric diffraction geometry. Both reflections sensitive to the stacking sequence $(1\,0\,\mathrm{L})^h$ as well as stacking-independent reflections $(1\,1\,\mathrm{L})^h$ can measured. Besides the location in the surface coordinate system, the cubic and wurtzite type indices are given.

incoming x-ray beam on the surface and the y direction perpendicular to this. Using the angles α_i, α_f (incidence- and exit angle of the x-ray beam on the surface) and ν (scattering angle in the detector plane perpendicular to α_f), the components of the scattering vector can be decomposed according to [108]

$$\begin{aligned} q_x &= \frac{2\pi}{\lambda}\,(\cos\,\alpha_f \cdot \cos\,\nu - \cos\,\alpha_i) \\ q_y &= \frac{2\pi}{\lambda}\,\sin\,\nu \\ q_z &= \frac{2\pi}{\lambda}\,(\sin\,\alpha_i + \sin\,\alpha_f \cdot \cos\,\nu) \end{aligned} \tag{3.26}$$

In the coplanar geometry used here, $\alpha_i = \omega$ and $\alpha_f = 2\theta - \omega$. Later on, additional diffraction experiments in a non-coplanar *grazing incidence diffraction* (GID) geometry will be performed. Details about this geometry can be found in appendix C.

Reciprocal space mapping

In most experiments performed in this work, the diffracted x-ray beam has been recorded using a two-dimensional pixel detector, allowing to simultaneously measure the intensity-distribution for a small range of 2θ and ν, respectively. According to equations (3.26), each frame taken at fixed incidence angle

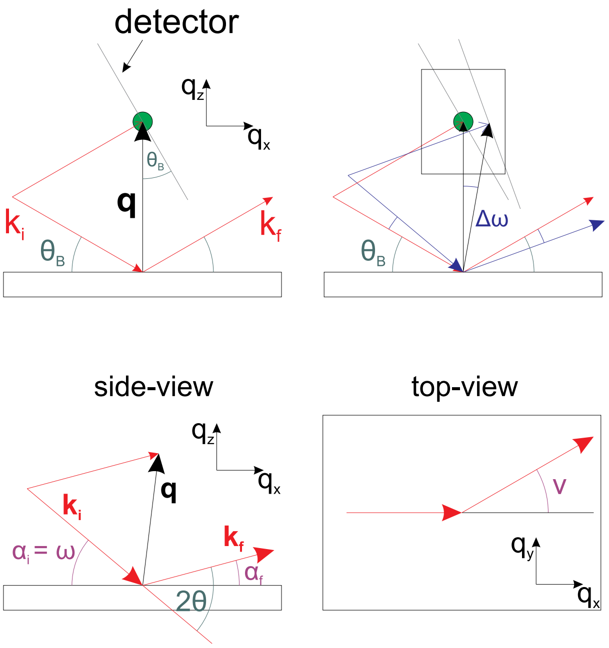

Figure 3.11: (top) Side-view of the symmetric diffraction geometry. A 1- or 2-dimensional detector covers a wide range of the scattering angle 2θ in each frame. If Bragg's law is fulfilled, this translates to an almost straight line (or plane) in reciprocal space, inclined by the Bragg angle with respect to the reciprocal lattice point. Rotation of the sample by small steps $\Delta\omega$ allows the measurement of a *reciprocal space map*. (bottom) Definition of the angles used in equ. (3.26) to decompose the scattering vector $\mathbf{q}$ in components q_x, q_y and q_z.

ω cuts a slice in reciprocal space. Therefore, subsequent frames taken at different incidence angles ω (and possible different detector positions 2θ) allow to reconstruct the 3dimensional intensity distribution in a given volume of reciprocal space [146]. This is illustrated in figure 3.11 for the case of a symmetric reflection, showing the translation of the detection volume during the rotation of the sample by a small angle $\Delta\omega$. It is important to realize that the mapping of reciprocal space using this setup is done in non-equally spaced volumetric pixels (cf. appendix B). For visualization and further analysis of the data in reciprocal space, the dataset is therefore usually gridded using a numeric algorithm on a regular spaced grid[8].

---

[8] All data processing in this work, including the transformation from angular coordinates into reciprocal space and the data visualization by gridding and rendering, has been performed within the MATLAB programming language [89].

Object-identification

In order to perform diffraction measurements on single nanoobjects, they need to be located within the focussed x-ray beam and aligned in the center of rotation. This can be done using the method of scanning x-ray diffraction microscopy [96]. In a first step, the sample is aligned in a non-focussed x-ray beam in an appropriate position, such that the nanostructures fulfill Bragg's law and the diffracted intensity can be observed on the detector. After the x-ray beam is focussed down, the sample is translated below the x-ray beam using a piezo positioning system, allowing a reliable sample alignment with nanometer resolution. Using this piezo scanner, the spatial resolved intensity distribution of the nanostructure's Bragg reflection is recorded, creating an intensity-map of the surface. The general scheme of the experimental setup equals the one shown in figure 3.7, with the addition that the sample can be translated by a piezo system of high resolution. An example of the technique is shown in figure 3.12. Fig. 3.12(a) shows a measurement around the $(3\,5\,1)^c$ reflection of GaAs nanowires grown on GaAs using a broad x-ray beam of $200\,\mu$m in diameter [9]. After identification of the nanostructure's Bragg peak (encircled region), the spatial resolved intensity distribution was measured, showing well aligned intensity maxima with periodicity of $3\,\mu$m, which corresponds nicely to the arrangement of nanowires observed in SEM images (c).

Experimental setups

ESRF

Most measurements presented throughout this work have been performed at the ID01 beamline of the ESRF synchrotron source in Grenoble, France [59]. The beamline is equipped with a dedicated setup to perform nanodiffraction experiments with the help of a focussed x-ray beam.

The x-ray beam is produced by a set of one or two undulators in the synchrotron storage ring. After the initial size of the beam has been defined by a set of slits in the optics section of the beamline, a Si $(1\,1\,1)$ monochromator is used to select the energy of the x-ray photons for the measurements. Typically,

---

[9] For more details about the measurement and the nanowires shown in the figure, compare chapter 4. The color of the figure shows the measured intensity in a logarithmic scale, as indicated by the colorbar. Later on, the colorbar is usually omitted in the figures.

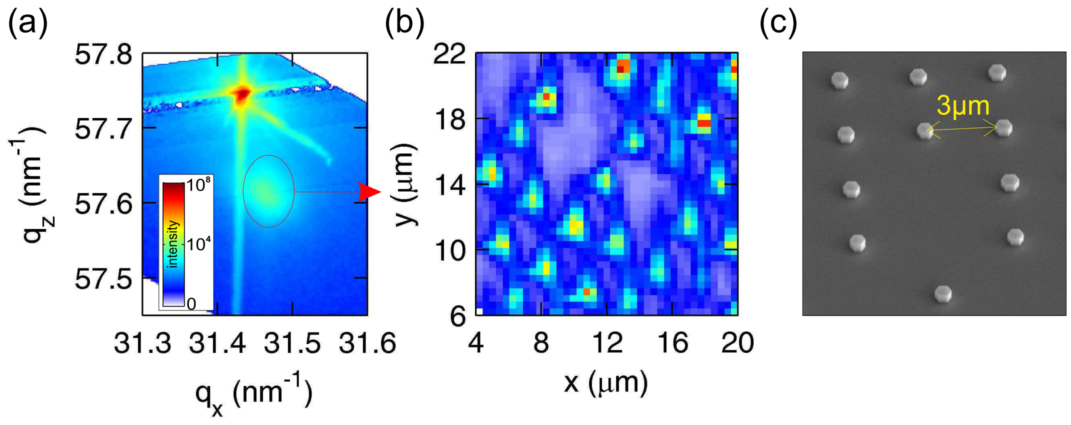

Figure 3.12: Identification of single nanoobjects with a focussed x-ray beam: (a) shows the intensity distribution around a $(3\,5\,1)^c$ Bragg reflection of GaAs nanowires grown on a GaAs substrate. Because of their different lattice parameter (compare chapter 4) they cause a separated Bragg reflection (red circle). (b) shows the intensity distribution of this region in reciprocal space measured with the focussed x-ray beam. Clearly separated spots can be identified with distance of $3\,\mu$m. (c) shows an electron micrograph of the same sample.

x-ray energies between 8keV and 10keV, corresponding to wavelengths from 1.24 Å to 1.55 Å have been used here. Behind the monochromator, a set of slits defines the size of the x-ray beam entering the experimental section of the beamline. For nanodiffraction experiments, a Fresnel zone plate with $200\,\mu$m diameter is placed at the focal distance in front of the center of rotation of the diffractometer. Together with the FZP, a central beamstop (diameter $60\mu m$) an order-sorting aperture with opening diameter of $50\,\mu$m are aligned along the optical axis, in order to block all but the first diffraction orders produced by the FZP. For most experiment, a FZP with 100 nm outermost zone width has been used, resulting in a focal length of 129 mm at a photon energy of 8 keV. The exact focal length has been optimized for each experiment by measuring the size of the focussed beam in the center of rotation using the sharp edge of a thin Au wire and determining the minimum spot size. Typical spot sizes (FWHM) between 200 nm × 200 nm and 300 nm × 400 nm (vertical and horizontal) have been achieved, depending on the properties of the the incoming x-ray beam, e.g. its energy but also quality in terms of coherence and divergence, that is affected by the other optical elements in the beamline and for example small vibrations of them, that will in turn affect the focal spot size. The FZP together with their apertures can be removed from the optical axis by a translation stage. In this case, two sets of slits define the size of the x-ray beam at the sample position. Typical sizes are 50-200 μm both horizontally and vertically.

The sample environment consists (in the newest version since 2011) of two rotational angles ω and ϕ (cf. fig. 3.8), that are mechanically decoupled from the rotations of the detector arm to avoid vibrations of the sample during movement of the detector. Nevertheless, the sample stage is mechanically coupled with the FZP, in order to avoid mutual movements between both. The sample is mounted on a x-y-z piezo stage, allowing a precise positioning of the sample in the nm range. Larger translations of the sample and alignments of the tilt angles of a conventional goniometer are realized by a hexapod below the piezo system. In all coplanar measurements presented here, the sample is mounted with the surface horizontally. In order to record the diffracted intensity, the detector-arm was equipped with a two-dimensional MAXIPIX pixel detector [111, 112], consisting of individual pixels with a size of 55μm x 55μm each and up to 516 pixels along both directions.

Figures 3.13 shows photographs of the diffratometer with indications of the optical elements. It is worth to note that the mechanical stability of the experimental setup and reliable motor-movements are of fundamental importance for nanodiffraction experiments, and substantial improvements have been achieved throughout the time spanned by the measurements reported later on.

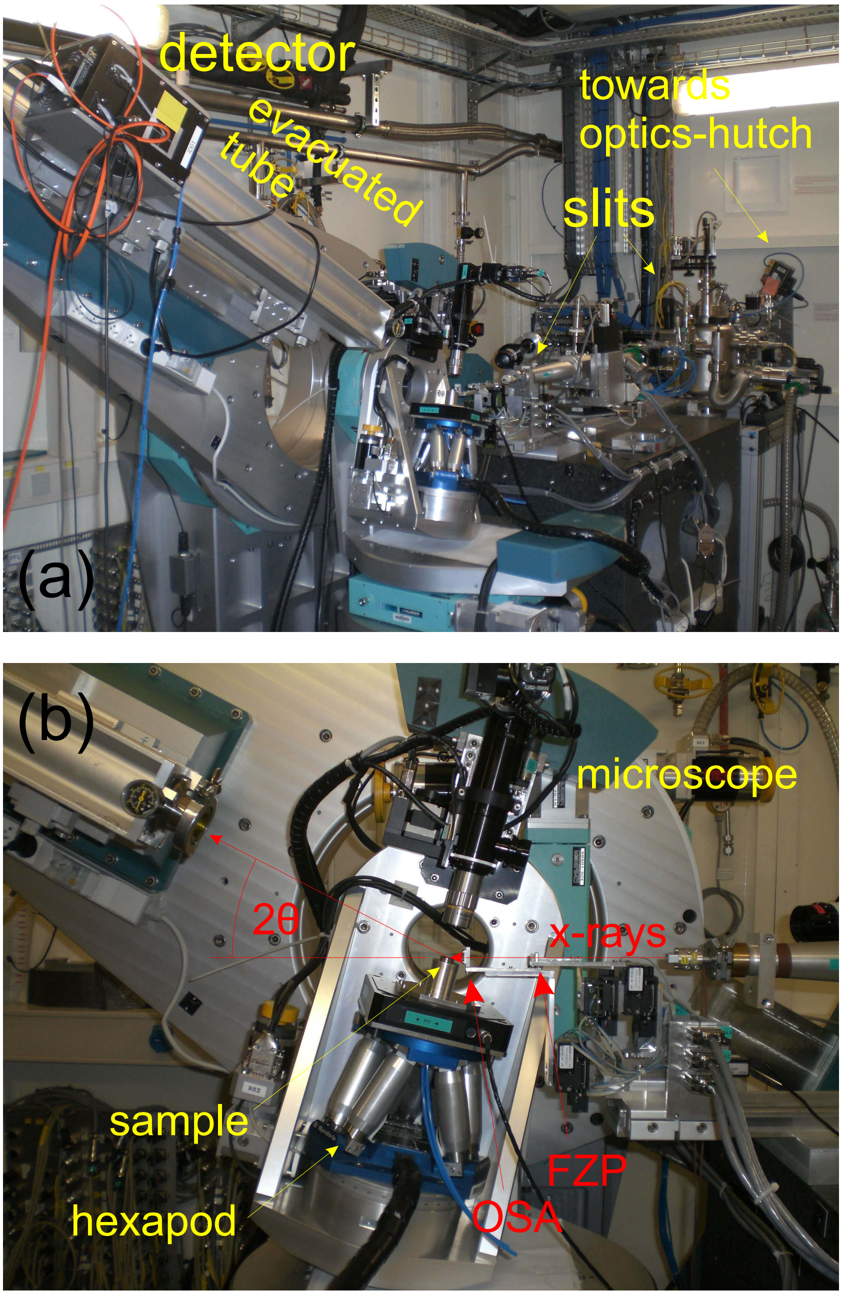

Figure 3.13: Pictures of the new diffractometer of the ID1 beamline at the ESRF synchrotron source, Grenoble. (a) shows an overview of the diffractometer, together with the slit systems in front of the sample and the detector. (b) shows a sideview of the sample-environment and the focussing optics. The directions of incident and diffracted x-rays are indicated.

PETRA

Measurements in a non-coplanar grazing incidence diffraction geometry have been performed at the P08 high resolution diffraction beamline of the PETRA III synchrotron in Hamburg, Germany. The beamline provides a highly parallel beam with accurate energy resolution, achieved by two monochromators [128]. The beamline is equipped with a high resolution Kohzu six-circle diffractometer, shown in figure 3.14. To achieve high resolution along the in-plane scattering angle in GID geometry and to prevent intensity losses due to the horizontal polarization of the incoming radiation, the sample was mounted on the diffractometer with its surface vertically, thus a detector movement along the vertical direction measures the scattering angle 2θ. In this case, a one dimensional MYTHEN detector [126] was used to measure the diffracted intensity along the exit angle direction. Good resolution along 2θ was achieved by a pair of slits behind the sample and directly in front of the detector.

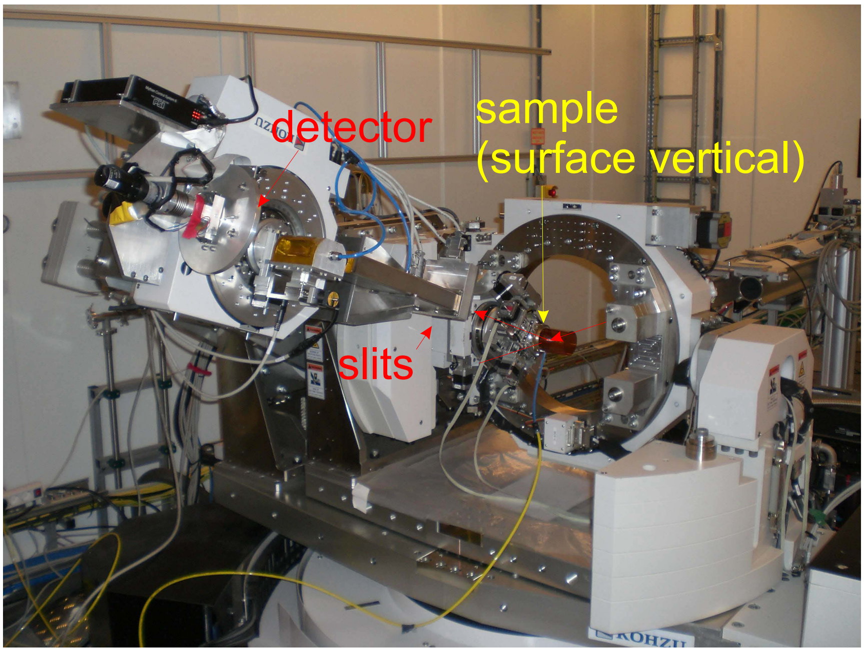

Figure 3.14: Picture of the Kohzu six-circle diffractometer installed at the P08 beamline of the PETRA III synchrotron, Hamburg [128]. For measurements in a grazing incidence geometry, the sample is mounted with the surface vertically, in order to obtain a vertical scattering geometry with σ-polarization.

4 Coherent x-ray diffraction from GaAs nanowires grown by MOVPE

In this chapter we study the structure and shape of GaAs nanowires grown in patterned arrays onto GaAs substrates using the catalyst-free growth by selective area metal-organic vapor phase epitaxy (SA-MOVPE). In section 4.1, the growth mechanism and the resulting morphology of the NWs are described. As we will see in section 4.2, the GaAs NWs have a different lattice parameter compared to the underlying GaAs substrate. The dimensions of the NWs allow to perform measurements by coherent x-ray diffraction in section 4.3, in order to determine both the shape of different NWs and to simultaneously reveal individual differences in their mean lattice parameters. Finally, in section 4.4 we will evaluate the microstructure of the NWs, exhibiting a large number of zinc-blende twin defects. Their density is estimated from coherent x-ray diffraction and electron microscopy. We find that the change in hexagonality of the resulting structure is consistent with the observed change in lattice parameters.

4.1 Growth details and description of samples

Catalyst-free GaAs nanowires have been grown by selective-area metal organic vapor phase epitaxy (SA-MOVPE) onto [1 1 1]B oriented GaAs substrates covered by a 15 nm thick amorphous SiN_x layer [10]. The silicon nitride has been deposited by plasma enhanced chemical vapor deposition (PECVD) at 300°C. Within an area of 250 x 250 $\mu\mathrm{m}^2$ the SiN_x layer was partially removed by electron beam lithography in an electron sensitive resists followed by wet chemical etching using $\mathrm{NH_4F{:}HF{:}H_2O}$ solution, defining a square shaped array of circular openings with diameters of 450 nm and lateral distances between 1 μm and 3 μm. Selective-area GaAs growth was carried out using low-pressure (50mbar) MOVPE in an AIXTRON AIX200 reactor with Thrimethylgallium (TMGa)

---

[10] The NW growth has been carried out by Hendrik Paetzelt in the Semiconductor Chemistry Group, University of Leipzig, Germany.

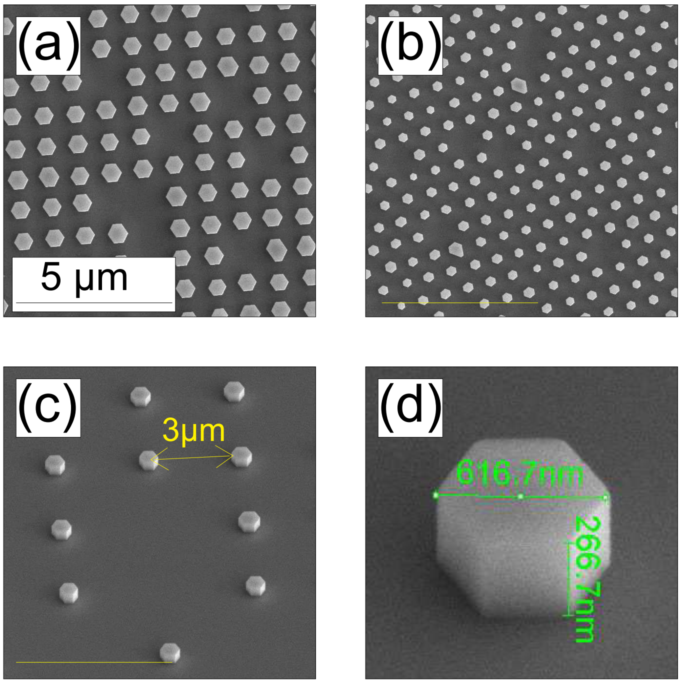

Figure 4.1: SEM pictures of different NW arrays produced. Both square (a) and hexagonal (b) arrangements have been realized. In (b), variations in size and shape of different NWs can be observed. Occasionally, NWs are missing in the patterns. (c) and (d) show NWs of the sample that has mainly been studied, exhibiting NWs with 600 nm diameter and 3 μm separation in a square array.

and Arsine (AsH_3) as group-III and group-V material, respectively. The total flow into the reactor amounted to 7 standard litres per minute (slm). The growth temperature was set to 750°C providing equally hexagonally shaped NWs. TEM measurements on selected GaAs nanowires show that the NWs grow predominantly in the zinc-blende structure containing a large number of twins[60, 61, 103].

Figure 4.1 displays SEM images of some of the grown samples, showing the variety of patterns produced. Both square (a) and hexagonal arrangements (b) with different pitch between the individual NWs have been produced. Although NWs grow well separated and with a rather uniform size distribution, several NWs are usually missing in the periodic pattern. This is attributed to an incomplete formation of openings in the mask. Also, variations in the shape between different NWs on the same sample can be observed (compare different NWs in fig. 4.1(b)), which is attributed to small differences in the initial etching procedure resulting in a non-homogenous growth. For x-ray measurements using synchrotron radiation, the sample shown in figures 4.1(c) and (d) has most extensively been studied, as this sample provides the maximum spacing of 3μm between the nanowires arranged in a square array of in total 250 μm x 250 μm.

At the time of the experiments, the focal size of the x-ray beam allowed only to clearly separate NWs for this sample. Figure 4.1(d) shows a magnified image of one of the NWs, showing the well defined formation of six $\{1\bar{1}0\}$ side facets. The direction of the side facets has been obtained from the relative orientation of the cleavage planes of the underlying substrate, and the orientation is preserved also in strongly asymmetrically shaped NWs (e.g. fig 4.1 (b)). The average height and diameter is estimated to about 380 nm and 600 nm, respectively.

4.2 Average lattice parameters

The x-ray diffraction experiments have been performed at the ID01 beamline at the ESRF synchrotron source using the nanofocus setup as described in section 3.4. At the time of the experiment, the 8keV x-ray beam was focussed down to a measured spot size of 220x600 nm^2 (FWHM vertical and horizontal, respectively) using a Fresnel zone plate placed 129 mm in front of the sample position. Including the geometrical footprint-effect, this beam size fits well with the size of individual NWs. In order to achieve an almost fully coherent illumination of the sample, the incoming x-ray beam was reduced to a size matching the transverse x-ray coherence lengths, both vertically (60 μm) and horizontally (20 μm). For ensemble-averaged measurements, the FZP was removed from the optical axes, leading to a beam size defined by a set of collimating slits.

In order to probe the average lattice parameters of the nanowires we performed measurements at the asymmetric $(3\,5\,1)^c$ reflection, equivalent to the $(1\,1\,\bar{2}\,9)^h$ reflection, which is not affected by the presence of stacking faults. The position of the bulk Bragg reflection in coordinates q$_x$ and q$_z$ is calculated according to

$$q_z = \frac{2\pi}{d_{351}} \cos(28.56°) = 57.748\,\mathrm{nm}^{-1} \quad ; \quad q_x = \frac{2\pi}{d_{351}} \sin(28.56°) = 31.434\,\mathrm{nm}^{-1},$$

taking into account the Bulk lattice parameter $a^0_{\mathrm{GaAs}} = 5.6536\,\text{Å}$. Figure 4.2 shows a 2dimensional reciprocal space map in the q$_x$-q$_z$ plane around this reflection, measured as an ensemble average of the NW array with a 100x100 μm^2 sized x-ray beam. The data was integrated along the q$_y$ direction. The intense substrate reflection is observed at the expected position, whereas a less intense peak at smaller q$_z$ can be attributed to the NWs. This peak shows a displacement of $\Delta q_z/q_z = -(0.23 \pm 0.03)\%$ along the vertical direction, indicating an average increase of vertical lattice parameter of the NWs by 0.23±0.03%. At the same time, the peak also shows a lateral lattice mismatch of $\Delta q_x/q_x = (0.1 \pm 0.05)\%$ towards a smaller in-plane lattice parameter. The values have been determined by a 2-dimensional Gaussian fit to the NWs Bragg peak. As we will see below, this average change in lattice parameter is consistent with the assumption that the presence of stacking faults, leading to a transition of the NW structure from a cubic zinc-blende one towards a more wurtzite type structure with higher hexagonality, is accompanied by a gradual change in lattice parameters.

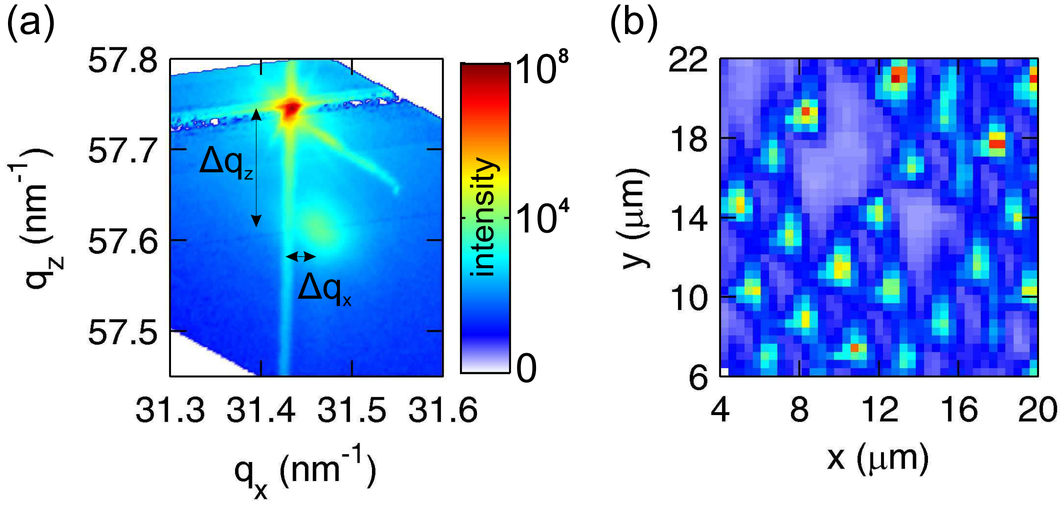

Figure 4.2: (a) Intensity distribution around the GaAs $(3\,5\,1)^c$ reflection. The NWs' Bragg peak shows an expansion of the NWs' lattice constant along the vertical and a compression along the lateral direction. (b) Spatial intensity distribution of the NW peak, showing intensity maxima in a regular array with 3μm distance. (enlargement of figure 3.12)

The FWHM of the NW reflection in figure 4.2(a) along the q_x direction is estimated to be $0.035\,\mathrm{nm}^{-1}$. If entirely caused by the NWs' size, this would correspond to a diameter of $2\pi/0.035\,\mathrm{nm}^{-1} = 180\,\mathrm{nm}$. Hence, the peak width is larger than what could be expected from the pure dimensions of the NWs and might be caused by a non-uniform distribution in average dimensions or fluctuations in lattice parameter. However, based on the SEM investigations the size distribution is much smaller than the large deviation estimated from the peak width. In the next section we will use coherent diffraction in order to compare shape and lattice parameter of different individual NWs, and will see that indeed fluctuations in lattice parameter are observed. The attribution of the additional Bragg peak to the NWs is readily verified by measuring the spatial resolved intensity distribution of this reflection, shown exemplarily in figure 4.2(b). Clearly visible is the spatial distribution corresponding to individual NWs in a square arrangement with distances of 3 μm, including positions of missing NWs as already seen in the SEM image (fig. 4.1(a)).

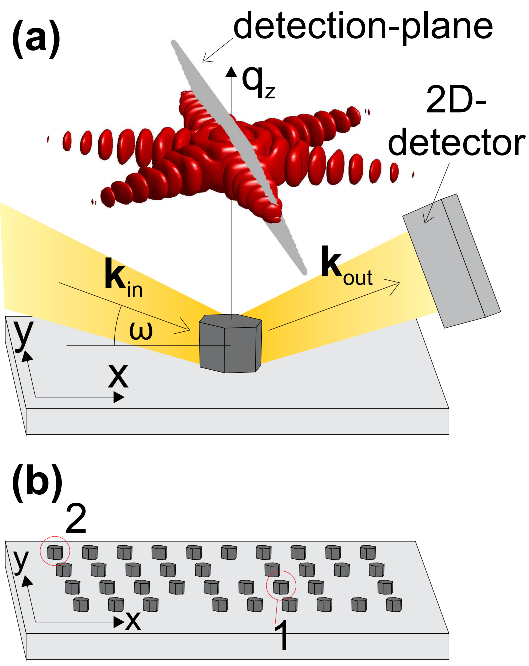

Figure 4.3: (a) Sketch of the scattering geometry used. If a single nanowire is illuminated coherently, the intensity distribution around its reciprocal lattice point corresponds to the Fourier transformation of the shape (simulation in red). The 2D detector covers an inclined detection plane in reciprocal space. (b) Two NWs have been selected for comparison, one located in the center of the array (1), one located at the edge (2).

4.3 Individual variations probed by x-ray diffraction

(published in paper [I])

Lattice parameter

In order to probe differences in the individual lattice parameters and shapes of the NWs, we measured the 3-dimensional coherent diffraction patterns around the symmetric (1 1 1) reflection of different individual nanowires. In particular, a NW in the center of the pattern was compared to a NW at the edge of the NW array (compare fig. 4.3(b)). Figure 4.3(a) shows a sketch of the scattering geometry used. The focussed x-ray beam illuminates a single NW under an incidence angle ω close to the GaAs (111) Bragg angle. The center of the 2-dimensional MAXIPIX detector was placed at a fixed scattering angle 2θ, covering a 2D surface in reciprocal space (grey shaded plane in fig. 4.3(a)). The full 3D intensity distribution is obtained by rotating the incidence angle ω through the Bragg position and subsequent recording of 2D intensity images at each position [146]. For every image, the intensity in reciprocal space coordinates $I(q_x, q_y, q_z)$ of each detector-pixel is obtained from the incidence angle ω and the two detector coordinates defining the in-plane and out-of-plane scattering angles according to equations (3.26). Finally, the slightly non-equally spaced data in q-space was binned on a regular spaced 3D array in reciprocal space from which data-visualisation and the extraction of slices through the intensity distribution, e.g. $I(q_x, q_y, q_z = \text{const.})$ were obtained.

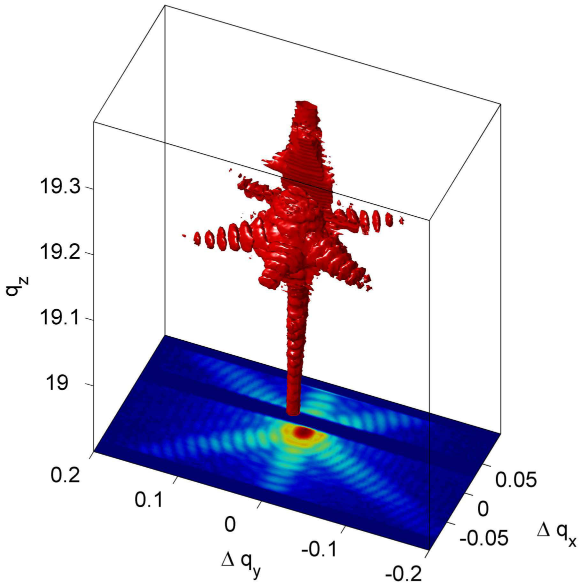

Figure 4.4: 3-dimensional coherent diffraction intensity distribution of a single nanowire close to the GaAs $(111)^c$ reflection. The red structure represents an iso-intensity surface, the map below shows a cut at constant q_z through the peak from the nanowire. The region containing the substrate's Bragg-maximum is missing in the data. All units in nm^{-1}.

Figure 4.4 shows the 3D plot of an iso-intensity surface in reciprocal space, measured at a single NW in the center of the patterned area around the GaAs $(1\,1\,1)^c$ reflection. Unavoidably, also the Bragg peak of the substrate, located at a slightly larger q_z, is excited in this case. This gives rise to the vertical crystal truncation rod of the GaAs substrate, superimposed by interference fringes from the finite NW height. Because the intensity of the substrate peak exceeds the signal of NW by several orders of magnitude, it had to be blocked due to the limited dynamic range of the detector, leading to the area of missing data, visible in the lower part of figure 4.4, showing a slice of the diffraction pattern above through the NW signal.

Due to the coherent illumination, the recorded diffraction pattern is proportional to the square modulus of the Fourier transform of the electron density of the selected NW. It shows characteristic oscillations due to its finite size and almost perfect hexagonal symmetry in the plane parallel to the surface.

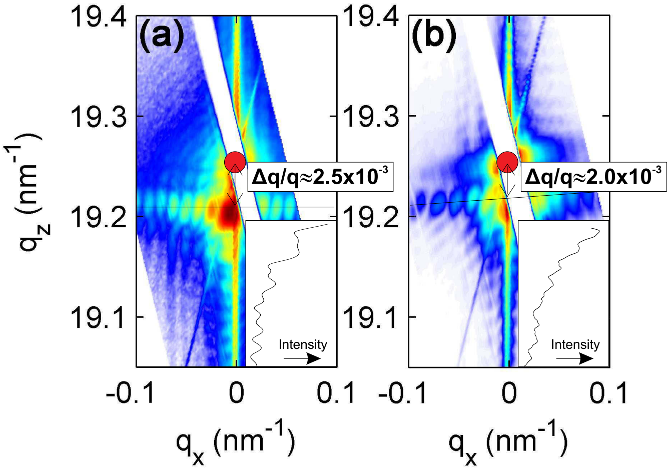

Figure 4.5: Cut in the q_x-q_z plane through the $(111)^c$-diffraction signal of the wire in the center (a) and at the edge (b). Vertical lattice mismatch, tilt of the NWs diffraction signal and vertical size are different in both cases. Insets show interference fringes along the CTR, measuring the height of the NWs.

As suggested by the large width of the $(3\,5\,1)^c$ reflection discussed above, fluctuations in the individual lattice parameters of different NWs can be expected. At the time of the experiment, only the symmetric $(1\,1\,1)^c$ reflection could be probed for different individual NWs, thus only the average vertical lattice parameter can be compared. Figure 4.5 shows a cut in the q_x-q_z plane through the 3D NW pattern around the GaAs $(1\,1\,1)^c$ reflection for a NW measured in the center (a) and at the edge (b). It displays a modulated intensity along the CTR (insets) measuring the height, L, of the selected NW by $L = 2\pi/\Delta q_z$. For the central NW we measure a value of L≈400 nm which is in good agreement with the height of 380nm measured in figure 4.1(d), taking into account the sample inclination of 45° used for the SEM image. The respective height of the NW at the edge is L≈360 nm, i.e. 10% smaller than found for the central NW.

In addition, the tilt of the facet CTRs with respect to the vertical direction in figure 4.5(b) shows that the side-facets of the NW at the edge are slightly tilted with respect to the substrate surface, oriented perpendicular to the vertical CTR. This inclination angle is in the order of 4°. Furthermore we find that the lattice mismatch, measured by the distance between the substrates Bragg peak (indicated by the circle) and the NW's Bragg peak, differs slightly for both NWs. It is $\Delta q_z/q_z = -(0.25 \pm 0.02)\%$ for the central NW and $\Delta q_z/q_z = -(0.20 \pm 0.03)\%$ for the NW at the edge.

Nanowire-shape

In order to analyze the shape of the NWs, a horizontal cut through the center of the nanowires diffraction pattern was extracted by summation of 8 horizontal slices (total extension along q_z: $0.018\,\text{nm}^{-1}$) in the q_x-q_y plane from the 3D intensity distribution.

Figures 4.6 and 4.7 show the extracted horizontal slices of the NW measured in the center and at the edge of the array, respectively. As immediately visible, the diffraction pattern shown in figure 4.6(a) exhibits a shape close to that of a perfect hexagon. All the CTRs originating from the six hexagonally arranged side facets show equally spaced interference fringes. In contrast, the pattern taken at the edge of the array (fig. 4.7(a)) displays a non-perfect, more deformed, hexagon. Here, the spacing between interference fringes varies among the different CTRs. The respective diameters D of the hexagon can be estimated from the distances of interference maxima, $\Delta q_{||}$, along a CTR by $D = 2\pi/\Delta q_{||}$. We obtain a diameter of about 500 nm for all six CTRs of central NW, but two different diameters, i.e. 400 nm and 470 nm, for the NW at the edge. The high quality of the data and the only small deviations from a hexagonal shape observed in the reciprocal space maps allows an easy estimation of the object's shape based on a simulation of the diffraction pattern. As model, a regular or distorted 2dimensional hexagon with homogeneous density and diameters D_i along the three hexagonal directions was used. The diffracted intensity in the vicinity of the reciprocal lattice point is obtained from the squared modulus of a 2D Fourier transform. The model parameters D_i were varied to find minimum deviation from the experiment. Figures 4.6(b) and 4.7(b) shows the simulated reciprocal space patterns together with the shape of the models indicated by black insets. Even the small intensity features between the main facet-streaks are well reproduced and one clearly can distinguish between regular and distorted NW shape. The NW in the center is an almost perfect hexagon with a diameter of 500 nm, corresponding to a distance between opposite corners of 580 nm. Contrary, the NW at the border of the array (fig. 4.7(b)) is considerable smaller and asymmetric, featuring four larger and two shorter side planes.

Phase retrieval analysis

Although the intuitive analysis of the object's shape using Fourier transform gives fast access to results in this case due to the rather simple structure of the system, the strength of *coherent diffraction imaging* lies in the possibility of a model-free, direct imaging of the electron density of the object. The extracted slices at constant value of the vertical momentum transfer q_z contain the information about the scattering potential (i.e. the electron-density) of the diffracting nanowire and therefore the shape. Measuring close to Bragg reflections, additionally opens opportunities for the measurement of atomic displacement fields within individual nanocrystals [107, 122, 99]. Here, a complex-valued object is considered, the amplitude of which represents the electron density of the object and its phase the displacement field projected onto the probed Bragg reciprocal space vector as introduced in section 3.2. Because the diffraction pattern has been recorded using a coherent x-ray beam and a high resolution in reciprocal space, fulfilling the oversampling criterion [93], an algorithm-based reconstruction of this scattering potential, termed *coherent diffractive imaging*, is possible. This method allows the reconstruction of the phase information of the scattering potential, that is lost during the measurement and therefore prevents a direct inversion of the diffraction pattern. This problem of *phase retrieval* can be accessed through several approaches and a very successful approach is the *Gerchberg Saxton (GS) algorithm.* The GS algorithm was introduced in 1972 in order to retrieve the phase of an object, assuming that its diffraction amplitude and also the absolute value of the scattering potential are known [49]. In 1982, it was extended by Fienup et al. to the case that only the diffracted amplitude is measured and certain constraints are known about the object, leading to the reconstruction of both absolute value and phase of the scattering potential. The algorithms introduced by Fienup are known as *error-reduction* (ER) and *hybrid input-output* (HIO) algorithms[45]. The principle of the ER-algorithm is shown in figure 4.8. Based on an initial guess of the object's electron density and a random phase, the diffracted amplitude and phase are simulated using a Fourier transformation according to equation (3.15). The initial guess of the object's

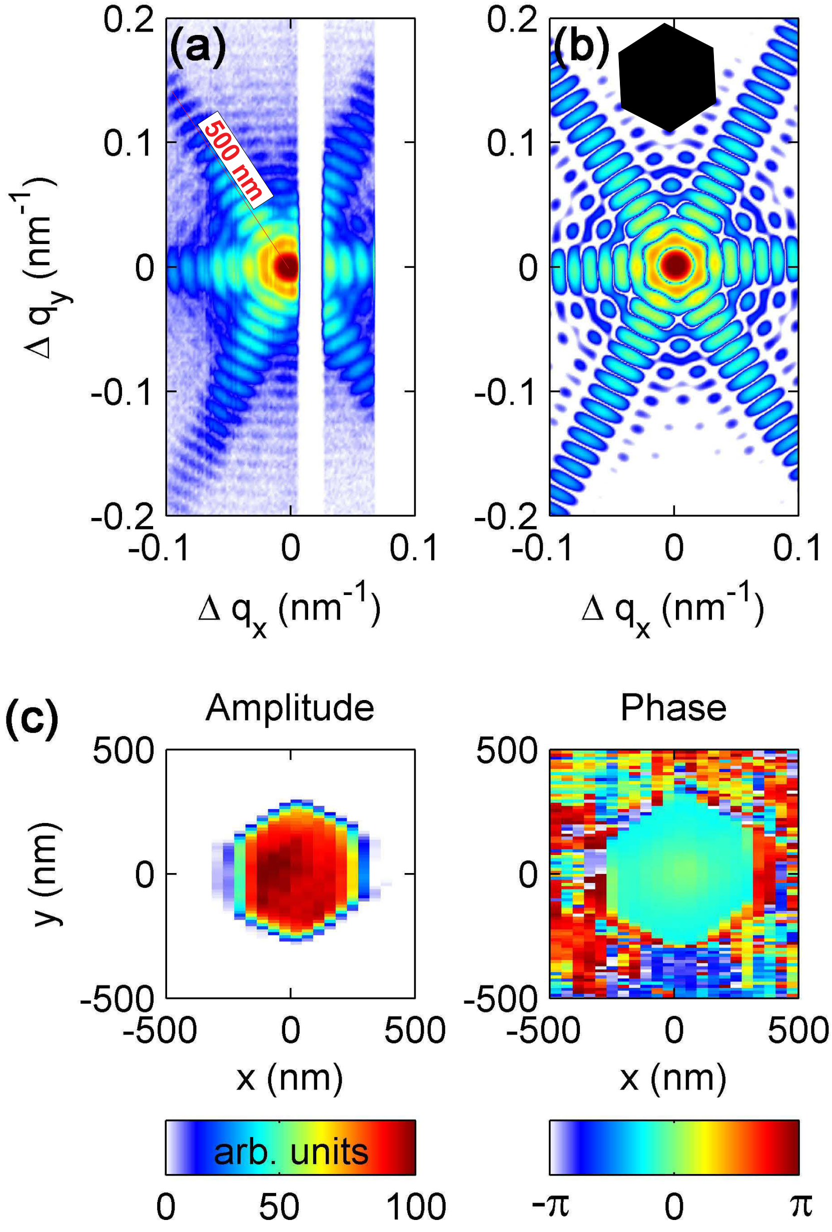

Figure 4.6: (a) Cut at constant q_z through the $(111)^c$-signal from a nanowire in the center of the array. Interference fringes measure a size of 500 nm. (b) Simulated intensity distribution obtained from 2D FFT of a homogeneous hexagon (black inset) (c) Amplitude and phase of the diffracting NW obtained by phase-retrieval analysis of the data shown in (a).

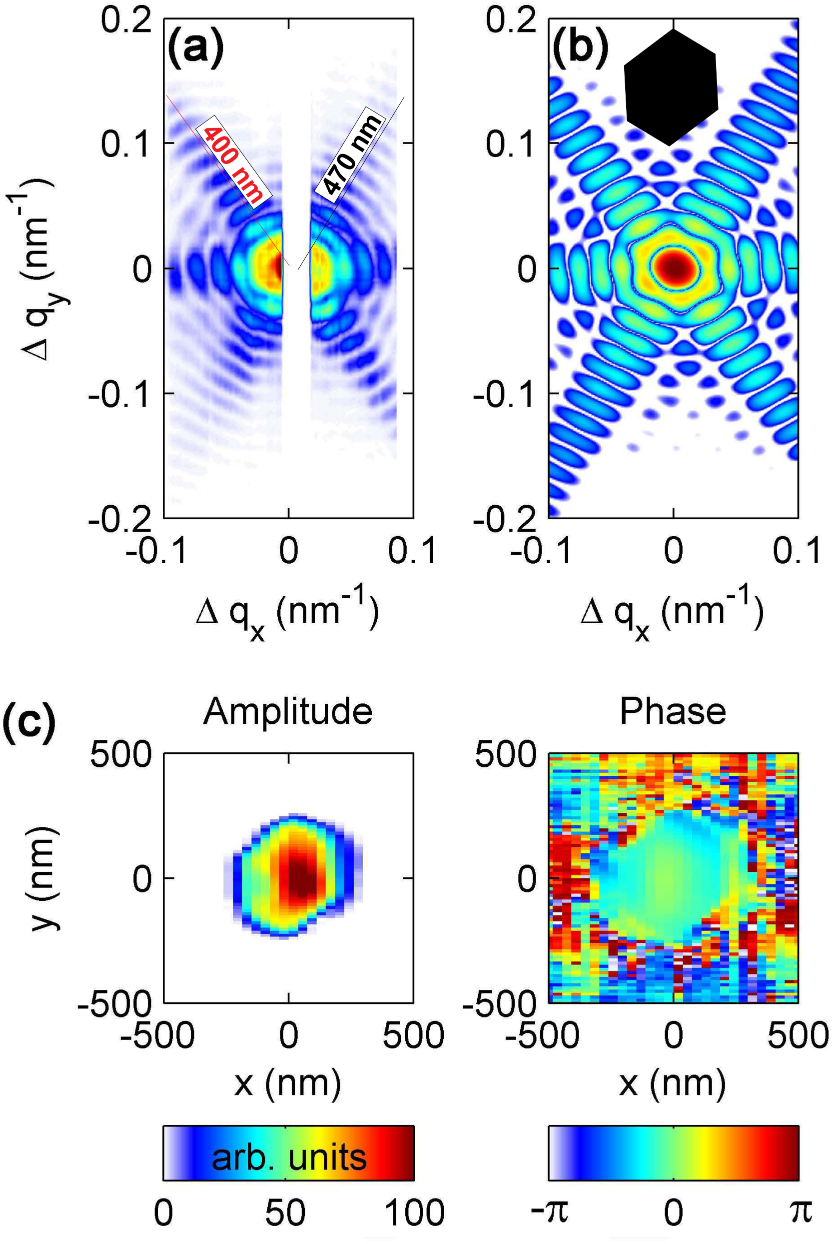

Figure 4.7: (a) Cut at constant q_z through the $(111)^c$-signal from a nanowire at the edge of the array. Interference fringes measure a inhomogeneous diameter between different facets. (b) Simulated intensity distribution obtained from 2D FFT of a homogeneous hexagon (black inset) (c) Amplitude and phase of the diffracting NW obtained by phase-retrieval analysis of the data shown in (a).

density is frequently taken from the Fourier transformation of the measured diffraction pattern, which is the autoconvolution function of the object itself.

Once the diffraction pattern is simulated, the simulated amplitude can be compared with the measured one (given by the square-root of the intensity), measuring the overall quality of the simulation. As long as measurement and simulation do not coincide below a certain level, a loop through the algorithm is performed:

The simulated amplitude is replaced by the measured amplitude, while the phase remains unchanged. This replacement defines the constraints in reciprocal space. A back-Fourier transformation is then applied in order to retrieve the magnitude and phase of the scattering potential. In order to make the algorithm converge, constraints in real space have to be applied next. The most vital one is the constraint of a limited *support*, i.e. the knowledge that the scattering object does not exceed a certain size. In this case, all simulated amplitude outside the *support* is set to zero, and the iteration is continued by calculating the new quantities in reciprocal space. One problem of this approach is that the resulting image obtained by the algorithm is better, the better the support is known, i.e. a high degree of *a priori* knowledge about the object is necessary. This drawback can be overcome by subsequently *shrinking* the support by creating the support from a threshold of the calculated amplitude itself as introduced by Marchesini et al. [80].

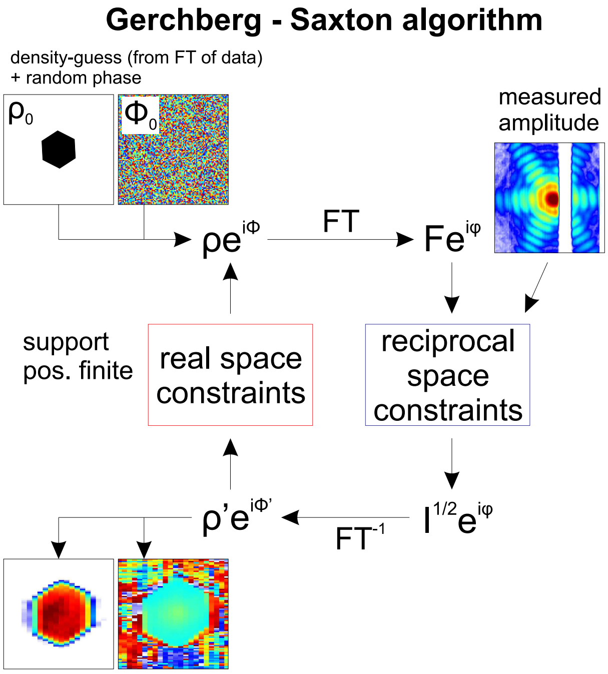

Figure 4.8: Sketch of the Gerchberg-Saxton algorithm. Starting from an initial guess of the electron density and a random phase, the diffracted amplitude is simulated and the amplitude replaced by the measured one (constraint in reciprocal space). After inverse Fourier transformation, constraints in real space are applied, e.g. a known finite size of the object (support). The algorithm converges towards the amplitude ρ' and phase ϕ' of the object.

In order to retrieve the object directly from the measured data, we used a combination of standard phase retrieval algorithms, namely error reduction (ER), hybrid input-output (HIO) and shrink-wrap (SW) [80][11]. The algorithms were applied directly on the 2D data shown in figures 4.6 (a) and 4.7 (a), defining a 2D phasing problem. In the algorithms, both amplitude and phase in real space were let to evolve free, with no other constraint apart from the necessary support constraint [45]. An initial support was assumed from the autoconvolution function, obtained through inverse Fourier transformation of the measured intensity pattern. Successive iterations of 50 times the ER algorithm followed by 2000 times the HIO algorithm were performed. The SW method was applied every 20 iterations of the HIO algorithm, following the scheme described in [80]. This approach allowed the support to progressively shrink to a size slightly larger than the reconstructed object. The performance of the algorithm was considerably improved with the use of the SW approach in comparison with a classical iteration of ER and HIO algorithms. Finally, 50 iterations of the ER algorithm were performed, making a total of 4150 iterations. Following this procedure, we performed 70 reconstructions starting with different sets of random phases each time and we averaged the complex-valued solutions, as reported by Diaz et al. [32].

Figures 4.6(c) and 4.7(c) show the obtained nanowires' cross-sections (amplitude and phase) corresponding to the diffraction patterns shown in parts (a) of the figures, respectively. The reconstructed image of the wire in the center of the sample (fig. 4.6(c)) shows a regular hexagon of equal side facets with a width of around 500 nm between opposite sides and an almost homogeneous electron density within the hexagon. On the other hand in the second reconstruction corresponding to a NW at the edge of the array (fig. 4.7(c)), the reconstructed object has the shape of an elongated hexagon along one direction, exhibiting a width of about 480 nm between the two opposite facets along this direction, while the width between two opposite facets along the other two directions is about 400 nm and 380 nm, respectively. The electron density within this NW is not homogeneous, showing a bump in the center. Missing data in both diffraction patterns, arising from the much stronger Bragg reflection and from the substrate CTR, have been replaced by their corresponding center-symmetric points prior to the phase retrieval process. This effectively replaces all missing

---

[11] The implementation of the GS-algorithm applied for the reconstruction was written by A. Diaz, compare also [32, 30].

data in figure 4.6(a). However, this can not be applied for all missing points in the case of figure 4.7(a), where some data are missing for both center-symmetric pixel positions. Such missing data could explain the non-homogeneous electron density obtained in 4.7(c), as was also reported by Diaz et al. in the reconstruction of the diffraction pattern from a single InAs NW[32]. The reconstructed phases show small phase changes up to about $\delta\phi = 0.5$ radians. In principle, one could attribute these changes to atomic field displacements along the z-direction up to about $\delta\phi/q \approx 0.025$ nm. However, such small phase variations have previously been obtained in systems in which they were not expected, and they might be due to a non perfect data quality [32]. Given the parabolic structure of the phase within the nanowires' cross-section, one might naively think that it results from the wavefront of the incoming focused beam. Indeed, the incoming beam could very well exhibit a similar curved profile at the focal plane. However, we note that, due to the Bragg geometry of the experiment, the focal plane is tilted by an angle of $90° - \theta_B = 76.35°$ with respect to the xy-plane of the nanowires' cross-section. Therefore, such a phase structure cannot be explained by the incoming wavefront at the sample position, but is rather due to artifacts in the experimental data.

The results obtained by phase retrieval are in very good agreement in terms of shape and size with those obtained above for the Fourier transform analysis. In addition, they show the realistic spatial resolution due to the extension in reciprocal space of the measured diffraction patterns. In the vertical direction (y), the real-space resolution is about 15 nm limited by the measured dynamic range in intensity. In the horizontal (x) direction a resolution of about 50 nm is obtained, limited by the range of the rocking scan around the Bragg reflection.

4.4 Microstructure of GaAs nanowires

Based on the diffraction experiments, the NWs are found to exhibit a smaller in-plane lattice parameter, but a larger lattice parameter along the growth direction compared to the bulk ZB phase. As discussed in section 2.3, the observed change in lattice parameter in the SA-MOVPE grown GaAs nanowires can be understood if we assume that a high density of stacking-faults or rotation twins is present in the NWs, changing the *hexagonality* of the crystal structure.

As we have seen above (section 3.3), the $(3\,5\,1)^c{=}(1\,1\,\overline{2}\,9)^h$ reflection is not affected by stacking faults. Compared to that, the $(1\ 0\ \overline{1}\ \mathrm{L})^h$ direction in the surface coordinate system will be affected by the presence of stacking faults and can be accessed in the coplanar experimental geometry. Therefore, additional measurements have been performed on the NWs inspected before. Here, the intensity distribution between the cubic $(331)^c$ and $(422)^c$ Bragg reflections was measured, corresponding to a range between the $(1\,0\,\overline{1}\,7)^h$ and $(1\,0\,\overline{1}\,8)^h$ reflections in the surface coordinate system. Reciprocal space maps of the measurements are shown in figure 4.9. Fig. 4.9(a) shows the intensity distribution around the $(4\,2\,2)^c{=}(1\,0\,\overline{1}\,8)^h$ reflection of the substrate. Clearly visible is the crystal truncation rod of the substrate, extending along the q_z direction perpendicular to the surface. Besides this CTR of the substrate, a second streak is observed, displaced by $\Delta q_x/q_x \approx 1 \cdot 10^{-3}$ from the substrate position (dashed lines). This displacement is the same as observed around the $(3\,5\,1)^c$ reflection discussed above. Fig. 4.9(b) shows a larger scale view of the measured region in reciprocal space. Compared to the cubic $(3\,5\,1)^c$ reflection, no distinct Bragg peak attributed to the NWs is observed here. Instead, we find a very homogeneous intensity distribution, extending over the entire range in q_z.

After focussing the x-ray beam using the FZP and selecting the coherent volume only, parts of the same region in reciprocal space have been recorded for different individual NWs. Figures 4.9(c) and (d) show the measured diffraction patterns for two different NWs investigated. As visible, the homogeneous intensity distribution splits up in many *speckles*. Due to the coherent illumination, this is expected and was exemplarily analyzed by Favre-Nicolin et al. using a Monte-Carlo simulation in order to retrieve the detailed arrangement of stacking-faults for a selected NW [43]. A detailed analysis of this diffraction patterns is beyond the scope of this work, but the measurement indeed indicates the presence of many stacking faults. For a quantitative estimate of the defect density, we can compare the measured intensity distributions in reciprocal space

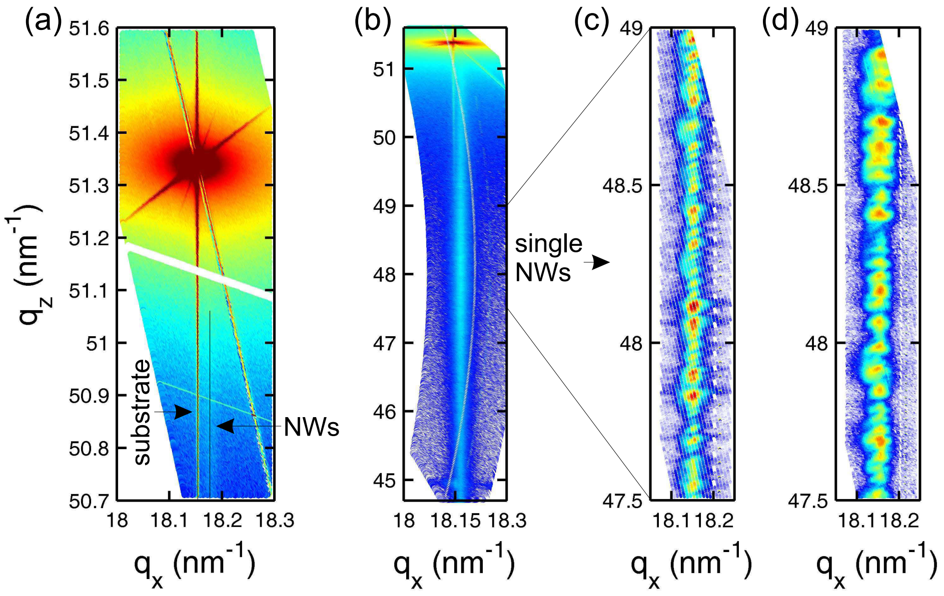

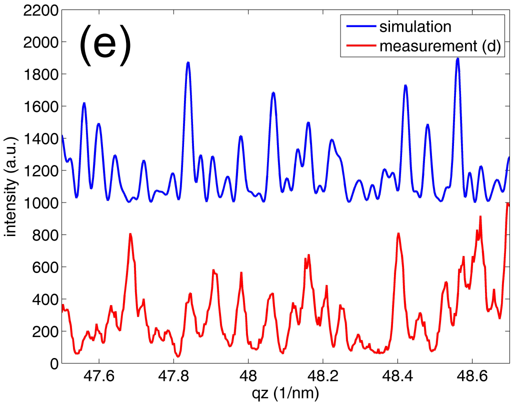

Figure 4.9: (a) Intensity around the GaAs $(422)^c$ reflection. The ensemble of NWs diffracts not only a single Bragg peak, but cause a streak displaced horizontally. (b) shows a larger scale image of the NW-streak, extending between the $(422)^c$ and $(331)^c$ reflections. (c) and (d) show exemplarily measurements at two different single NWs. Qualitatively, (e) compares the measurement with a simulation of random stacking-faults with 3 ML average distance.

with a simulation of the diffracted intensity of a NW containing rotation twins at random positions. For example, fig. 4.9(e) shows a line profile of the intensity distribution in fig. 4.9(d) together with a simulation using equation (3.23) of a Poisson-distributed arrangement of twin-planes with mean distance of 3 MLs in a 280 nm high NW, showing qualitative similarities in terms of speckle-separation, visibility and width.

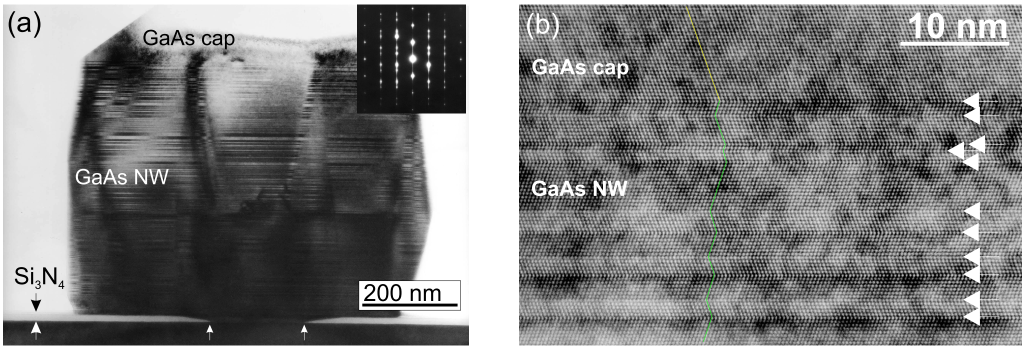

Figure 4.10: (a) Bright-field TEM image of a GaAs NW (diameter $\approx 300nm$) that was overgrown by a GaAs cap layer. Whereas lateral overgrowth adapts the defect structure of the initial NW, axial overgrowth leads to a defect-fee 'cap' in the ZB structure. The inset shows a selected area electron diffraction pattern, showing a twinned ZB structure (from [103]). (b) High-resolution TEM image of the topmost region of a NW similar to the one in (a). Visible is a random arrangement of ZB-twins. The average distance between twin-planes is estimated to be 6 MLs. The twin-structure is also visible in (a) by the dark-light contrast, showing a shorter distance between the twin-defects at the bottom of the NW compared to the top.

On selected samples obtained by the same growth scheme, transmission electron microscopy measurements have been performed. Figure 4.10(a) shows a bright-field TEM image of one of the inspected NWs. Several features are visible in this image. First, the Si_3N_4 mask is visible on top of the GaAs substrate. In the center of the NW, the mask-opening created in the lithography process is observed. The diameter of the hole amounts to 200 nm and the sidewalls are tapered due to the etching procedure. As visible, the NW has overgrown the Si_3N_4 layer. In the GaAs NW itself, a high number of twin defects can be observed, visible by the light/dark contrast. The samples used for the TEM inspection have been overgrown by a very thin InAs quantum well and an additional GaAs shell layer after the main nanowire growth. Whereas the InAs quantum well can not be observed in the TEM image [103], the GaAs shell leads to a formation of a nearly defect-free GaAs 'cap' visible in the top region of the figure. In lateral direction, the stacking faults are transferred from the core into the shell region. The inset in fig. 4.10(a) shows an selected area electron diffraction pattern taken in the top region of the NW. The picture displays the typical diffraction pattern of a twinned zinc-blende lattice, with sets of two spots aligned along vertical 'rods' on the left and right side of the center. Note that the central rod as well as the third rods left and right hand side the central rod do not show this twinning, because they are insensitive to the presence of stacking-faults (compare the case of x-ray diffraction from stacking-faults). Figure 4.10(b) shows a magnified high-resolution TEM image obtained at the border between the cap-layer and the initial NW [104]. The defect free cap and the NW region are indicated, together with arrows indicating the position of twin-defects, occurring in distances between 0.6 nm and 4.5 nm. The mean distance between subsequent twin-planes amounts to 1.992 nm, which is equivalent to 6.1 (111)-layers. Although no high-resolution images for the structure of the lower part of the NW are available, a close inspection of fig. 4.10(a) shows, for this example, a higher density of twin defects in the lower 300 nm of the NW compared to the top region. As the NWs inspected by x-ray measurements have an average height of 400 nm, we may assume that also in this case the average separation of stacking faults is 6 MLs or less, in agreement with the very rough estimation of 3 MLs separation from the XRD-measurements. In terms of *hexagonality*, the observed average distance between twin-defects corresponds to a hexagonality of $1/6\approx$ 17% - $1/3\approx$ 33%. As we will see, this is consistent with the observed change in lattice parameter, as shown in chapter 5.

4.5 Discussion

Compared to SEM, the x-ray methods applied here provide not only the shape of the NWs, but at the same time crystallographic information like the lattice parameters can be obtained destruction free and with high resolution. In the present case we could show that NW parameters such as height, diameter, lattice parameters and misorientation change among NWs located at different positions within in the predetermined NW array. This differences can be attributed to the fluctuations of local shape of the etched openings in the SiN_x mask and by the growth parameters, fluctuating among different positions on the sample. Whereas variations in the shape can also be detected by SEM inspections (compare fig. 4.1), the combined determination of shape and lattice parameters with high resolution is hardly possible by complementary destruction free methods.

Besides local fluctuations, we have observed that the mean lattice parameters of the NWs differs significantly from bulk GaAs. The x-ray measure-

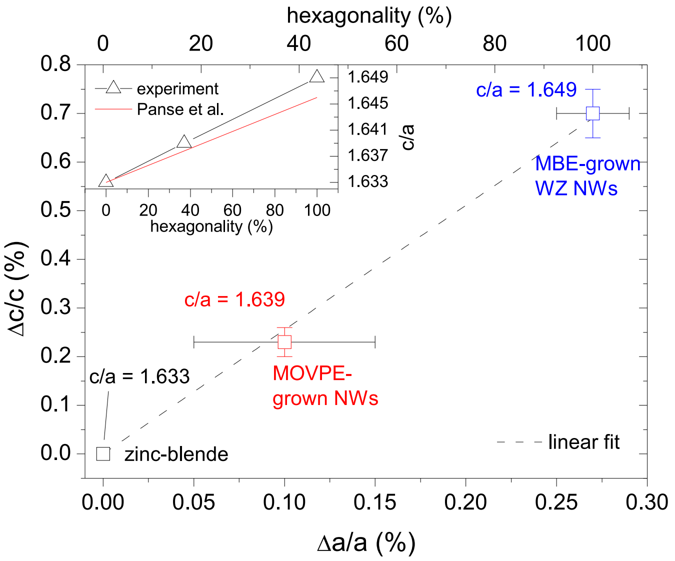

Figure 4.11: Relative increase in the vertical lattice plane spacing $\Delta c/c$ against the relative decrease in the hexagonal in-plane lattice parameter $\Delta a/a$. By definition, the cubic ZB structure marks the origin of the coordinate system. Datapoints for the MOVPE grown NWs (this chapter) and MBE grown NWs with WZ structure (next chapter) are shown. The inset compares the experimentally observed c/a ratios as function of the *hexagonality* with theoretical predictions by Panse et al. [106].

ments showed an average *decrease* of the in-plane lattice parameter by $\Delta a/a = -(0.1 \pm 0.05)\%$ and an average *increase* of $\Delta c/c = (0.23 \pm 0.03)\%$ of the lattice plane spacing along the growth direction. Figure 4.11 summarizes these findings and puts them in a context with measurements of the wurtzite lattice parameter in GaAs NWs grown by MBE that will be obtained in the next chapter. If we assume a linear increase of the c/a ratio as function of hexagonality, the present results are consistent with a hexagonality of $\approx 36\%$, corresponding to an average distance of 2.8 MLs between subsequent twin-planes. This appears in reasonable agreement with the indications of TEM measurements and coherent diffraction measurements discussed in the previous section.

5 Structural evolution and relaxation of GaAS NWs on Si grown by MBE

In this chapter, we study the structure and lattice parameter accommodation in the initial stage of GaAs nanowires grown on Si (1 1 1) using the Ga-assisted growth mode in molecular beam epitaxy (MBE). In sections 5.1, general aspects regarding the growth of GaAs on Si and in particular the growth of NWs on a mismatched substrate are briefly discussed. In section 5.2, details about the growth parameter of the studied NWs are given together with their morphological evolution obtained by electron microscopy. In a first step in section 5.3, x-ray diffraction will be used to determine the structural composition of the NWs as function of growth time. Whereas conventional diffraction measurements allow to determine the averaged composition with good statistics in a fast measurement, nanodiffraction experiments on single NWs are used to probe the statistical occurrence of the different crystallographic phases (5.4) as well as the detailed arrangement of the different structural segments in selected NWs (5.5). Finally, in section 5.6 we observe that the NWs are subject to a residual compressive strain at their bottom interface towards the substrate, originating from a partial relaxation by the inclusion of misfit dislocations at a rough interface. This in-plane strain is further probed by grazing incidence diffraction (5.7) and compared with the relaxation of significantly thinner NWs in section 5.8, whose diameter is below the predicted critical diameters for dislocation free growth [152]. Contrary to theoretical expectations, we find an instantaneous strain release even for thin NWs, showing that besides energetic aspects also the chemistry in the nucleation stage play a crucial role when aiming to achieve defect free interfaces.

5.1 Introduction

As discussed in chapter 2, the control of the crystal structure during NW growth is a major challenge, as changes in crystal structure also affect the electronic properties of the NWs. Thus, many studies have been devoted to elucidating the correlation between crystal structure and growth conditions, both for the Au-assisted and the self-assisted growth modes[34]. However, the NW structure close to the substrate interface is seldom addressed, although strong changes in growth conditions can be expected there. For example, in the case of Ga-assisted NW growth, liquid Ga droplets are formed in the beginning, and growth starts after the oxide layer below the droplet has been resolved. In turn, the droplet is lifted upwards during NW growth, with possible changes in chemical composition or contact angle, which crucially affect the crystal structure. Whereas the structural evolution during growth or at the end of growth can be easily investigated by TEM, e.g. after removal of the NWs from the substrate, characterization of the initial stage is more challenging.

Besides possible structural changes during the initial stage, the contact between NW and substrate may induce strains. From a technological point of view, it is highly desirable to combine the properties of compound semiconductors like GaAs, exhibiting a direct band gap and good optical coupling, with the high-speed Si technology that serves as platform for most electronic applications nowadays. However, the interface between both material should exhibit a low number of extended defects. From planar crystal growth it is known that pseudomorphic growth between materials with large lattice mismatch is limited up to a certain critical layer thickness [90], above which misfit dislocations are induced or island formation may take place (Stranski-Krastanov growth mode) [130]. These islands show a gradual strain release from the bottom towards the free surfaces.

As the lattice parameter of GaAs is 4% larger than that of Si, the direct combination of both materials is challenging and many attempts have been made to integrate GaAs films on Si-substrates [12]. In molecular beam epitaxy (MBE), direct growth of GaAs on Si typically starts as island-growth (Volmer-Weber growth mode). These islands may coalesce and form a closed film. However, the large lattice mismatch between both materials induces a large number of threading dislocations at the film-to-substrate interface, making the system inadequate for device production.

Compared to that, it is believed that epitaxial growth of nanowires on lattice-mismatched substrates can be realized without the introduction of misfit dislocations up to a critical diameter, depending on the respective lattice mismatch [50, 39, 151, 152]. Understanding the process of lattice parameter accommodation is essential in order to control both axial NW-heterostructures as well as the interface towards the underlying substrate. However, whereas the growth and relaxation of axial NW heterostructures has been addressed by different authors [68], literature about strain accommodation at the NW-substrate interface is rare. Cirlin et al. deduced the critical diameters for dislocation-free growth for different NW-substrate combinations by measuring with scanning electron microscopy up to which diameter nanowires grow straight [23]. For GaAs NWs grown on Si (1 1 1) by molecular beam epitaxy they observed a critical diameter of 110 nm above which NWs grow kinked or do not grow at all, in agreement with a theoretical model by Zhang et al. [152]. For the same material combination and growth technique, a nucleation study revealed that vertical NWs grow only after the initial formation of GaAs islands that accommodate the lattice mismatch, and the NWs are thus strain-free [14, 28]. In the case of GaAs NW growth on Si (1 1 1) by selective area metal-organic vapor phase epitaxy, Tomioka et al. demonstrated by high-resolution transmission electron microscopy the possibility of pseudomorphic growth without the introduction of misfit dislocations for diameters below 20 nm [136], whereas for diameters above 100 nm straight NWs with dislocations were observed [139]. However, the borderline between pseudomorphic and dislocated growth has not been determined precisely.

5.2 Ga-assisted NW growth

The GaAs nanowires under investigation have been prepared and analyzed in SEM by Steffen Breuer in the Paul-Drude-Institut für Festkörperelektronik in Berlin, Germany. NWs were grown by MBE on 2-inch n-Si(111) ± 0.5° substrates, which were covered by their native oxide. At the growth temperature of 580 °C, the simultaneous opening of the Ga and the As_4 source led to Ga droplet formation and subsequent Ga-assisted GaAs nanowire growth. The effective atomic fluxes of both sources were set to be equal (stoichiometric supply) and matched a planar GaAs(001) growth rate of 100 nm/h. The growth was terminated by the simultaneous closing of both sources followed by a rapid cooldown to room temperature [16].

In order to follow the structural evolution during growth *ex-situ*, the nanowire growth time t_g was varied in order to study nanowires with different lengths. Furthermore, it was found that the thickness and number density of the nanowires depend on the specifics of the employed substrate. Nanowires with diameters of about 100 nm and average number density of less than 1 NW/μm^2 were found for growths on highly arsenic-doped Si substrates from *Silchem* with a resistivity in the low mΩcm range. This low density of NWs will be used to perform x-ray diffraction experiments on single NWs later on. In addition, nanowires with significantly smaller diameters (below 50 nm) but higher number density have been prepared on lowly arsenic-doped substrates. This will be discussed in section 5.8.

Figure 5.1 shows SEM images of the inspected samples, which will further on be denoted by capital letters (A-C). For each sample, nanowire lengths and diameters were measured and are summarized in table 5.1. For sample B, which showed an unusually wide nanowire size distribution across the wafer, two small pieces were analyzed. Due to inhomogeneity of the growth temperature across the substrate, the Ga formed droplets with lower average diameter towards the wafer edges, resulting in longer NWs.[127] One piece was taken from the center of the wafer (B1) and another one approximately 1 cm away from the wafer edge. The NWs on samples (A-C) are grown with diameters between 90 nm and 300 nm. The length is increasing from ≈ 20 nm (A) over 40 nm (B1) and 100 nm (B2), until for sample (C) NWs with 1.21 μm length are obtained. Although NWs grow well separated, island-like structures are observed between them for long growth times, as was reported before[24].

Table 5.1: Overview of growth-time (t_g), length (L) and diameter (D) of the inspected NWs in series (A-C). The average as well as the standard deviation obtained from measurements of at least five nanowires are shown.

Sample	A	B1	B2	C
t_g / s	60	300	300	3600
L / nm	18±10	44±13	100±46	1208±21
D / nm	121±6	285±65	138±14	91±8

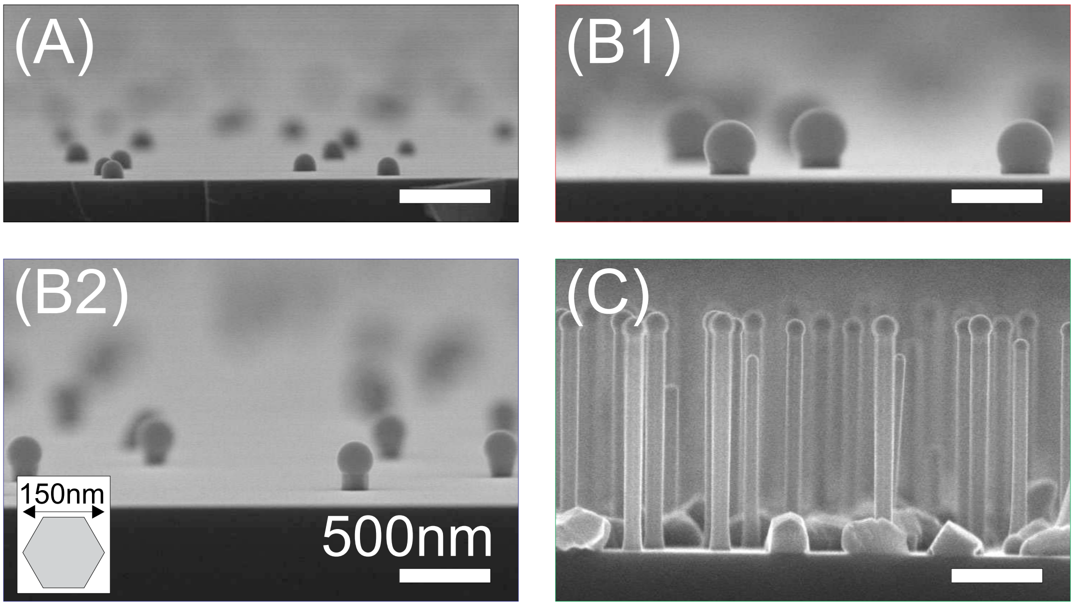

Figure 5.1: SEM pictures of the inspected GaAs nanowires in series (A-C). The diameter of the NWs ranges between 100 nm and 140 nm (A,B2,C) up to 280 nm (B1). The length of the NWs is increasing from 15nm (A) to 1.2μm. For short growth times, the NWs are well isolated on a smooth surface. For long growth times, small island-like structures are visible between the wires. All scale-bars 500 nm.

5.3 Evolution of average structural composition

(published in paper [II])

The average structural composition of the NWs was determined ex-situ by asymmetric x-ray diffraction measurements at the ID01 beamline at the ESRF synchrotron source (section 3.4). The sample was illuminated with an 8 keV x-ray beam with a size of 200×200 μm^2. Using a 2-dimensional MAXIPIX pixel detector, the diffracted intensity along the $(1\,0\,\bar{1}\,\mathrm{L})^h$ direction was measured, containing the cubic $(3\,3\,1)^c$ and $(4\,2\,2)^c$ type of reflections of the two possible ZB twin orientations, as well as the $(1\,0\,\bar{1}\,5)^{wz}$ reflection (cf. right part of fig. 5.2 and section 3.4). The data was integrated along q$_x$ and q$_y$ in order to obtain the integrated intensity of the Bragg reflections as function of q_z.

Figure 5.2(a) shows the measured intensity distributions along the q_z direction after subtraction of the contribution of diffuse scattering of the Si $(422)^c$ reflection, located in close vicinity to the GaAs $(422)^c$ reflection in reciprocal space ($|\mathbf{q}|_{Si}^{(422)} = 56.68\mathrm{nm}^{-1}$ and $|\mathbf{q}|_{GaAs}^{(422)} = 54.45\mathrm{nm}^{-1}$). Independent of NW length, all samples show both the ZB as well as the WZ reflections, but differ in the relative intensities. The dashed line in fig. 5.2(a) indicates the calculated position of the corresponding WZ reflection based on the cubic lattice constant of the ZB phases and the c/a ratio of a perfect ZB structure (1.633). Clearly, the measured peak position of all the WZ reflections is shifted towards smaller q_z, corresponding to a larger c lattice plane spacing in the WZ structure. However, no significant change in the in-plane peak position between the ZB and WZ type reflections could be observed within the experimental resolution ($\Delta q/q \approx 1 \cdot 10^{-3}$), as has been observed for phase pure ZB and WZ InAs nanowires by Kriegner et al. [74]. Later on, diffraction experiments in a grazing incidence diffraction geometry will be used to reveal also a change in the in-plane lattice parameter between WZ and ZB structures. From the displacement of the WZ reflection from the ideal position, we obtain a relative increase of $\Delta c/c = (0.7 \pm 0.05)\%$ of the lattice parameter of the WZ structure compared to the geometrical consideration.

The second important observation from the XRD measurements is that the intensity ratio between WZ and ZB reflections changes as a function of NW length. After normalization by the respective structure factors of the measured Bragg reflections (compare Appendix A), the total volume present in the different structural phases can be estimated from the intensity ratios of the integrated intensities [145]. The quantitative analysis of this trend is shown in figure 5.2(b), showing the total volume fraction of WZ units present in the sample (open circles) and the relative WZ content that has been grown in the additional length segment compared to the previous, shorter sample (triangles)[12]. Whereas for the shortest NWs (A) both ZB and WZ phases occur in roughly equal abundance (≈ 60 % ZB and 40 % WZ), only ≈ 3 % of WZ are incorporated between 100 nm and 1200 nm (last triangle). The last datapoint was corrected for the presence of island-like structures between the wires, assuming them to be of ZB structure and containing a total volume fraction of 50 % (estimated from SEM images).

---

[12] Compared to the data presented in paper [II], the nanowire length on the x-axis of the plot has been corrected by a more detailed length evaluation by SEM summarized in table 5.1, resulting in slightly larger NW lengths for sample (B1) and (B2) compared to the values in [II].

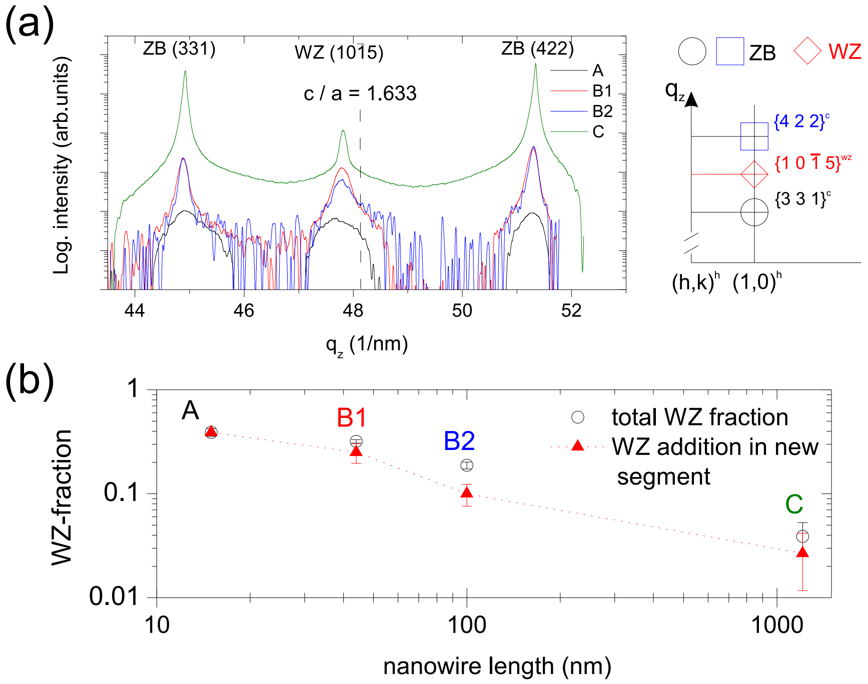

Figure 5.2: (a) Ensemble averaged intensity distributions of the ZB $(331)^c/(422)^c$ and WZ $(10\bar{1}5)^{WZ}$ reflections. Compared to the ZB segments, the lattice parameter along the growth direction is increased in the WZ phase. The right inset shows a sketch of the peak positions in reciprocal space. (b) Evolution of the WZ content as function of the average NW length measured by SEM. Triangles: WZ content in the newly grown NW segment.

In other investigations of self-assisted GaAs NWs it was found that the crystal phase changes from ZB to WZ as growth proceeds [75, 109, 22]. However, in those studies dispersed NWs were characterized by transmission electron microscopy, and thus in contrast to our measurements the very base of the NWs was likely not taken into consideration. Also, Krogstrup et al. demonstrated that the transition from ZB to WZ can be avoided, leading to the growth of pure ZB NWs.[75] At the same time, these authors observed a high density of twin planes at the bottom of those NWs. Our XRD measurements average over a large ensemble of NWs and proof that the WZ phase forms in significant abundance during the initial growth stage. Moreover, the experimental data provides the quantitative dependence of the WZ content on NW length.

5.4 Statistical distribution of zinc-blende twins and wurtzite segments

Whereas the x-ray measurements presented above allow to study the average structural composition of a large ensemble of NWs, no information about the phase composition within single NWs can be obtained. In section 5.5, we will use diffraction measurements on single NWs in order to retrieve the arrangement of ZB and WZ structural units within single selected NWs. However, these measurements have been restricted to a small amount of NWs only, due to experimental limitations discussed below. In this section, we use a recently developed experimental setup at the ID01 beamline in order to probe the structural composition of a large amount of NWs and obtain their statistical distributions.

Until recently, a major restriction to the measurement of single nanoobjects was the reliable identification and discrimination of different objects below the x-ray beam. In the conventional scheme for object identification at the ID01 beamline, the positioning stage was stopped at each (x,y) coordinate and the detector was integrating the intensity for a desired time. Additional time of 2.5 s was required for the electronic readout and storage of the signal in the detector system. This rather time consuming procedure usually allowed to identify and measure a limited number of NWs only.

Meanwhile, a recently developed electronics allows for the integration of the diffraction signal recorded by the 2dimensional MAXIPIX detector during a continuous, synchronized movement of the sample-positioning system, leading to a drastic decrease of the time required to obtain spatially resolved intensity maps of a desired Bragg reflection. With the new electronics, the time required to obtain a single map reduces by $\approx$ 2 orders of magnitude, allowing to scan much larger surface areas than possible before. We have used this new system in order to determine the individual structural composition of a large number of NWs. To this end, we determined the spatial distribution of GaAs NWs on the sample at the symmetric $(111)^c = (0003)^h$ reflection, allowed for both ZB and WZ crystal structures. The phase composition of the same NWs was monitored at two ZB and one WZ sensitive reflection, i.e. the $(331)^c$, $(422)^c$ and $(10\bar{1}5)^h$ reflections, respectively[13]. For a fixed azimuthal orientation of the sample (along

---

[13] In the diffraction experiments presented in all other sections, the conventional scanning scheme was used and prevented to measure different Bragg reflections of the same nanowires.

the $(331)^c$ reflection of the substrate), the two cubic reflections measure the diffracted intensity from *non-twinned* or *twinned* domains of the ZB lattice with respect of the substrate lattice, respectively (cf. section 3.3). Exemplarily, the measurements presented here have been performed on sample (B2), providing 100 nm long NWs with sufficient separation to probe them individually.

Figure 5.3 (a) shows the intensity distribution of the $(111)^c$ reflection on a surface area of 35 μm x 50 μm. In this example, the integration time of each point in the x-y map could be reduced to 0.02 s, where the translation speed of the piezo system was chosen in a way that this corresponds to a translation of the sample by 250 nm. Visible are well defined spots attributed to single NWs, all exhibiting a similar size caused by the convolution of the NW diameter of $\approx$ 100 nm with the footprint of the x-ray beam, illuminating the sample under an angle of 13.7° with respect to the sample surface. Occasionally, several spots overlap if the distance between subsequent NWs is smaller than the width of the x-ray beam.

In figure 5.3(b), this intensity distribution is superimposed by contour plots of the intensity distributions of the $(331)^c$ (black), $(422)^c$ (red) and $(10\bar{1}5)^{WZ}$ (green) reflections, visualizing the two ZB orientations and the hexagonal wurtzite phase, respectively. All NWs visible in the symmetric reflection are present in one or more of these structural sensitive reflections as well. Unavoidably, the involved sample rotation between the different Bragg reflections causes small offsets (in the order of a few μm) in the entire spatial position of the maps, which have been corrected by recognition of characteristic arrangements of NWs. Although this allows the identification of single objects in different reflections, small discrepancies between the different positions remain, most likely caused by small drifts of the experimental setup. For a statistical analysis of the measured intensity distributions, the intensities of each NW have been integrated. To this end, elliptical integration areas of about 1x2 μm^2 have been defined around each NW obtained in the symmetric picture, taking into account the footprint of the x-ray beam. For NWs situated close to each other, a reduced size of the integration area was chosen, determined from the distance between adjacent NWs. For the maps recorded in the asymmetric reflection geometry, an iterative refinement step of the center of the integration area was performed, shifting the center of the integration area to the maximum of the intensity in the prior defined area if the maximum intensity was higher than 1.5 times the average background. This procedure allowed to efficiently correct for the spatial offset between the NW positions at different reflections.

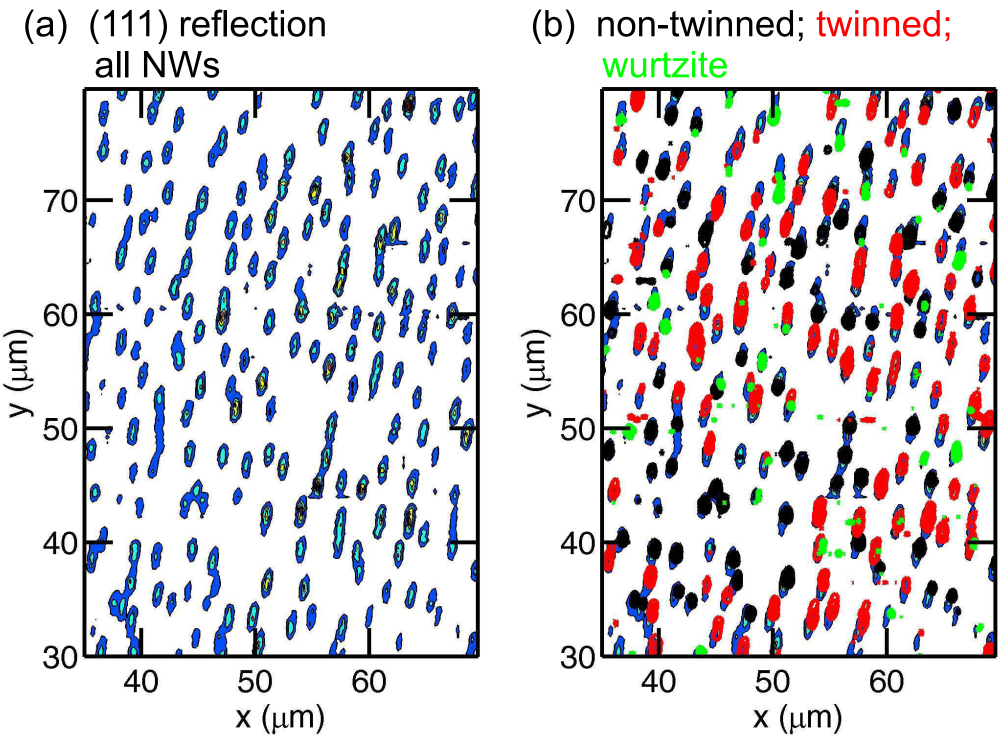

Figure 5.3: (a) Intensity map of the $(1\,1\,1)^c$ reflection, representing all NWs on the sample. (b) Overlay of (a) with the intensity distributions of the, compared to the substrate, non-twinned (black), twinned (red) and wurtzite (green) orientations.

For both ZB and the WZ reflections, the spatially integrated intensities were determined and normalized by the respective structure factors, taking into account that, for example, the cubic $(422)^c$ reflection will be more intense compared to the $(331)^c$ reflections for structures of same size. This correction allows for a quantitative comparison of the crystal phases in the NWs. Note that by this estimate not the total integrated intensity of the x-ray rocking-curve is considered for each NW, because the intensity is recorded for a fixed incidence angle of the x-ray beam as determined from the Bragg peaks maximum from the ensemble of NWs. Instead, due to the 2dimensional detector, the data represents an integrated slice through the NWs intensity distribution in reciprocal space. Using this approach, we observe that in total, the non-twinned $(331)^c$ orientation shows an abundance of 60% of all ZB signals, whereas the twinned

$(422)^c$ orientation amounts to 40% only. Hence, our observation indicates that the majority of the NWs ZB material is non-twinned compared to the underlying substrate lattice. In average, 25% of the NWs volume are found in the WZ phase. These average values are in well agreement with ensemble-measurements using an x-ray beam of 200 μm diameter, demonstrating the feasibility of the used approach. However, compared to measurements using a broad x-ray beam we are now able to quantify the distribution of the different crystal orientations among the different NWs.

For a more quantitative comparison, for each of the 160 inspected NWs the phase fraction of the total diffraction signal (corrected by the respective structure factor) was determined and binned in steps of 10%. Figure 5.4 displays the histograms for the non-twinned (a), twinned (b) and WZ phase (c) for all inspected NWs. In this representation, the y-scale measures the percentage of NWs exhibiting the given phase fraction shown along the x-axis. The inset in fig. 5.4(c) depicts a scheme of the NW structure as obtained from TEM images (cf. section 5.5). Here, frequently non-twinned ZB segments are observed at the bottom the NW, but WZ segments and twinned ZB segments are observed as well. Fig. 5.4(a) shows the histogram of the non-twinned orientation. Whereas few NWs contain only a small amount of non-twinned material, a significant fraction of NWs contain non-twinned material in more than 50% of the total NW volume. Compared to that, in more than 50% of all inspected NWs the twinned ZB segment (fig 5.4(b)) has a length between only 0% and 20% of the total NW length, whereas higher occupancies are found in less than 10% of the NWs only and no distinct occurrence of larger segments is observed. For an average NW length of 100 nm, this amounts to a majority with total segment-length of only up to 20 nm. For the WZ phase, most NWs contain between 0% and 50% of WZ, with an average of 25%.

As we know the intensity of both ZB orientations in each single NW, we can also calculate the fraction of twinned ZB material within the total ZB part of each NW. If the entire ZB part in the NW has the orientation of the substrate lattice, this ratio is 0, whereas it amounts to 1 for a completely twinned ZB part. This histogram is shown in fig. 5.4(d). As we see, the configuration of equal occurrence of both ZB phases ('50-50') is present in less than 10% of all NWs and the majority of all NWs is grown in the non-twinned phase. This supports the indicated structure observed in TEM images, showing that the extended ZB segments are almost free of twin defects. If we assume that NW growth commonly starts in the non-twinned orientation imposed by the substrate, the

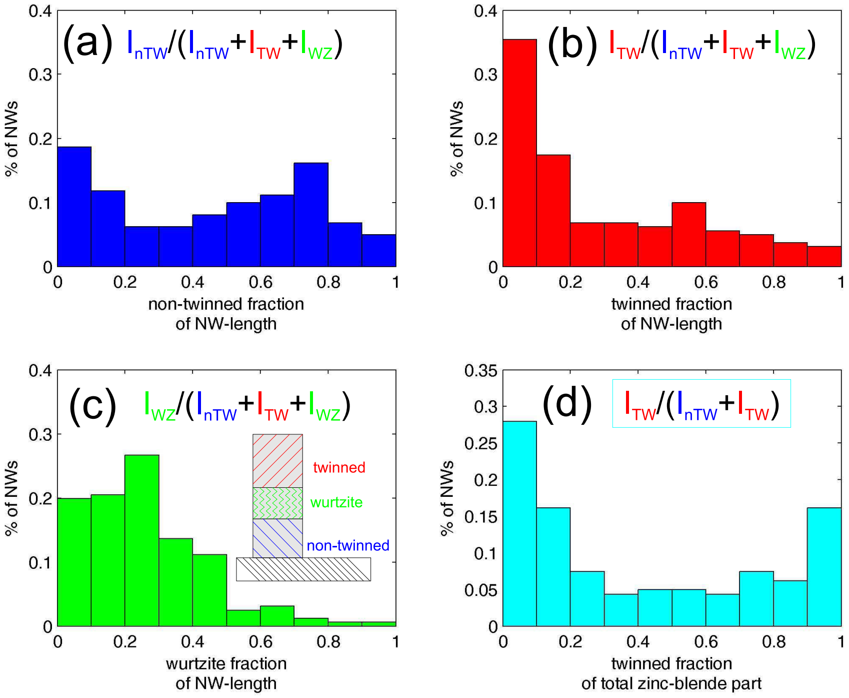

Figure 5.4: Histograms showing the percentage of NWs (y) in which the respective phase (non-twinned (a), twinned (b), wurtzite (c)) is present in a certain fraction (x). (d) shows a histogram of the twinned fraction of the ZB part only. The inset in (c) displays a schematic representation of the different structures compared to the substrate. Formulas indicate how the histograms are obtained.

general dominance of the non-twinned orientation can be understood. If growth proceeds in the hexagonal WZ phase and switches back to the ZB phase after a segment of random length, we do not expect a predominant orientation of the following ZB phase. However, together with the initial ZB segment at the bottom of the NWs, the non-twinned orientation will dominate.

In summary, the presented experimental technique allows to scan much larger surface areas in a significantly reduced amount of time compared to conventional scanning x-ray diffraction. This allows to reliably locate the same objects even at different Bragg reflections and significantly reduces the time required for diffraction experiments on single nanoobjects. In the grown GaAs NWs, we observed that in less than 10% of all NWs, the two ZB orientations occur in equal abundance, i.e. the majority of the NWs is composed by only one ZB phase. Moreover, imposed by the substrate the non-twinned orientation is the dominant one in most of the NWs. Whereas the majority of the NWs contain twinned segments of extension less than 20% of the total NW length, a significantly larger number of all NWs has extended segments in the non-twinned orientation.

5.5 Distribution of ZB and WZ phased along the growth direction

(published in paper [III])

In the previous sections, we have seen that the wurtzite crystal structure forms in large abundance during the initial stage of NW growth. Based on the results in section 5.4, we observed that WZ and ZB parts mix randomly in different NWs. However, the detailed structural composition along the growth axis can not be determined from these measurements, and it can only partially be judged whether the observed WZ material is present in the form of single extended segments, or many smaller parts throughout the NW. In order to probe the phase composition, and in particular the WZ content and position along the growth axis, diffraction profiles of the symmetric $(111)^c$ reflection of single NWs have been measured and analyzed, using the fact that the WZ segments exhibit a larger vertical lattice parameter than the ZB segments.

The diffraction experiments have been performed on sample (B2) described above. Besides the well suited average distance between the NWs, the dimensions of the NWs fit well to the experimental condition for the diffraction experiments (see below), providing a sufficient number of well resolved size oscillations in reciprocal space and reasonable scattered intensity in order to perform measurements on a single nanowire in the time-scale of minutes. The experiments in a coplanar performed at the ID01 beamline at the ESRF using the setup described in section 3.4. At the photon energy of 8 keV, a measured focal size of 300 x 300 nm^2 has been obtained.

The left panel in figure 5.5 shows an ensemble averaged (i.e. 200 x 200 μm^2 sized x-ray beam) reciprocal space map of the sample, measured around the $(111)^c$ reciprocal lattice point, allowed for both ZB and WZ structures. The strong reflection shown in the upper part corresponds to the silicon $(111)^c$ re-

Figure 5.5: Reciprocal space maps around the GaAs $(111)^c$ reflection. left: Ensemble measurement, showing the Si and GaAs $(111)^c$ reflections. right: measurements on single NWs with a focussed x-ray beam. NW lattice parameters fluctuate around the average values. If no NW is illuminated (vi), only a small signal is observed, caused by the long tails of the focussed x-ray beam still illuminating wires. Colorscale: log(intensity). Average and single measurements are on different scale due to focussing.

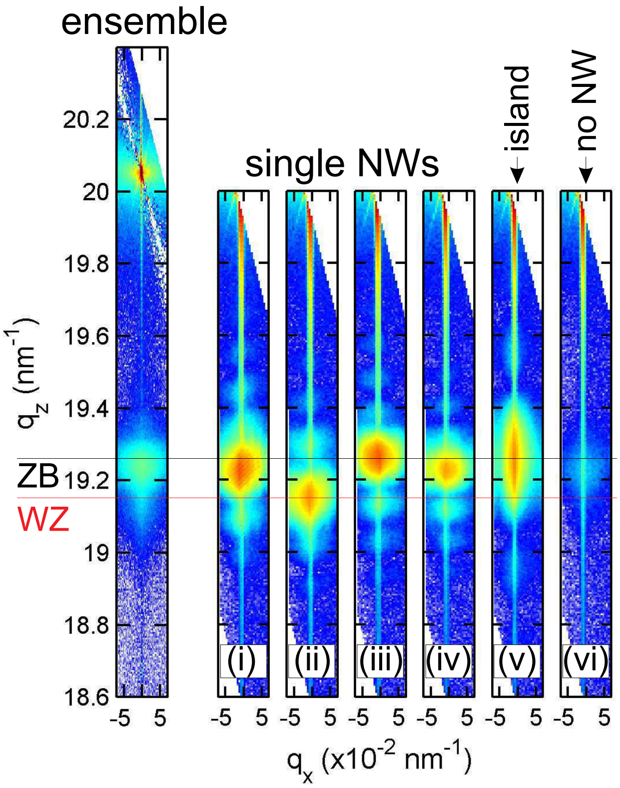

flection and is used as a reference signal in all measurements. Due to the larger lattice parameters of WZ and ZB GaAs, the Bragg peak of the NWs is located at smaller vertical momentum transfer and ZB and WZ segments diffract at different values of q_z, reflected by the superposition of two peaks. Dashed vertical lines indicate the expected peak positions of the ZB and WZ structures as obtained from the 0.7% increased lattice plane spacing of the WZ phase observed in in the asymmetric reflection geometry.

The panels at the right hand side of fig. 5.5 show the same region in reciprocal space, measured at different individual NWs using the focused x-ray beam. Because of the different lattice parameters of WZ and ZB structures, the varying WZ-content of different wires is reflected by the strong differences in the individual diffraction signals. Compared to the average signal, the finite size of the individually diffracting NW causes thickness oscillations along q_z, inversely proportional to the NW‘s height. Whereas most NWs show a similar height of around 70 nm, measurement (v) indicates a height of about 30 nm only, but a larger lateral size due to the smaller width along the horizontal axis. Most probably this measurement corresponds to an island-type crystallite grown randomly between the NWs.

In order to compare the structure of individual NWs more quantitatively, the intensity distributions along q_z have been extracted from the reciprocal space maps, shown by open symbols in figure 5.6. To identify the structural composition along the vertical axis, the data were modeled assuming that each NW contains a wurtzite segments of length D_{wz} located at a height H_{wz} above the substrate, illustrated by the lower schemes in fig. 5.6. The intensity distribution of this nanowires was simulated using equation (3.23), taking into account a relative increase of 0.7% in the lattice plane spacing along the growth direction for the WZ segments that was determined above. As we will see, this model is sufficient to describe the measured intensity distribution and agrees with structural compositions found in TEM inspections at selected wires, showing that the NW structure is mainly ZB together with extended inclusions of WZ structure close to the substrate (cf. fig. 5.7).

As example, one out of all measured diffraction signals, shown by fig. 5.5 (ii) and fig. 5.6 (ii) shows a significant shift of the central peak towards the WZ position. The extracted data is shown in fig. 5.6 together with a simulation of the diffracted intensity of an (61 ± 1) nm high NW containing around (43 ± 2) nm of wurtzite located at the bottom (compare sketch of the used structures in fig. 5.6 (bottom)). The increase of measured intensity above $q_z = 19.6\text{nm}^{-1}$ is caused by the increasing contribution from the Si-reflection seen in fig. 5.5. This part of the data has not been considered in the simulation, causing the systematic discrepancy between simulation and experiment.

The typical WZ content based on simulations was found to be around 5-16 nm in a 60-80 nm high NW, corresponding to 6-22% WZ content. This is in reasonable agreement with measurements on the ensemble of NWs, showing an average WZ content of $(18 \pm 2)\%$ in the inspected sample. As example, the simulation of dataset (iii) is shown based on a (80 ± 1) nm high NW with a (12 ± 2) nm high WZ segment included at a height of (8 ± 2) nm above the substrate. It is worth to note that the measurement is not only sensitive to the amount of wurtzite in the NW, but also the diffraction signal is strongly modified by its position above the substrate. The second simulation shown together with dataset (iii) is based on a wire with same height and WZ content, but the WZ segment located at a height of 16 nm, showing less agreement

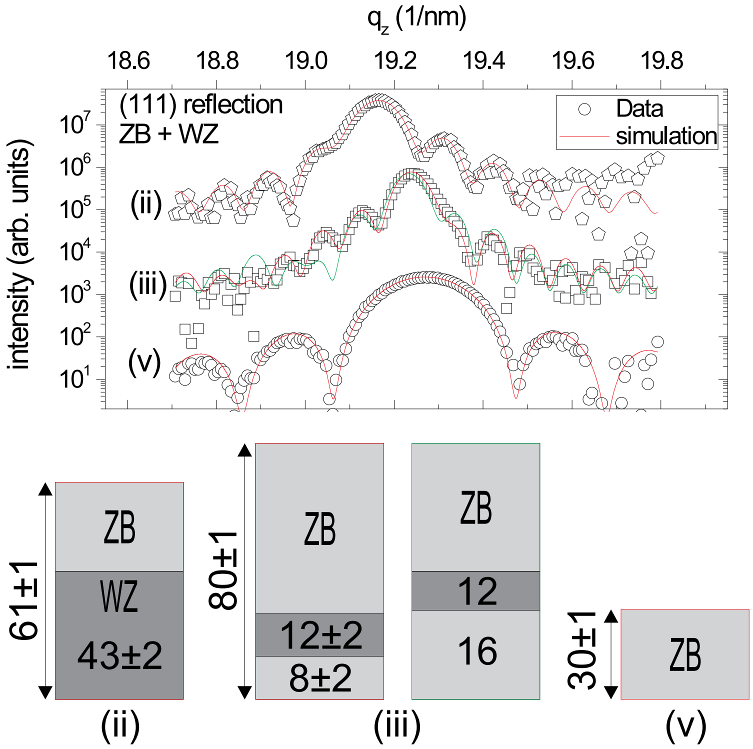

Figure 5.6: (top) Diffracted intensity distribution of single NWs around the GaAs $(111)^c$ reflection. Due to the random mixture of zincblende and wurtzite units, the $(111)^c$ reflection shows strong variations between individual wires. (bottom) Models of the NW structures for simulation of the diffraction patterns (solid lines).Values give the determined vertical dimensions in nm.

with the experiment. Also, all datasets can be sufficiently modeled taking into account only one WZ segment in an otherwise ZB phase nanowire.

A different situation is shown in figure 5.6 (v), showing a measurement from a 30 nm high particle. The data shows no asymmetry along q_z and can be modeled without a WZ contribution and without further displacement field, indicating a strain free particle completely grown in the ZB structure. The corresponding RSM is shown in 5.5 (v). As visible, the width of this reflection along q_x is smaller than at the other NW reflections, measuring a larger lateral size of the particle of around 200 nm along the direction of the incoming x-ray beam. This corresponds well to one of the randomly grown crystallites in between the NWs, that are seen in SEM images after long growth time.

Comparison with TEM

In order to verify the structural composition obtained by the x-ray diffraction analysis, high-resolution transmission electron micrographs have been prepared on single nanowires from sample (B1). The TEM measurements have been performed with a JEM 2010F microscope in the Paul-Drude-Institut für Festkörperelektronik. The microscope operates with 200 kV acceleration voltage achieving a lattice resolution of 0.1 nm. Cross-sectional TEM specimens were prepared in the conventional way through mechanical grinding, polishing and Argon ion beam sputtering. Exemplarily, figure 5.7 shows a TEM micrograph of the interface region of a NW diameter of about 230 nm. The structure of the shown NW is mainly ZB, however, a 17 nm wide region of WZ structure and a region with ZB-twins can be observed close to the substrate, in agreement with the x-ray results above.

5.6 Strain relaxation at the NW - substrate interface of single NWs

(published in paper [III])

Besides the possibility to determine the structural composition using NW resolved diffraction, the strength of XRD is that this technique provides a high accuracy for the determination of lattice parameters and strain. However, in the example above the $(111)^c$ reflection can not be used to obtain precise information about additional small displacement fields in the single structure units, because strong modifications of the diffraction pattern are already induced by the relative lattice mismatch of 0.7% between the WZ and ZB segments and strain and size effects can not be determined uniquely.

In order to disentangle contributions from WZ and ZB structural units, NW-resolved diffraction measurements have been performed at the asymmetric $(331)^c$ and $(10\bar{1}5)^{WZ}$ reflections, which are exclusively sensitive to the ZB and WZ sections in the NWs, respectively. Fig. 5.8 shows three examples of WZ (a) and ZB (b) reflections, measured at different NWs. Due to the large spread of the ZB-signal in reciprocal space, the region around the $(331)^c$ reflection was only partially measured, including the information necessary for further data analysis. It is important to note that the shown Bragg reflections in the top and bottom rows of figure 5.8 have not been measured at the same NWs,

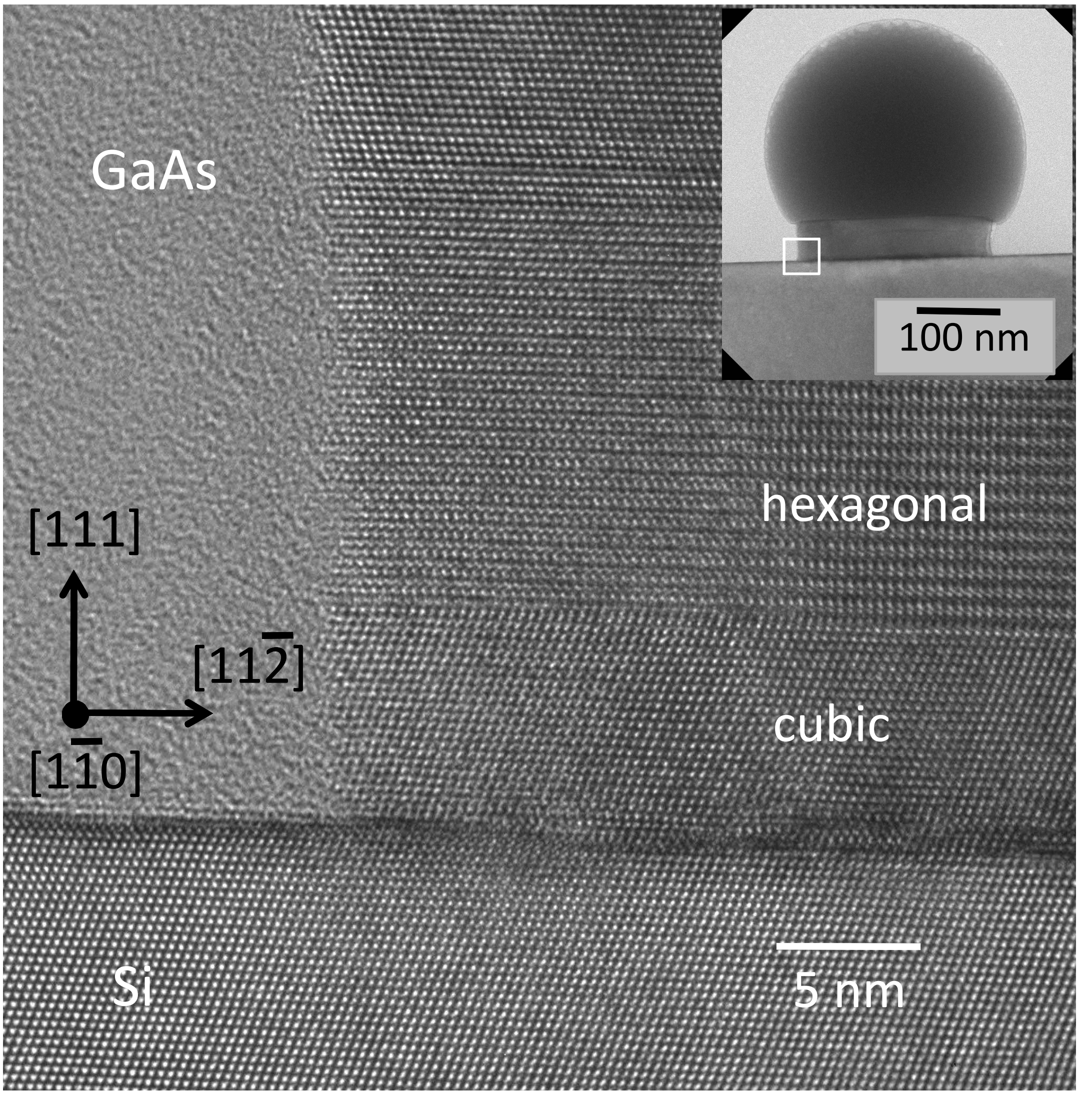

Figure 5.7: High resolution TEM image of a nanowire from sample (B1). NW growth starts in the ZB structure with the same orientation as the underlying substrate. 10 nm above the interface, a 17 nm wide WZ segment is observed, followed by a short segment with ZB-twins before growth continues in the ZB structure.

and the data can not be correlated with the wires measured in the symmetric diffraction geometry above. The measurements presented in this section have been performed before the fast identification of the NW positions presented in section 5.4 became available, and the limited positional stability during the involved sample rotations did not allow to maintain the focal spot of the x-ray beam at the same NW position during the experiments. However, the current developments and improvements of the experimental setup will allow a reliable measurement of multiple Bragg reflections of the same object in future experiments. On dedicated samples, containing only a small number of nanoparticles at known positions, this has already been demonstrated [99].

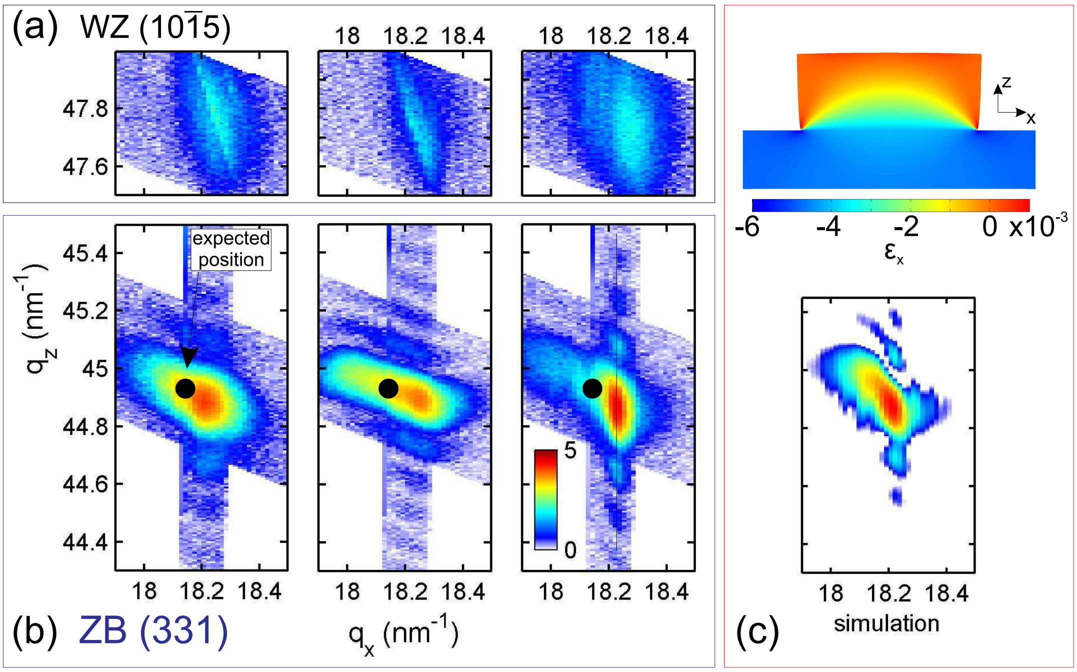

Figure 5.8: (left) Measured reciprocal space maps around the (a) $(10\bar{1}5)^{WZ}$ and (b) $(331)^c$ Bragg reflections of different nanowires. The asymmetry of the diffraction patterns indicates a strain-field in the nanowires. (c) Lateral component of the strain-field in a NW subjected to a compressive stress at its bottom obtained from a finite-element simulation (top). Using a maximum strain of $\approx -0.5\%$ at the bottom interface, the data can be qualitatively modeled (bottom).

In general, the reciprocal space maps differ significantly between different NWs, both for the $(1\,0\,\bar{1}\,5)^{WZ}$ and $(3\,3\,1)^{c}$ reflections. The much larger spread of the $(1\,0\,\bar{1}\,5)^{WZ}$ reflection along the q_z direction indicates the small size of the measured WZ units within the nanowires, which also causes an intensity drop by two orders of magnitude compared to the ZB reflections. Based on the width along the q_z direction, a length between 15 nm and 20 nm of the corresponding WZ segments can be estimated. For all data presented here, NWs with a particular high intensity the the respective Bragg reflection and therefore large amount of the corresponding structure have been selected. The data of the cubic segments measured at the $(3\,3\,1)^{c}$ reflection measured the ZB segments in the twinned orientation with respect to the substrate. As we have seen in the previous section, those NWs commonly exhibit only small segments in the non-twinned orientation. Nevertheless, it can not be excluded that the probed ZB segments are not located at the bottom of the NWs. However, the height measured by the thickness oscillations is smaller by about 10-20% compared to the total height of the NWs measured at the $(111)^{c}$ reflection ($\approx$80 nm), ensuring that the probed ZB segment can not be separated by more than, in average, 15nm from the substrate interface.

Also, the presence of a well defined Bragg peak and thickness oscillations indicate that the probed NWs can not contain a large number of ZB rotational twins or WZ segments, as the presence of twins and stacking faults would lead to a complex diffraction pattern around the inspected Bragg reflection (compare section 4.4). More strikingly, all Bragg peaks show a certain asymmetry along the q_x direction, most clearly visible at the more intense ZB reflections. Since the measurement probes the projection of a displacement field onto the diffraction vector, the visible asymmetry directly indicates residual strain within the nanowire. This effect was demonstrated recently at an example of highly strained surface gratings in [95]. The black spots in figure 5.8 (b) indicate the expected peak position of unstrained, ZB-type GaAs with the cubic bulk lattice parameter 5.6532 Å. All measurements show a shift of the maximum intensity towards larger q_x and smaller q_z, i.e. a lateral compression and an expansion along the growth direction. However, the amount of strain varies among the individual nanowires. The deviation of the Bragg peaks maximum, indicating the mean strain in the NWs, varies in the range $\frac{\Delta q_x}{q_x} = (3\,-5)\cdot 10^{-3}$ parallel to the surface, accompanied by a mean displacement of $\frac{\Delta q_z}{q_z} = -(0.8\,-1.3)\cdot 10^{-3}$ along the growth direction for the examples shown in fig. 5.8. Qualitatively,

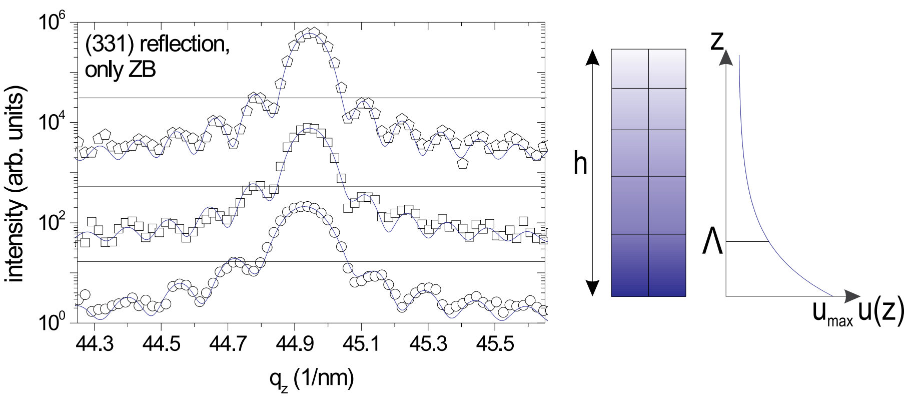

Figure 5.9: (left) Diffracted intensity distribution of single NWs around the zinc-blende $(331)^c$ reflection. To estimate the amount of strain in the ZB segments, a model based on a single ZB unit with exponentially decaying displacement field (right) has been fitted to the data (solid lines).

the visible asymmetry can be expressed as indication of a compressive lateral stress, whose origin might be either a different in-plane lattice constant along the hexagonal a^h direction between WZ and ZB material, creating a strain-field at the WZ/ZB heterojunction in the NWs, or a residual strain-field at the interface to the substrate. The observed NW diameter of 150 nm is larger than the expected critical diameter for dislocation-free growth of GaAs on Si, for which values between 40 nm and 110 nm have been reported [39, 50, 23]. Therefore dislocations will be present at the interface, which may relax the lattice mismatch only partially. The corresponding displacement field induced in the NWs, with components along the growth direction and parallel to the substrate plane, may cause the complex intensity-distribution in reciprocal space.

In order to determine which of the two scenarios - strain at a ZB/WZ heterojunction or residual strain originating from the substrate interface - is responsible for the observed effect, we first estimate the vertical strain $\epsilon_\perp$ in the measured ZB sections more quantitatively. To this end, line profiles along the q_z direction have been extracted from the reciprocal space maps (e.g. vertical line in fig. 5.8 (b)), and fitted by a model for the vertical displacement field as shown in figure 5.9. Here, we assumed a single ZB section of finite length with an exponentially decaying displacement field pinned at its bottom interface [39]. At this interface, strain may arise from one of the above scenarios. The assumption of a single ZB unit is only an approximation, as WZ segments will be included in the wire (compare fig. 5.6). However, the data can sufficiently be modeled using this simplified approach. The exponential decay is a reasonable approximation of the displacement field obtained by simulations of the elastic properties (see below).

Simulations based on our assumption (solid lines in fig. 5.9) show a maximum vertical strain $\epsilon_\perp$ at the bottom interface varying between $(0.3\pm0.1)\%$ and $(0.6\pm 0.1)\%$ among different nanowires, with an exponential decay length between 10 and 20 nm. The latter is reasonable, as finite element simulations of the elastic behavior of nanowires show that the nanowires are free of strain at a distance from a stressed interface comparable to the NW diameter. The estimated decay length is in the order of 15% - 30% of the average NW length, so only the lower part of the NW is subjected to strains larger than 0.1%. The estimated amount of strain fluctuates randomly and shows no correlation with the length of the ZB segment.

The corresponding strain $\epsilon_{||}$ parallel to the surface can be estimated using linear elasticity theory. To this end, the elastic constants of GaAs are taken into account in a rotated coordinate system with the hexagonal x_1 and x_2 axes parallel to the surface and the x_3 axis parallel to the NWs growth axis. Assuming a compressive stress along the x_1 and x_2 axis, the strain along the in-plane direction ($\epsilon_{||}$) is related to the strain along the growth direction ($\epsilon_\perp$) via the relation $\epsilon_{||} = -\frac{c_{33}^h}{2c_{13}^h}\epsilon_\perp$. Here, c_{33}^h and c_{13}^h are the elastic constitutive parameters of the GaAs in the hexagonal coordinate system. Following the approach by Martin [86], the coefficients can be calculated from the cubic bulk values given in Ref. [87] to be $c_{13}^h = 35.4\ GPa$ and $c_{33}^h = 153.8\ GPa$. Here it is important to note that the parameters c_{13}^h and c_{33}^h are identical in both WZ and ZB crystal structure. As result, a vertical strain of $\epsilon_\perp \approx 0.3\%$ should be accompanied by a maximum lateral displacement of $\epsilon_{||} \approx -0.65\%$.

Although the WZ phase of GaAs should exhibit a smaller lattice parameter along the hexagonal a^h direction than the ZB phase, the difference is expected to be in the range of -0.2% only. For WZ GaAs synthesized from a high pressure phase, McMahon et al. measured a value of $\frac{\Delta a_{WZ}}{a_{ZB,0}^h} \approx -0.22\%$ [91]. In section 5.8 we will observe a comparable value in GaAs NWs. Given that due to the elastic deformation of the nanowire at a hypothetical ZB/WZ heterointerface, the maximum strain $\epsilon_{||}$ will be even smaller in this case, our measurements favor the presence of residual strain at the substrate interface.

In order to compare the measured reciprocal space maps qualitatively with this assumption, a simplified simulation of the diffracted intensity based on a Finite Element model has been performed. The right part of figure 5.8 shows a simulation of the diffracted intensity around the $(331)^c$ reflection considering a 2-dimensional, homogeneous box of GaAs, subjected to compressive lateral stress at its bottom interface. A homogeneous stress was applied to the box by a temperature-induced shrinking of the substrate until the desired strain was reached. The corresponding displacement field in this 'nanowire' was calculated by means of a finite element approach implemented within the COMSOL Multiphysics package [25] (cf. sec. 6.3). Finally, the diffraction pattern was obtained by a two dimensional Fourier-transform of the displacement field according to equation (3.15). The top part of figure 5.8 (c) depicts the shape used for the simulation together with the lateral strain-field. Note that the substrate below the nanowire does not contribute to the simulated intensity due to its different lattice parameter. Also, the simplified assumption of a homogeneous stress at the bottom interface does not take into account any effects of dislocations, that will be present at the interface and relax most of the lattice mismatch, causing a more complex strain field in the nanowire. The maximum value of lateral strain at the NW bottom interface was varied, and an estimation of $\epsilon_{||} = -0.5\%$ leads to the simulated intensity distribution in the lower part of figure 5.8 (c), giving good qualitative agreement with the observed diffraction patterns.

5.7 Average strain release and interface structure

(published in paper [IV])

The measurements presented above indicate the presence of a residual stress at the interface between the NWs and the substrate, with the attributed strain field decaying along the growth axis of the nanowires. To verify this assumption, ensemble averaged diffraction experiments in a grazing incidence diffraction geometry have been performed on samples (A-C), probing the in-plane lattice parameter of the NWs as function of NW height. For shorter NWs, the deformation of the NWs lattice close to the interface will become stronger, which can be directly observed experimentally by the displacement of the respective Bragg peaks, giving an average information along the NWs height.

In order to probe the lattice parameters of the grown NWs, non-coplanar GID experiments have been performed at the P08 beamline of the PETRA III synchrotron source in Hamburg, Germany [128]. Here, the incoming x-ray beam with photon energy of 9 keV was diffracted from the sample mounted with the surface aligned vertically. The diffracted x-ray beam was integrated along the exit angle perpendicular to the surface using a one-dimensional position sensitive Mythen detector.

In the GID geometry, lattice planes perpendicular to the sample surface are probed which are most sensitive to the lattice accommodation at the nanowire-to-substrate interface. Due to refraction effects, even the respective Bragg reflections are accessible if incidence and exit angles $\alpha_{i,f}$ of the x-ray beam are small and close to the critical angle of total external reflection α_c [108] ($\alpha_c = 0.2^\circ$ for Si at 9 keV x-ray photon energy). A more detailed description of the GID geometry and the reflection and refraction effects of the x-ray beam at small incidence angles can be found in appendix C.

Due to the small incidence angles, the footprint of the x-ray beam on the surface is large and the measurements provide results averaged across the sample. Taking into account the size of the incident x-ray beam (50 μm x 50 μm) and the average dimension of the samples used (10 mm), the illuminated sample area amounts to 500.000 μm^2. With an average NW density of 1NW/μm^2, $5 \cdot 10^5$ NWs contribute to the diffraction signal.

Figure 5.10 schematically depicts a top-view of the experimental geometry together with the probed in-plane Bragg reflections of both cubic ZB and hexagonal WZ structures. For a given set of lattice planes (left), incidence- and exit angles are kept equal and varied in magnitude, defining the radial momentum transfer $q_r = \frac{4\pi}{\lambda} \sin(\theta)$ along the desired directions (dashed lines). As known from SEM images, the grown NWs exhibit $\{1\bar{1}0\}^c$ type facet orientations. The probed lattice planes in the experiment are either perpendicular to the side-facets (line (i)), or rotated by 30° along the 'edges' (line (ii)).

Results and discussion

Figure 5.11 shows the ensemble-averaged intensity distribution of samples (A-C)as a function of q_r parallel to the cubic $[20\bar{2}]^c$ direction. The curves have been recorded at an incidence angle of $\alpha_i = 0.2^\circ$ probing both the substrate and the base of the nanowires close to the substrate. Here, GaAs and Si peaks are well aligned along the $[20\bar{2}]^c$ direction, demonstrating the epitaxial relation between substrate and NWs. For all samples, the Si $(2\,0\,\bar{2})^c$ reflection of the substrate

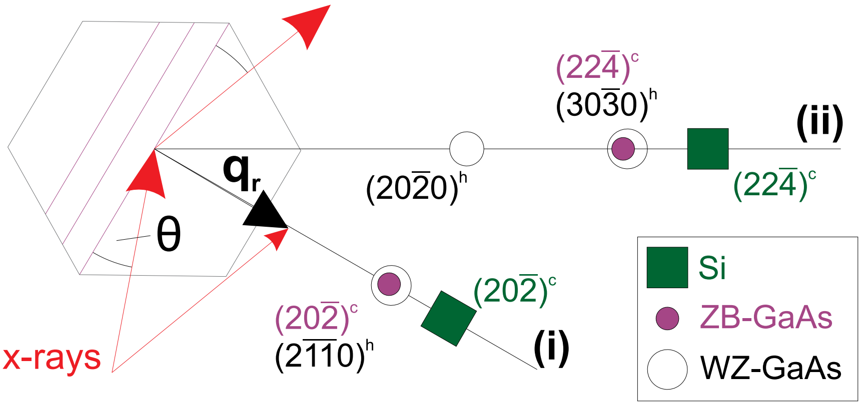

Figure 5.10: Sketch of the experimental geometry and measured Bragg reflections along the indicated lines (i) and (ii).

has been used as an internal reference. The corresponding GaAs reflection, located at smaller q_r, is allowed for both ZB and WZ crystal structures, where the indices are $(2\,0\,\bar{2})^c$ in the cubic and $(2\,\bar{1}\,\bar{1}\,0)^h$ in the hexagonal notation, respectively. The dashed vertical lines in fig. 5.11 indicate the expected peak positions based on the cubic bulk lattice parameters.

Sample (C) with the 1.2 μm long NWs shows a broad GaAs reflection located at the expected position of GaAs with ZB structure (dashed line). In this sample, a large amount of island-like crystallites is observed on the surface. Based on SEM images and the diffraction data presented above, they occupy around 50% of the GaAs volume and grow in the zinc-blende type structure. Hence, they may contribute to the respective Bragg-peak. However, almost no crystallites are observed for samples (A-B2).

For shorter NWs (samples B2, B1, and A), this Bragg peak becomes superimposed by a second maximum and shifts systematically towards larger q_r , i.e. smaller lattice parameters as a function of decreasing NW length. For sample (B2) the position of the second maximum, indicated by a vertical line, corresponds to the lattice parameter of the hexagonal wurtzite structure, which will be measured for thinner NWs with larger surface coverage in the following section. The appearance of this WZ type reflection is caused by the increasing relative WZ content in shorter NWs and the diffraction signal can be interpreted by a superposition of ZB and WZ type materials.

Besides this superposition of diffraction signals, for decreasing NW length both these WZ- and ZB type peaks become considerably shifted towards larger

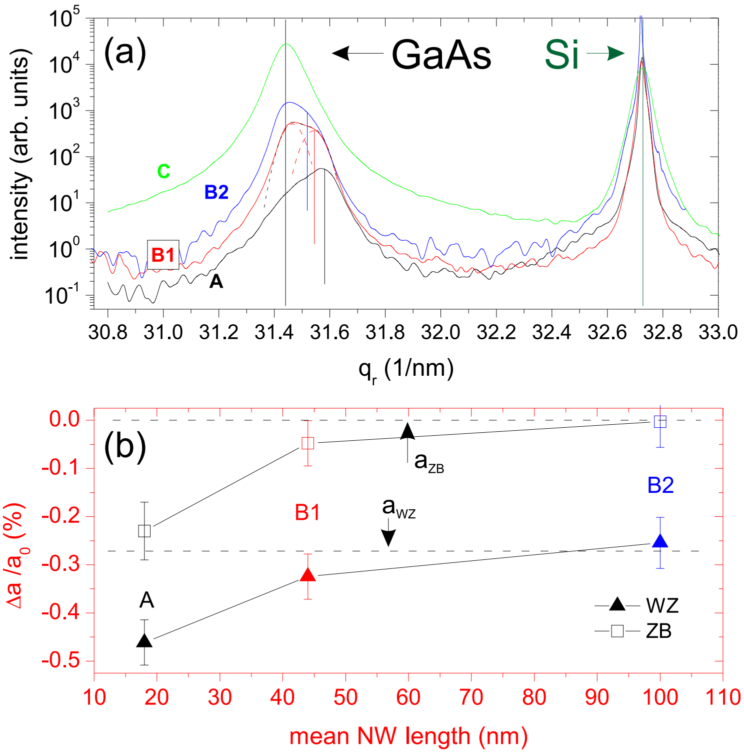

Figure 5.11: (a) Measurement along the $[2\,0\,\bar{2}]^c$ direction for samples (A-C). For shorter NWs, the NWs' Bragg peak shifts towards smaller lattice parameter (vertical lines: position of the WZ contribution, see text; dashed lines: bulk values). (b) Relative shift of lattice parameters of ZB and WZ contributions [vertical lines in (a)] compared to the bulk value. The NWs are compressively strained close to the substrate interface.

momentum transfer, i.e. even smaller lattice parameters. In addition, the Bragg reflection attributed to the WZ structure becomes relatively more intens, in agreement with the relative increase in WZ material in shorter NWs.

For a quantitative analysis, the diffraction profiles along q_r have been decomposed by a linear superposition of Gaussian profiles, representing an approximation for the mean WZ and ZB contributions. The determined maximum positions of the WZ-type peaks is shown by vertical lines in figure 5.11(a) and exemplarily, the deconvolution is shown by dashed profiles for sample (B1). Figure 5.11(b) shows the relative displacement $\delta a_{||}$ of the so-obtained WZ and ZB in-plane lattice parameters with respect to the bulk lattice parameter a_0^h (upper dashed line) as a function of mean NW height. The horizontal lines indicate the position of the bulk ZB material as well as the wurtzite lattice parameter that is observed in section 5.8. The data shows that the region close to the substrate-interface is compressively strained, exhibiting mean strain values of up to $\delta a_{||} = -(0.23 \pm 0.06)\,\%$ for the shortest NWs. Due to the small NW height, the measurement represents the averaged information along the growth axis. The decrease of the measured strain value with increasing NW height therefore represents a measure for a relaxation of a displacement field along the growth axis, showing that the base of the NWs is compressively strained at the interface towards the substrate.

Interface structure

In order to characterize the NWs' interface towards the substrate and to identify the origin of the strained interface region, TEM measurements at selected NWs have been performed.

Figure 5.12(a) shows a high resolution (HR)TEM micrograph of the interface region of a NW from sample (B1), obtained along the $[1\,1\,\bar{2}]$ zone axis. The image demonstrates that the interface between NW and substrate (right) is significantly roughened compared to the free Si surface (left). The smoothness of the free Si surface indicates that the roughness of the GaAs-Si interface is related to the growth process. The rough interface extends about 3 nm along the growth direction.

This increased interface-roughness can be explained by the reaction of the liquid Ga-droplet with the top layer of the substrate during the initial stage of growth, in which the oxide layer, and probably parts of the Si substrate, are dissolved by the liquid Ga until NW growth starts. Similar reactions of Ga with a Si substrate, denoted as meltback-etching, have been observed for GaN growth on Si [62, 27]. We expect that due to the large contact area between droplet and substrate the initial etching process is more pronounced for thicker NWs. In the next section we will observe that considerably thinner NWs show a smooth interface structure.

Besides the high interface roughness, misfit dislocations can be observed at the interface (not shown, compare [16]). On average, the dislocations are separated laterally by a distance of (5.3 ± 0.5) nm. Assuming 60°-type misfit dislocations, this average distance would be sufficient to accommodate nearly the entire lattice mismatch between GaAs and Si. However, the large interface roughness may hinder the movement of misfit dislocations to the equilibrium positions for complete plastic relaxation, and thus effectively prevent the complete strain release. The residual strain in GaAs near the interface may depend on the particular interface morphology, which explains the variations observed in the diffraction measurements at different NWs.

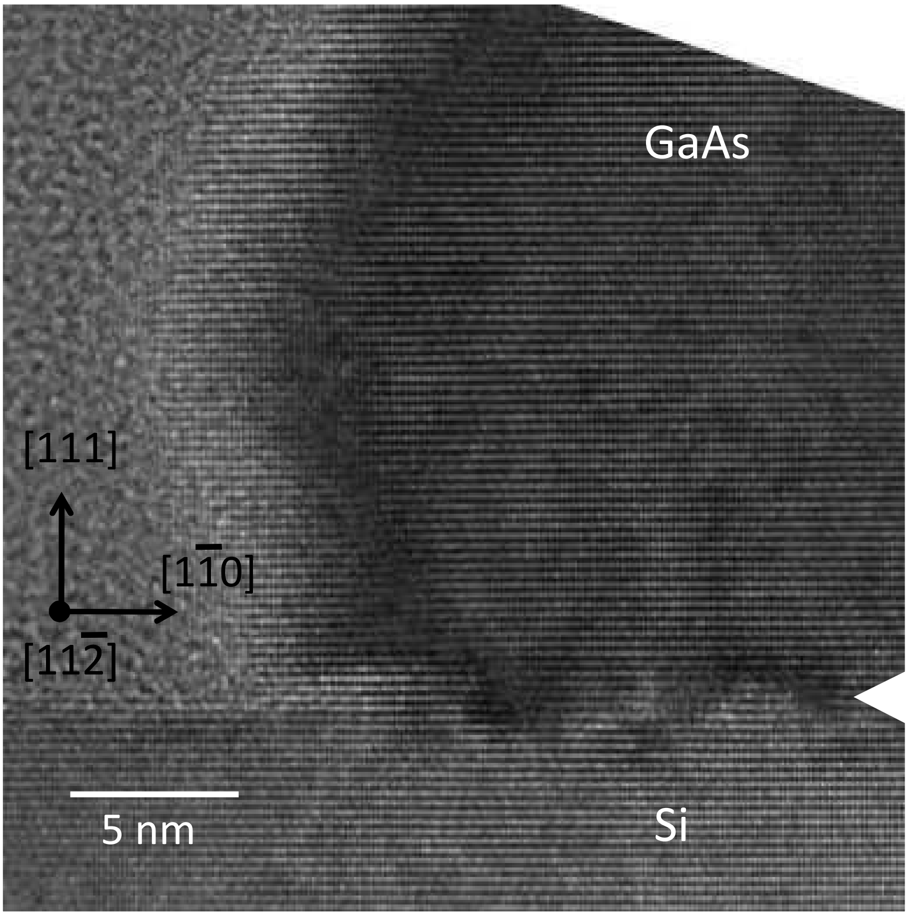

Figure 5.12: High-resolution TEM image of the interface region of a NW on sample (B1) along the $[1\,1\,\overline{2}]$ zone axis, showing the rough interface structure between the NW and the substrate, probably caused by a meltback-etching reaction of the liquid Ga droplet with the Si substrate. Due to the rough structure, the existing dislocations can not glide to their equilibrium positions for complete relaxation, leading to a residual strain in the NW.

5.8 Relaxation of thin nanowires

(published in paper [IV])

The NWs investigated in the previous section have diameters above 100 nm and hence, dislocations are expected to be present at the interface. However, a critical diameter for dislocation free growth of 100 nm has been predicted theoretically for the case of GaAs NW growth on Si, and indeed defect free interfaces have been reported for NWs grown by SA-MOVPE and diameters below 20 nm [136]. In order to probe whether pseudomorphic growth can also be obtained using the Ga assisted growth mechanism presented above, a second set of samples has been investigated, exhibiting significantly smaller diameters between 10 nm and 50 nm.

This series of nanowires (α-γ) has been grown using the same preparation scheme as series (A-C), described in the previous section. However, the NWs have been grown on a lowly arsenic-doped Si substrates from *SiMat* with a resistivity in the low Ωcm range, resulting in diameters below 50 nm. In contrast, NWs with much larger diameters (samples A, B, C) had been obtained for growths on more highly arsenic-doped Si substrates. We suppose that the effect of substrate dopant concentration on nanowire diameter may be related to differences in the native oxide layer. The NW diameter is determined by the size of the initial Ga droplet, which in turn results from the interplay between the accumulation of liquid Ga and the etching of the oxide by the Ga droplet before the droplet is lifted up by the growing GaAs NW. It has been reported that the thickness of the native oxide very sensitively affects the NW diameter [75], and the oxide thickness is known to depend on the substrate dopant concentration [98].

Figure 5.13 displays SEM images of the growth series (α-γ). The NWs are grown with significantly smaller diameters than on series (A-C), and both nanowire height and diameter increase during growth. On sample (α), first nanowires with diameters of about 10 nm and similar height have formed. With increasing growth time, the NWs increase both in diameter and length. On sample (β), diameters and a length of around 30 nm are obtained, until after 1000 s of growth (γ) diameter and length increased to around 40 nm and 230 nm, respectively. Similar to series (A-C), island-like structures are observed between them for long growth times. The surface coverage obtained under the used growth conditions is about 10 NWs/μm^2. Table 5.2 summarizes the parameters of the investigated samples.

Table 5.2: Overview of growth-time (t_g), length (L) and diameter (D) of the inspected NWs in series (α-γ). The average as well as the standard deviation obtained from measurements of at least five nanowires are shown.

Sample	α	β	γ
t_g / s	10	100	1000
L / nm	6±1	32±8	232±7
D / nm	13±3	28±3	42±4

Figure 5.14(a) shows the ensemble-averaged intensity distribution of samples (α-γ) as a function of q_r parallel to the cubic $[20\overline{2}]^c$ direction, measured in the GID geometry at an incidence angle of $\alpha_i = 0.2°$. The measurements were performed with the same experimental conditions as used for samples (A-C) in the previous section.

Most importantly, already sample (α) shows an isolated Bragg peak that is displaced by $\Delta a_{\mathrm{GaAs},\alpha}/a_{\mathrm{Si}} = 3.8\%$ with respect to the silicon substrate, corresponding to 90% of the difference between the in-plane lattice parameters of GaAs and Si. The large width of the Bragg peak measures the small diameter of the NWs ($\approx 10\,\mathrm{nm}$). Due to this large width and small intensity, the precise determination of a lattice parameter is not possible here. However, the data clearly indicate that no pseudomorphic growth is obtained even for thin nanowires. In case of pseudomorphic growth, a gradual change in lattice parameter close to the NW-substrate interface would be required, leading to a much higher scattering intensity between the NW peak and the Si Bragg peak. Instead, HR-TEM investigations (see below) could confirm that the inclusion of misfit dislocations at the interface between NW and substrate leads to plastic relaxation of the lattice mismatch.

For sample (β), the NW -peak increases in intensity, but otherwise maintains the same maximum position as found for sample (α). In addition, size- oscillations can be observed around the Bragg peak, originating from the finite size of the NWs (arrows in fig. 5.14(b)). The appearance of size oscillations implies a rather homogeneous size-distribution of the NW ensemble. Simulations of the diffracted intensity (dashed line, vertically shifted for clarity) indicate an average size of 26 ± 2 nm, in good accordance with the SEM results, and a lattice parameter of $a^h_\beta = (3.987 \pm 0.002)$ Å.

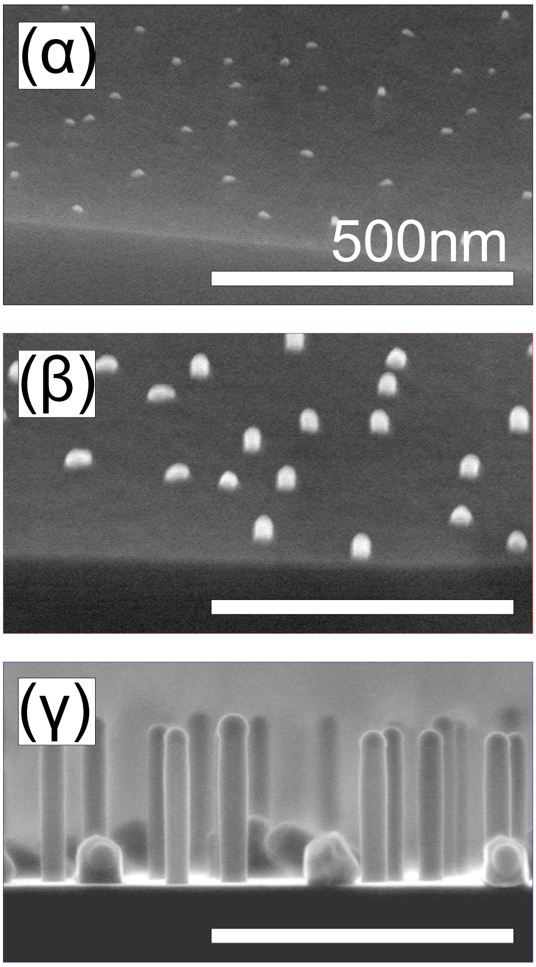

Figure 5.13: SEM pictures of the inspected GaAs nanowires in series (α-γ). The diameter of the NWs increases from $\approx$ 10 nm (α) to $\approx$ 40 nm (γ). For short growth times, the NWs are well isolated on a smooth surface. For long growth times, small island-like structures are visible between the wires. All scale-bars 500 nm.

Compared to sample (α) and (β), the diffraction maximum of sample (γ), exhibiting the longest NWs of up to 250 nm length, is shifted towards the bulk ZB GaAs position, measuring a lattice parameter of $a^h_\gamma = (3.994 \pm 0.001)\,\text{Å}$, slightly smaller than the expected value for bulk GaAs. In this case, size oscillations show an average NW diameter of 45 ± 2 nm, also in good agreement with the SEM value. In addition, the diffracted intensity shows a slight asymmetry towards the position of samples (α / β).

The integrated intensities measured at selected WZ and ZB type reflections in an asymmetric scattering geometry (cf. section 5.3) show that sample (β) consists of more than 60% WZ, whereas only in total 6% WZ can be found in sample (γ). We therefore interpret the observed in-plane lattice parameters in

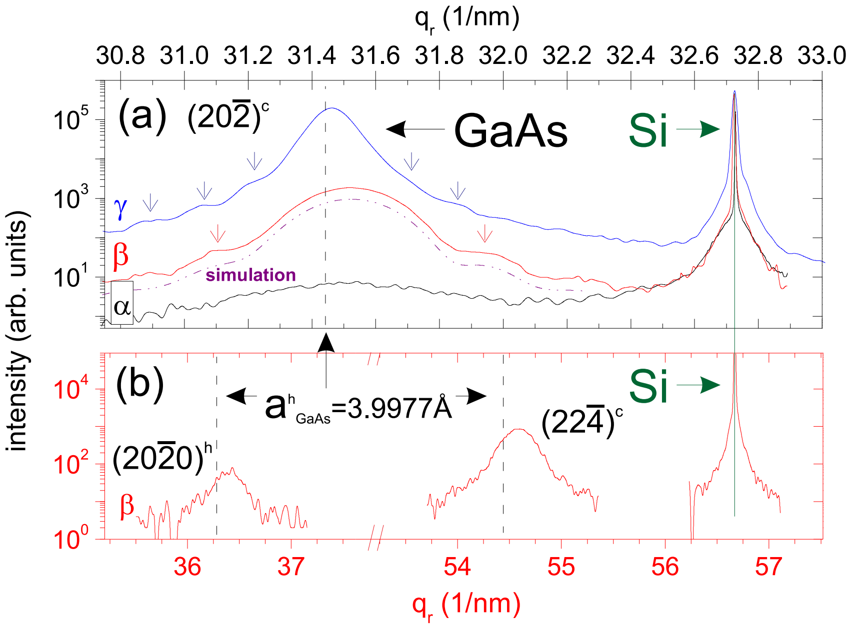

Figure 5.14: Intensity distribution along the $[2\,0\,\overline{2}]^c$ (a) and the $[2\,2\,\overline{4}]^c$ direction (b) for samples (α-γ), corresponding to directions (i) and (ii) in fig. 5.10. Clearly visible is a shift in position of the maximum GaAs intensity for sample (β) compared to the expected position for bulk ZB GaAs (vertical lines). Size-oscillations are seen [arrows in (a)], originating from homogeneous NW diameters.

samples (α) and (β) to be the in-plane lattice parameter of the hexagonal WZ phase.

The attribution to WZ and ZB phases is verified by measurements along the $[1\,1\,\overline{2}]^c \equiv [1\,0\,\overline{1}\,0]^h$ direction for sample (β), shown in fig. 5.14(b). Here, the $(2\,0\,\overline{2}\,0)^h$ reflection is allowed for the WZ structure only, whereas the cubic $(2\,2\,\overline{4})^c$ reflection is equivalent to the hexagonal $(3\,0\,\overline{3}\,0)^h$ reflection. All reflections show the same displacement with respect to the expected bulk position, verifying that the observed lattice parameter belongs to the WZ crystal structure. Combining all measured reflections, we obtain a mean value of $a^h_{\mathrm{WZ}} = (3.987 \pm 0.001)\,\text{Å}$ for the lattice parameter of sample (β). This is in good agreement with values reported for Au-assisted grown, mainly WZ-type GaAs nanowires by Tchernycheva et al. (3.988 Å) [134] and for WZ-type GaAs obtained by a high pressure synthesis by McMahon et al. ($a^h_{\mathrm{WZ}} = (3.989 \pm 0.001)\,\text{Å}$) [91]. Compared to the bulk value of the ZB phase $a^h_{0,\mathrm{GaAs}} = 3.9977\,\text{Å}$, the WZ phase shows a relative decrease in the hexagonal lattice parameter of $\Delta a_{WZ}/a^h_{0,\mathrm{GaAs}} = (-0.27 \pm 0.02)\%$.

The agreement between the measured value for the WZ lattice parameter and the expected values from literature corroborates the conclusion that these thin NWs are free of strain even at the bottom. This finding is confirmed further by the comparison of samples (β) and (α). For elastically strained NWs, the position of the corresponding Bragg reflection would show a dependence on the NW height, as the displacement field would be stronger towards the bottom of the NWs (compare samples (A-C) above), but such a peak shift is not observed.

Interface structure

Figure 5.15 displays a typical high-resolution (HR)TEM micrograph of a short NW from sample (β) taken along the Si $[1\,\bar{1}\,0]$ zone axis. The diameter of the imaged NW amounts to about 25 nm. A short segment of cubic structure directly above the substrate is followed by a region with many stacking faults and then a segment with mostly hexagonal stacking sequences as indicated in the figure. The lattice mismatch to the Si substrate is accommodated by the formation of misfit dislocations along the interface. The magnified image of the interfacial area, which is additionally noise-reduced by Fourier filtering, clarifies the location (marked by the arrow) as well as the edge character of the misfit dislocation. Besides the presence of dislocations, the interface between NW and substrate is smooth, and for most NWs inspected by TEM, an amorphous layer between crystalline GaAs and Si is observed at the outer parts of the NW, which can be attributed to the initial oxide layer. The presence of dislocations together with the smooth interface structure explains the complete strain release in these thin NWs. Note that for the small interface region between NW and substrate, only a small number of dislocations is necessary to relieve the entire lattice mismatch.

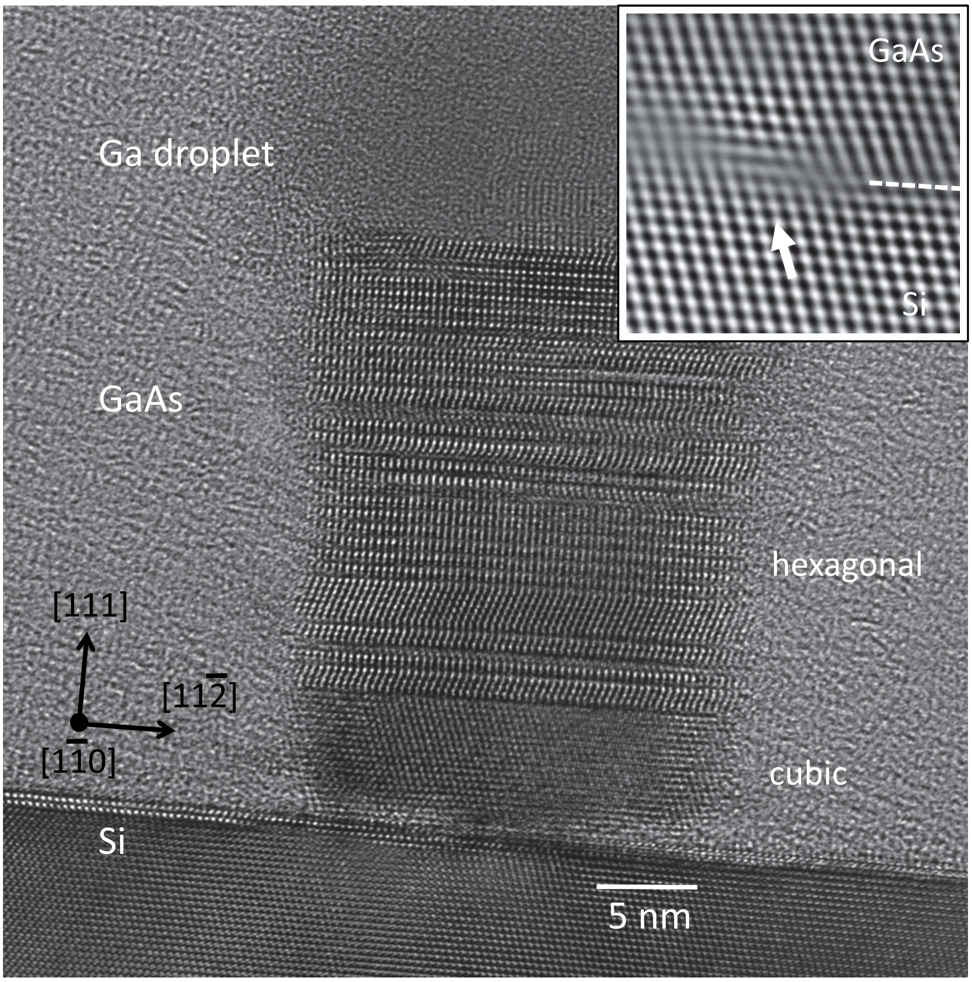

Figure 5.15: HRTEM micrograph of a nanowire of sample (β). The NW with diameter of 25 nm shows segments of cubic and hexagonal stacking. Dislocations can be found at the interface between NW and Si (arrow in Fourier-filtered image of the interface region in inset).

5.9 Summary

In summary, the presented experiments show that using the Ga-assisted growth mechanism of GaAs NWs on Si (1 1 1), no pseudomorphic NW growth is obtained even for NWs with diameters as small as 10 nm. While the NWs with diameters below 50 nm are completely relaxed, NWs with diameters above 100 nm are affected by a residual strain at the interface with the substrate, decaying elastically along the growth direction. These NWs exhibit a rough interface structure, most likely caused by an initial meltback-etching process of the liquid Ga droplet with the Si substrate. Although a high number of dislocations is introduced, the interface roughness prevents full strain release. In contrast, NWs with diameters below 50 nm are free of strain because the smooth interface to the Si substrate allows complete plastic relaxation.

This finding is in contradiction to a theoretical analysis that predicts dislocation-free growth for NW diameters below $\sim$ 100 nm [152]; and for NWs grown by selective-area MOVPE no dislocations were observed by HR-TEM if the NW diameter was below 20 nm [136]. However, it is important to realize that the interface structure is not only influenced by lattice mismatch and strain but also by the interface chemistry. The case of Ga-assisted GaAs NW growth on Si is particularly complex, because the interplay between liquid Ga, solid Si, and the thin oxide layer has to be taken into account. However, little is known about NW nucleation in this framework. Our results demonstrate that more effects than the elastic energy have to be taken into account to describe whether NW growth takes place without the introduction of dislocations.

In addition to the strain relaxation, during the initial stage of growth both thick and thin NWs contain large amounts of the wurtzite phase. Using x-ray diffraction on single nanowires, the position and amount of the WZ material along the growth axis could be quantified, showing a mixture of extended ZB and WZ segments during the beginning of growth. For longer NWs, the growth is dominated by the ZB structure.

We found that the wurtzite structure of GaAs has a smaller in-plane lattice parameter with mismatch of $\frac{\Delta a_{WZ}}{a^h_{ZB,0}} = -(0.27 \pm 0.02)$ %, but a larger lattice plane spacing along the growth direction of $\frac{\Delta c}{c} = (0.7 \pm 0.05)\%$ compared to the purely geometrical expectation based on zinc-blende GaAs.

Coming back to figure 4.11, the observed lattice parameter change of the WZ structure (hexagonality 100%) is compared with the results obtained in chapter 4 for NWs exhibiting a high density of ZB-twins, leading to a less pronounced change in lattice parameters. The data shows the relative increase in the $(1\,1\,1)^c$ lattice plane spacing $\Delta c/c$ as function of the relative decrease of the in-plane lattice parameter $\Delta a/a$ of the WZ structure compared to the ZB case (first data point). The dashed line represents a linear fit to the data, giving reasonable agreement. The inset shows the c/a - ratio as function of the hexagonality of the structure, and compares them with theoretical expectations based on density functional theory calculations [106]. Whereas a linear increase is observed in both cases, the measurements in this work indicate a slightly stronger increase up to a value of 1.649 ± 0.001 for the WZ structure.

6 Strain in core-shell nanowire heterostructures

In the previous chapters, x-ray diffraction has been used to determine the shape, structural composition and strain in pure GaAs nanowires. However, for most technological applications, the formation of heterostructures (HS) in the NW geometry is required, combining materials of different properties (e.g. bandstructures) and usually also different lattice parameters. In this case, strains or defects may arise from the heterointerface, and x-ray diffraction provides a valuable tool to study strains or chemical changes at heterointerfaces. As example and outlook for future nanodiffraction experiments, first investigations of the strain effects at a heterointerface in a core-shell NW geometry are presented in this chapter. In section 6.1, a brief introduction to NW heterostructures is given together with the description of the investigated system. First experimental results on the axial strain in a GaAs core / InAs shell heterostructure are presented in section 6.2, followed by an interpretation of the data based on an incomplete relaxation at the heterointerface. In addition, a short description of finite element simulations of the elastic interaction in this heterostructures is given in section 6.3.

6.1 Nanowire heterostructures

In general, two different geometries for a NW-heterostructure are considered and depicted in figure 6.1. In an axial HS, two materials are combined along the growth direction, whereas in a radial HS, a NW *core* is surrounded by a *shell* or multiple shells of different material. In practice, the axial HS allows to form defect-free interfaces between lattice mismatched materials, as strain is assumed to be released by elastic deformation of the NW towards the side walls [10, 39, 50]. In this geometry, the formation of small quantum-dot like structures can be achieved, with possible applications as resonant tunneling diodes [11] or light emitting diodes [55]. However, for many practical purposes the growth of this heterostructures is challenging. For example, in the case of the VLS mechanism the composition of the liquid droplet needs to be changed in order to form the HS, which frequently leads to a gradual change in the chemical composition along the growth direction and no sharp interfaces are obtained [76, 33]. Furthermore, straight nanowires are frequently observed only in one interface direction [36, 92] and growth conditions (e.g. temperature, partial pressures) might be strongly different for the two materials. Compared to this, the formation of core-shell systems is frequently more easy to obtain. Here, the core, which might be grown by VLS, needs to be overgrown radially, which is similar to the growth of planar layers on the sidewalls of the NW. As no liquid droplet is required for this overgrowth, sharp interfaces are more readily obtained here. However, in terms of interface-quality a possible drawback in this geometry is the larger interface area, leading to higher strain energy densities and the formation of defects to release lattice mismatches plastically.

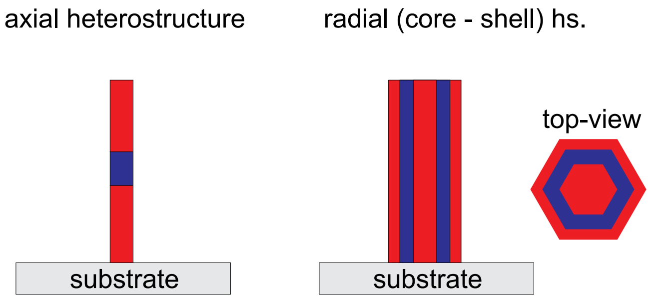

Figure 6.1: Schematic representation of an axial nanowire heterostructure (left) and a radial (core-shell) heterostructure (right).

In the core-shell geometry, only small shell thicknesses can be grown coherently, and for typical NW diameters, the critical thickness for dislocation free growth is only slightly larger than for planar films [118, 119]. In the case of highly lattice mismatched III-V NW heterostructures, the relaxation of InAs core - GaAs shell nanowires has most extensively been studied. The cubic bulk lattice parameters of this materials are $a_{\mathrm{InAs}} = 6.0583\text{Å}$ and $a_{\mathrm{GaAs}} = 5.6536\text{Å}$, corresponding to a lattice mismatch of $\delta a = \frac{a_{\mathrm{InAs}} - a_{\mathrm{GaAs}}}{a_{\mathrm{GaAs}}} = 7.16\%$ [79]. In this system, a fast relaxation along the radial direction has been reported, whereas a slower and gradual relaxation in axial direction was observed [69, 113, 70]. The faster radial relaxation is caused by the energetically favored formation of edge dislocations releasing the strain along the circumference of the NW more easily compared to axial relaxation, which is observed to occur gradually [70]. For wurtzite type InAs NWs with a GaAs shell, a sudden and nearly complete radial strain release as function of shell thickness was observed, accompanied by a gradual axial strain relief saturating at values of around 80% [69].

However, whereas the relaxation is commonly related to the shell, the possibility of strain in the core is often neglected and cannot, or only hardly, be accessed independently if, using TEM, the separation of Moiré fringes is used to calculate the degree of relaxation, or the splitting of electron diffraction peaks.

Complementary to electron microscopy, x-ray diffraction can be used to monitor the relaxation in core-shell nanowire heterostructures. Goldhorpe et al. measured the shell-induced strain in thin Ge-core / Si-shell NWs with core diameters below 30 nm. Compared to the InAs/GaAs case, a faster strain relaxation along the axial direction was observed in this system [53]. Keplinger et al. studied the limits of pseudomorphic shell growth in the InAs core / InAsP shell system using grazing incidence diffraction, and observed pseudomorphic growth for mismatches below 1%, considerably smaller than the 7.16% in the InAs / GaAs system [71].

In this chapter, we study the axial strain relaxation in GaAs core / InAs shell nanowire heterostructures using x-ray diffraction. Besides a gradual relaxation of the shell, we find a significant impact of strain in the GaAs core, increasing with shell thickness. This increasing strain can be explained by a saturation of the dislocation density at the core-shell interface. Based on TEM investigations, a maximum axial relaxation of 80% is obtained. Independent measurements of core and shell reveal a higher relaxation of the shell (93% of the initial mismatch with GaAs) , together with a tensile strain in the core, leading to a change in the distances in Moiré patterns and subsequently an underestimation of the relaxation if the shell is considered alone.

Here, only the axial relaxation will be discussed. A detailed study of the radial relaxation, which can be expected to occur more suddenly, will be subject of future work.

Sample description

The GaAs NW cores were grown by MBE using the Ga-assisted growth mode on a GaAs (1 1 1) surface covered by a thin SiO layer [120] [14]. The core growth was

---

[14] The core-shell NWs have been grown and analyzed with electron microscopy by Torsten Rieger at the Peter Grünberg Institute (PGI-9), Forschungszentrum Jülich, Germany.

performed using a substrate temperature of 590°C, a Ga rate of 0.075 μm/h and an As flux of 1x10^{-6} torr for 45 minutes, resulting in a mean diameter of 70 nm-80 nm along the $[1\,1\,\overline{2}]$ direction and a length of 1.2 μm. After the core growth, the samples were kept 10 minutes at constant temperature and As flux in order to consume the Ga droplet. The NW cores exhibit the cubic zinc-blende structure with few rotational twins and a short segment of the hexagonal wurtzite phase at the top of the wire, created during the consumption of the liquid Ga droplet [120]. Then, the substrate temperature was ramped down to 490°C and the growth of the InAs shell was initiated using the same As flux as for the core and an In rate of 0.1 μm/h. Three samples were grown with shell growth times ranging from 5 to 30 minutes. Additionally, one sample was grown without the InAs shell.

During the initial stage of InAs growth, InAs islands are formed on the core's $[1\,\overline{1}\,0]$ side facets, which coalesce and form a closed shell after a thickness of 5 nm [121]. Measurements of Moiré patterns in TEM indicate a saturation of the axial relaxation at around 80% of the total mismatch, comparable to the InAs-core/ GaAs-shell case [69]. A set of these NWs with closed InAs shell has been selected for x-ray diffraction experiments.

Figure 6.2 shows scanning electron micrographs of the pure GaAs NWs (a) and the GaAs NWs covered by a 12 nm (b), 20 nm(c) and 35 nm (d) thick shell of InAs, respectively. For all samples, the shell thickness was determined by transmission electron microscopy after the transfer of NWs from the substrate to a TEM grid. Note that besides the increasing diameter of the NWs observed in SEM, parasitic growth of crystallites occurs during InAs deposition in between the NWs.

High resolution x-ray diffraction experiments have been performed at the P08 beamline of the PETRA III synchrotron source. In addition, diffraction measurements using the nano-focussed x-ray beam have been performed at the ID01 beamline of the ESRF synchrotron source in order to verify the attribution of the diffraction signals to nanowire core, shell and crystallites, respectively.

6.2 Axial strain measurements in core-shell NWs

Figure 6.3 (a) shows a reciprocal space map around the GaAs $(111)^c$ reflection of the bare GaAs NWs. X and y axis measure the momentum transfer of the diffracted x-ray beam parallel to the surface (q_x) and perpendicular to it (q_z),

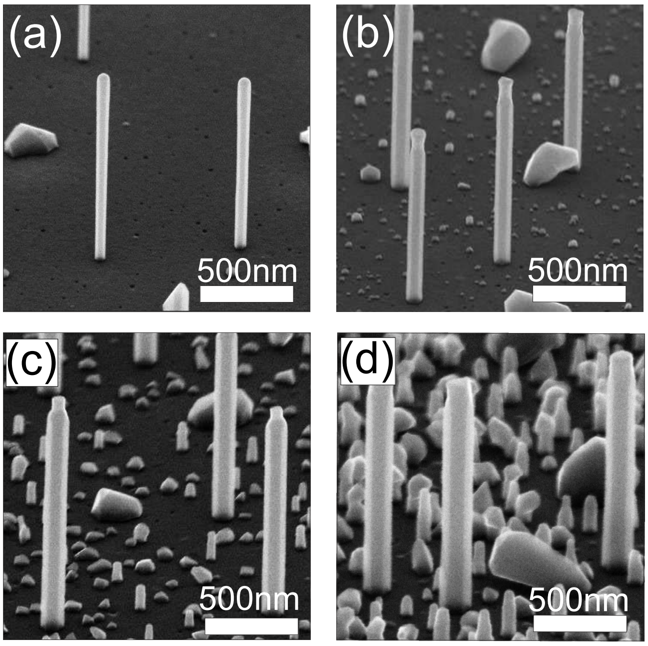

Figure 6.2: SEM images of the inspected NWs. 1.2 μm long GaAs NW cores (a) are covered by an InAs shell of 12 nm (b), 20 nm (c) and 35 nm (d), respectively. Together with the growth of the InAs shell, parasitic InAs growth occurs in between the initial NWs.

respectively (compare fig 6.3 (e)). The GaAs substrate creates a sharp Bragg peak (s) in reciprocal space, superimposed by a crystal truncation rod originating from the surface of the substrate (vertical streak in (a)) as well as crossed streaks of intensity caused by the crystal-monochromator and the detector, respectively [108]. Compared to that, the finite size and a possible random tilt of the GaAs nanowires leads to an elongated diffraction signal along the q_x direction in reciprocal space, allowing to separate the contributions from NW cores ('co') and substrate. For the pure GaAs NWs, the elongated signal coincided with the substrate signal, indicating that the NWs grow in the cubic zinc-blende structure exhibiting the bulk lattice parameter in agreement with TEM investigations. In addition, a second signal is observed displaced by $\Delta q_z/q_z \approx -0.5\%$ along the vertical direction. This signal can be attributed to wurtzite segments that are observed close to the tip of the NWs and are known to exhibit an increased lattice plane spacing along the growth direction compared to the ZB structure (cf. chapter 5).

If a completely relaxed InAs shell is grown around the NW core, the larger $(111)^c$ lattice plane spacing of InAs leads to a Bragg peak located at smaller vertical momentum transfer. However, if the InAs shell is subjected to compressive strain, the diffraction signal will be displaced along q_z towards the GaAs position.

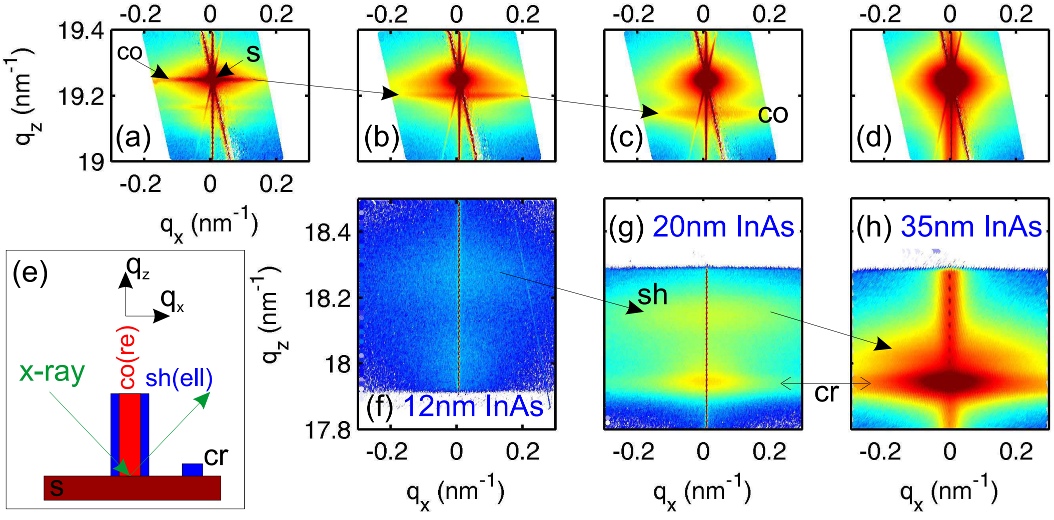

Figure 6.3: X-ray reciprocal space maps around the GaAs $(111)^c$ (a-d) and InAs $(111)^c$ (f-h) reflections of all investigated samples. With increasing shell thickness, the diffraction signal of the GaAs core (co) is displaced from the substrate (s), which is used as reference. Simultaneously, the shell (sh) shows a gradual relaxation and InAs crystallites (cr) grow. (e) shows a sketch of the diffraction geometry.

In figure 6.3 (b-d), the same region in reciprocal space is shown for the NWs covered with increasing InAs shell thickness. (f-h) show the corresponding region around the InAs $(1\,1\,1)^c$ reflection, respectively. Most strikingly, with increasing shell thickness the diffraction signal attributed to the GaAs core ('co' in (c)) shifts towards smaller momentum transfers, indicating a mean increase of the lattice plane spacing. This shift is indicated by arrows between figures 6.3 (a-c). Simultaneously, the peak broadens considerably, until for a 35 nm thick shell (d), no distinct GaAs core reflection is observed anymore. In the latter case, the entire CTR of the substrate is surrounded by a strong diffuse scattering signal originating from the high surface coverage by parasitic crystallites, possibly shadowing the small core signal. For all shell thicknesses, the diffraction signal of the InAs shell (fig. 6.3 (f-h)) consists of a superposition of two maxima, out of which one is located at the position of bulk ZB InAs ('cr') and the second one is displaced ('sh') towards larger q_z, i.e. smaller lattice parameters. Spatially resolved nanodiffraction experiments using a focused x-

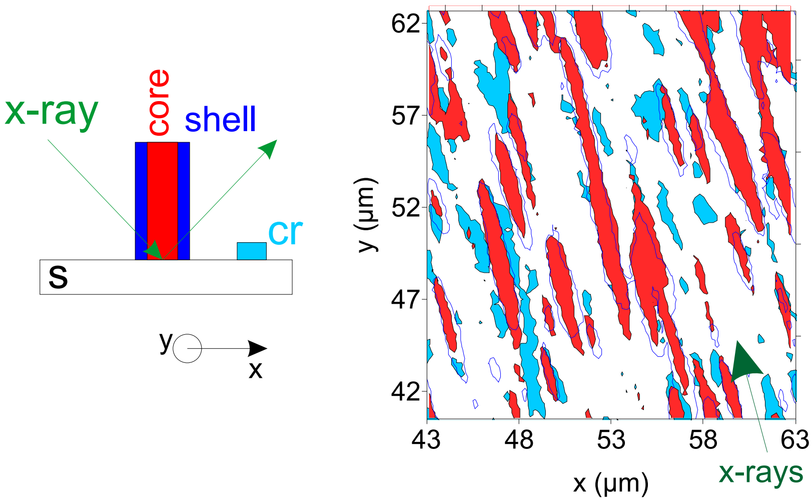

Figure 6.4: Position-resolved intensity distribution of the Bragg peaks assigned to GaAs core (red filled), InAs shell (blue contours) and parasitic InAs crystallites (light blue filled). Using a piezo positioning system, the sample is scanned below the stationary focused x-ray beam. The projection of the inclined x-ray beam on the surface is marked by the arrow. The height of the NWs and the inclined x-ray beam leads to the elongated spots in the intensity-map. Whereas the diffraction signals assigned to core and shell show the same spatial distribution, the additional InAs signal assigned to the crystallites is only present on areas in between, in agreement with the observations by scanning electron microscopy.

ray beam showed that the displaced GaAs and InAs diffraction signals originate from identical positions on the sample (the NWs with shell), whereas the relaxed InAs signal is caused by smaller structures in between (figure 6.4). This compares well with the observation in figure 6.2, showing an increasing amount of parasitic InAs growth on the oxide covered surface during the shell deposition.

The mean strain values in GaAs core and InAs shell can be determined from their respective peak positions ('co' and 'sh' in fig. 6.3) and are plotted in figure 6.5. The values are calculated with respect to the lattice plane spacing of unstrained material, taken from the position of the GaAs substrate reflection and the InAs crystallites measured simultaneously. The error bars are determined from the full width at half maximum of the diffraction signals and indicate the spread of the lattice parameter distribution rather than the experimental resolution ($\Delta a/a \approx 1 \cdot 10^{-4}$). Whereas the InAs shell is under axial compressive strain, the GaAs core is tensile strained, increasing from 0.25% for 12nm thick InAs to 0.5% for a 20nm thick InAs shell.

The inset in figure 6.5 shows a TEM micrograph of a NW with 20 nm thick InAs shell. In the central region, a Moiré pattern is visible due to the overlapping lattices of core and shell. From the separation of the Moiré fringes, the mismatch between both lattices can be obtained. For comparison, green triangles show the strains in the shell based on the TEM investigation, if only a deformation of the shell, but no change in the core lattice parameter is considered. The TEM data shows a saturation of the strain in the shell around $(\Delta a/a)_{\text{shell}} \approx -1.5\%$, corresponding to a relaxation of 80% compared to bulk values[15]. Compared to this, the x-ray data clearly shows a smaller compressive axial strain in the shell, decreasing to $(\Delta a/a)_{\text{shell}} \approx -0.5\%$ for 35 nm shell thickness. Compared to the bulk lattice parameters of GaAs and InAs, this corresponds to a relaxations of 93%, larger than observed by TEM. However, this discrepancy is resolved if the experimentally observed changes of *both* core and shell lattice parameters are considered. In this case, the *relative* difference of the core-shell lattice parameters amounts to $\approx$ 80% for all measured samples.

6.3 FEM simulations

The increasing strain in the core for larger shell thickness indicates that the plastic relaxation of the shell by inclusions of misfit dislocations is incomplete and does not reach 100%. This situation will lead to an remaining effective lattice-mismatch and hence stress at the heterointerface. Under the assumption that a residual stress remains, an increasing shell thickness will lead to a more efficient relaxation of the shell, accompanied by a higher strain in the core induced by the increasing shell thickness.

Besides the increasing strain, the diffraction signal of the core indicates a rather homogeneous displacement throughout the entire core region. In order to determine whether the observation of a homogeneous, increasing strain is consistent with the assumption of an incomplete plastic relaxation, the elastic interaction between core and shell has been simulated within a finite element approach in the COMSOL Multiphysics package [25]. FEM methods have

---

[15] TEM investigations have been performed for more combinations of shell thickness and core diameter, all showing a saturation with increasing shell thickness (not shown here).

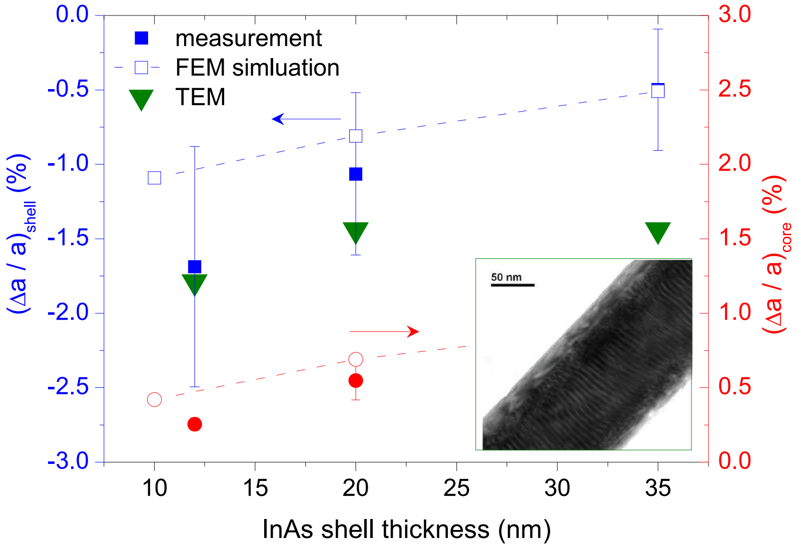

Figure 6.5: Average change of core (red spheres) and shell (blue squares) lattice parameters along the growth direction as function of shell thickness. Error bars measure the observed spread from the FWHM in fig. 6.3. Open sympols: Results of a finite element simulation, cf. section 6.3.

been used before to study the in-plane strain distribution for the example of GaAs/GaP core-shell NWs in ref. [54] for a fixed combination of core and shell diameter. However, the dependence on the shell thickness has not been studied.

Simulation details

The strain energy U of a deformed solid is given by [100]

$$U = \frac{1}{2} \int C_{ijkl}(\mathbf{r})\, \epsilon_{ij}(\mathbf{r})\, \epsilon_{kl}(\mathbf{r})\, \mathrm{d}\mathbf{r} \tag{6.1}$$

where C_{ijkl} is the fourth rank tensor of elastic stiffness constants and ϵ_{ij} are the components of the strain tensor $(i, j, k, l = 1, 2, 3)$. The integration is performed over the entire volume of the solid. A pseudomorphic combination of two materials at a heterointerface can be expressed by an initial strain ϵ^0_{ij}, that does not include rotations and deforms the materials with respect to their bulk lattice constants in order to match the pseudomorphic requirement at the interface. In addition to this initial strain, the system can be free to deform elastically, for example due to free surfaces in a finite nanostructure. This deformation is characterized by a displacement field $\mathbf{u}(\mathbf{r})$, depending on the position $\mathbf{r}$ in the solid. In this case, the total strain tensor in equation (6.1) can be written as [116, 114]

$$\epsilon_{ij}(\mathbf{r}) = \frac{1}{2}\left(\frac{\partial u_i(\mathbf{r})}{\partial x_j} + \frac{\partial u_j(\mathbf{r})}{\partial x_i}\right) + \epsilon^0_{ij}(\mathbf{r}). \tag{6.2}$$

To determine the strain distribution in the solid, the displacement field $\mathbf{u}$ is varied to minimize the strain energy U in equation (6.1). Using the finite element method, this is done by standard numerical algorithms after reduction of the continuous solid to a set of discrete elements [9].

Figure 6.6 shows a view of the core-shell geometry used for the FEM simulation. For all simulations, a NW core with 80 nm diameter between opposite corners and hexagonal cross section has been surrounded by a shell of 10 nm, 20 nm and 35 nm thickness, respectively (cf. also fig. 6.7). To simulate the elastic properties of core and shell, the bulk elastic constants of GaAs and InAs have been transformed into the surface coordinate system obeying the hexagonal symmetry of the NWs by means of a tensor transformation of the fourth rang elasticity tensor [16]. However, the rotation of the cubic directions into the surface coordinate system does not lead to a hexagonal symmetry. Instead, a trigonal symmetry is obtained, corresponding to the two possible twin orientations of the cubic zinc-blende lattice. Following an approach by Martin [86], hexagonal symmetry is obtained by averaging the elastic constants for the two possible twinned zinc-blende orientations. This is a reasonable assumption, as the NWs contain ZB rotational twins. No additional modification of the elastic constants due to the WZ crystal structure was considered (cf. [86]), as the WZ structure is only observed at the top part of the NWs. In addition, growth experiments show that the InAs shell only forms on the ZB part of the GaAs core, leading to the tapered part of the shell towards the top of the NW (cf. figure 6.2(c)).

If we assume a homogeneous shell covering the entire length of the NW, the strain field within the NW will not change along the NW axis apart from the

---

[16] For the sake of convenience, usually the matrix notation for the indices of the tensors C_{ijkl} and ϵ_{ij} is applied, reducing the indices to C_{jk} and ϵ_j with $j, k = 1, ..., 6$. For cubic materials described in a cubic coordinate system with axes parallel to the principal directions of the cube, only the three components C_{11}, C_{12} and C_{44} are non zero. However, transformation to a rotated coordinate system yields more non zero elements (compare [100]).

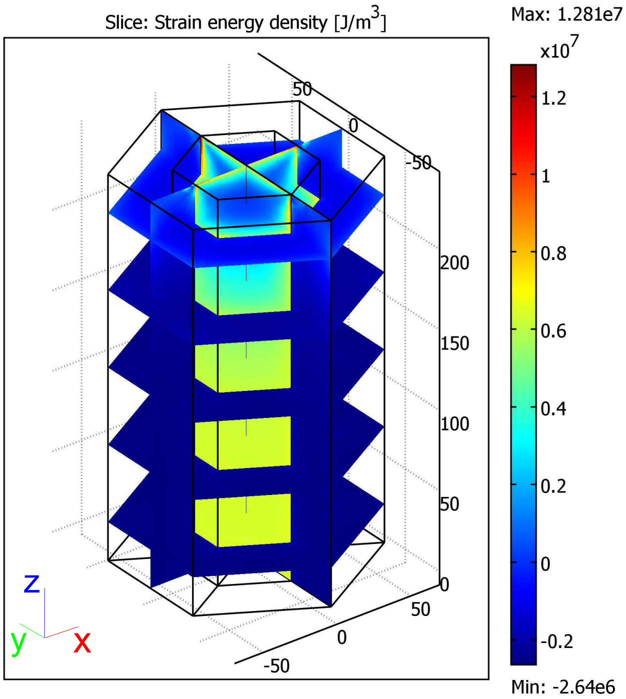

Figure 6.6: 3-dimensional view of a core-shell nanowire geometry (80 nm core diameter, 35 nm shell thickness) used in the FEM simulation. The z- and x-axis of the model correspond to the cubic $[1\,1\,1]^c$ and $[1\,\bar{1}\,0]^c$ directions, respectively. The slices show the strain energy density within the NW, showing the deformation close to the top wire facet. For the simulation, only the steady state in the lower part of the NW is considered.

topmost free surface and the interface region towards the substrate. Neglecting possible changes in these areas, we therefore aim to simulate the displacement field within a cross sectional slice within the NW. In order to achieve this, the top interface of the NW depicted in figure 6.6 was allowed to deform freely within the FEM simulation, whereas the bottom interface was subjected to a roller boundary condition, allowing only displacements in the x-y plane (cf. figure 6.6), but no perpendicular displacements or twists. The latter is used to obtain the static situation assumed in the NW away from it's topmost facet. To be unaffected by deformation effects arising at the top facet of the NW, simulations have been performed for different NW lengths. As a result, the length of the

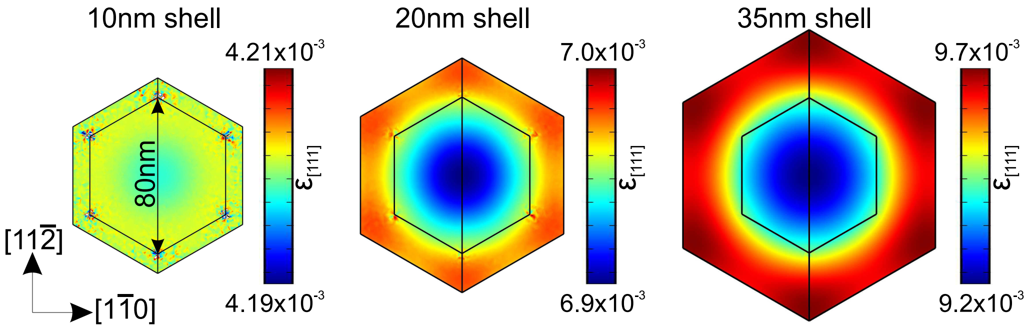

Figure 6.7: Relative displacement $\epsilon_{[111]}$ along the growth direction, resulting from FEM simulations for different shell thicknesses. In all cases, an effective axial mismatch of 1.5% was used for the simulation. Core and shell regions are indicated. In all cases, the displacement in the core shows only small variations. With increasing thickness, the shell relaxes towards the free surface. Note that the strain in the shell is given by $\epsilon_{[111]} - 1.5\%$

NW was chosen to be 4 times its diameter [17], resulting in a steady state of the strain field in a distance of about one times its diameter away from the top facet. Residual axial stress arising at the core-shell interface was simulated by applying an vertical expansion of the shell by means of a temperature increase (representing ϵ_0 in equ. (6.2)). The relative expansion of the shell models the remaining effective mismatch at the heterointerface. Whereas 7.16% expansion corresponds to the (axially) pseudomorphic case, 1% expansion correspond to a plastic relaxation of $R = 1 - (1/7.16) = 86\%$. Here, only initial axial mismatch (resulting in both axial and radial strains) has been considered and no thermal expansion of the shell in the radial direction has been applied. The choice has been motivated by experimental reports, showing that in InAs core/GaAs shell NWs the radial strain release occurs more rapidly than the axial one [69, 113, 70].

In the simulation, the relative expansion of the shell and hence the residual mismatch was varied and the resulting strains were compared with the experiment. Figure 6.7 shows the relative displacement $\epsilon_{[111]}$ in a cross section of the NW 10 nm above the bottom interface, arising from a thermal axial expansion of the shell by 1.5%. In the combination of all measured data points, this value of 1.5% residual strain lead to the best agreement between simulation and data.

---

[17] For better representation, the scheme in figure 6.6 shows a shorter NW with length equal to 3 times its diameter.

In this slice, the steady state of the deformation away from the topmost interface has been reached. Due to the elastic interaction between core and shell, also the core region is tensile strained in all cases. The strain $\epsilon_{[111]}^{core}$ in the core is equal to $\epsilon_{[111]}$ as shown in figure 6.7. At the same time, the expansion of the shell does not reach the desired 1.5% with respect to the initial state. Hence, the shell is compressively strained by $\epsilon_{[111]}^{shell} = \epsilon_{[111]} - 1.5\%$. With increasing shell thickness, the simulations show an increasing strain in the core, together with a more efficient relaxation of the shell towards the free surface. In addition, the strain distribution within both core and shell is comparably homogeneous, showing only small variations in the range of $\pm 0.01 \cdot 10^{-3}$ for 10 nm shell thickness up to $\pm 0.3 \cdot 10^{-3}$ for 35 nm shell thickness, respectively. This small spread in the displacement supports the interpretation of the x-ray data, in which a shift of the entire diffraction signal of the GaAs core has been observed. For a quantitative comparison with the x-ray data, the average strains in the core and shell regions of figure 6.7 have been calculated. This results are plotted as open symbols together with the experimental data in figure 6.5. The general trend observed in the experiment can be well explained without the need of additional plastic relaxation for larger shell thickness and hence explain the observed 'saturation' of the axial relaxation.

Comparing the absolute values of the strain and the general dependence of the strain in core/shell with increasing shell thickness, small deviations are observed between simulation and measurement. Several factors may contribute to this deviations. First, the calculations for each sample have been performed for one selected shell- and core diameter only, but due to the random nature of NW growth, the dimensions of both core and shell will vary among different NWs even for the same growth parameters. Second, only axial stress has been considered (see above), neglecting possible tangential stresses around the NWs perimeter. Finally, bulk elastic constants have been considered for the simulation. However, deviations of the elastic parameters are expected for small dimensions, which holds in particular for the thin InAs shell but also the core diameter of 80 nm. However, no conclusive picture about the changes in elastic properties and their dependence on geometric or size effects can be drawn to date. For example, a systematic *increase* in Young's modulus in ZnO NWs with decreasing diameter below 500 nm has been found and explained by a model in which the NW contains a core and shell-region of larger stiffness due to surface effects, who's contribution increases for smaller diameter [20, 1, 150]. For Si NWs, a *decrease* of Young's modulus for thin diameter is usually observed

[78, 150]. However, the case of GaAs NWs, both an increase [144] as well as a decrease [3] of Young's modulus of GaAs NWs compared to bulk GaAs have been reported.

6.4 Summary

The FEM simulation showed that the observed homogeneous strain in the GaAs cores can indeed be caused by residual axial stress at the core/shell interface. Noteworthy, already thin InAs shells of 10 nm can lead to a significant elastic deformation, showing only small variations within the entire core. Compared to measurements of the axial relaxation by electron diffraction or Moiré patterns in TEM, our x-ray data provide the absolute strains in both core and shell, showing an increasing average relaxation of the shell together with an increasing strain in the core. This observation can be explained by a saturation of the dislocation density at the heterointerface, leading to an effective mismatch of 1.5% between core and shell. First HR-TEM investigations of the initial stage of InAs formation show that the distance between dislocations at the interface is larger than required for complete plastic relaxation, in agreement with this assumption [121]. At present, we speculate that dislocations are formed during the growth of initial InAs islands on the NWs' sidewalls. Here, less dislocations might be sufficient to release the strain energy together with deformations at the free surfaces of the islands. Once the islands coalesce and form a closed film, dislocation nucleation might be hindered and lead to the observed residual strain. Also in planar heteroepitaxy of InAs on GaAs (1 1 1)A, a transition from initially strained islands towards a closed layer including misfit dislocations that release the strain only partially has been reported [147].

In addition, our measurements explain the observed "saturation" of axial relaxation in the shell by TEM methods. Both measurement and simulation show a relative difference in the lattice parameters of core and shell of $\approx 80\%$ compared to the bulk lattice parameters. Due to the elastic interaction, this value does not change considerably even for large shell thickness, although the mean relaxation of the shell reaches a value of 93% (compared to bulk values) for 35 nm thickness.

7 Conclusions

In the present work, x-ray diffraction methods were used to study the growth and structure of different GaAs nanowire systems. Whereas conventional diffraction techniques have been used to study large ensembles of nanowires simultaneously, nanodiffraction techniques allowed to address the unique structure of the probed objects and hence provide information independent from the fluctuations that are usually observed among different nanowires grown on one substrate (e.g. diameters, stacking-faults and arrangement of ZB/WZ segments along the growth axis).

Coherent x-ray diffraction was applied to measure simultaneously the 3-dimensional shape and lattice parameters of GaAs nanowires grown by metal-organic vapor phase epitaxy on GaAs. Using a model-free reconstruction of the diffracting object using phase retrieval algorithms, both real and imaginary part of the NWs' electron densities could be obtained from the diffraction patterns. In the presented study, the method revealed individual differences in the shape of the simultaneously grown nanowires. Whereas in this particular example the differences in shape are also accessible using standard electron microscopy techniques, the x-ray method is generally not restricted to the outer particle's shape, but can also be used to reveal internal variations in chemical composition or strains with a high resolution. In addition to individual differences in the shape, we have observed that due to a high density of zinc-blende rotational twins within the NWs, their lattice parameter deviates systematically from the bulk zinc-blende phase.

In a second example, we have addressed the initial stage in the growth of GaAs NWs on Si (1 1 1) surfaces using a Ga-assisted growth mechanism in molecular beam epitaxy. In this system, the smaller lattice parameter of the silicon compared to the GaAs NWs requires the accommodation of this mismatch during the initial stage of growth. We observed that independent of their diameter, NWs grow with relaxed in-plane lattice parameter on the Si substrate. This lattice parameter accommodation takes place already in the initial stage of growth through the inclusion of misfit dislocations. Remarkably, even for NW diameters as small as 10 nm, growth is not pseudomorphic. Thick nanowires with diameters larger than 100 nm are affected by residual strain at the interface towards the substrate, decaying elastically along the growth direction. These NWs exhibit a rough interface structure, most likely caused by an initial meltback-etching process of the liquid Ga droplet with the Si substrate. Although a high number of dislocations is introduced, the interface roughness prevents full strain release. In contrast, NWs with diameters below 50 nm are free of strain because the smooth interface to the Si substrate allows complete plastic relaxation. This results demonstrate that more effects than the elastic energy have to be taken into account to describe whether NW growth takes place without the introduction of dislocations. All nanowires are found to grow mainly in the cubic zinc-blende structure, although a large abundance of the hexagonal wurtzite phase is found in the beginning of growth. The wurtzite structure has an increased c/a - ratio of 1.649 ± 0.001 compared to 1.633 in the bulk zinc-blende phase. Using diffraction measurements on single NWs, we have determined the wurtzite content and its position along the growth direction for individual NWs, showing that although growth frequently starts in the ZB structure, extended wurtzite segments are formed close to the substrate.

Finally, first measurements of the axial strain and relaxation in GaAs-core / InAs-shell nanowire heterostructures were presented. In this system, we have found a residual stress at the core-shell interface, that can be explained by a saturation of the dislocation density at the core-shell interface during the initial stage of growth, in which InAs islands are formed. This leads to a significant strain in the GaAs core, increasing with the thickness of the InAs shell. Simultaneously, the shell relaxes gradually with increasing thickness.

A Structure factors of zinc-blende and wurtzite materials

To determine the position and intensity of allowed Bragg reflections in reciprocal space, the structure factors F_{hkl} need to be calculated according to

$$F_{hkl} = \sum_n f_n(\mathbf{q}) e^{i\,\mathbf{q}\cdot\mathbf{r}_n}.$$

Here, $\mathbf{q}$ is the diffraction vector of the reciprocal lattice point with indices (h k l). In particular, the structure factors determine the combinations of indices (h k l), for which no reflections can be observed. Here, the expressions for the structure factors of the zinc-blende and wurtzite structures for a reflection (h k l) in their respective coordinate systems are given. For the cubic zinc-blende structure, we need to distinguish between the description in the cubic and hexagonal notation of the surface-coordinate system. The calculations are performed for the GaAs structure. For silicon, the structure factors are obtained by replacing both atomic form factors of Ga and As by Si.

Zinc-blende structure, cubic coordinate system Commonly, the zinc-blende structure is described in a cubic coordinate system with the atoms located at the following relative positions in the cubic unit cell (cf. figure 2.3):

$$\begin{aligned} &As : (0,0,0) \quad \left(\frac{1}{2},\frac{1}{2},0\right) \quad \left(\frac{1}{2},0,\frac{1}{2}\right) \quad \left(0,\frac{1}{2},\frac{1}{2}\right) \\ &Ga : \left(\frac{1}{4},\frac{1}{4},\frac{1}{4}\right) \quad \left(\frac{3}{4},\frac{3}{4},\frac{1}{4}\right) \quad \left(\frac{3}{4},\frac{1}{4},\frac{3}{4}\right) \quad \left(\frac{1}{4},\frac{3}{4},\frac{3}{4}\right) \end{aligned}$$

Using this relative coordinates, the structure factor of a reflection with Miller indices (h k l) can be calculated according to equation (3.12)

$$F_{hkl}^{ZB,c} = \left(1 + e^{i\pi(h+k)} + e^{i\pi(h+l)} + e^{i\pi(k+l)}\right)\left(f_{\mathrm{As}} + f_{\mathrm{Ga}} e^{i(\pi/2)(h+k+l)}\right) \qquad \text{(A.1)}$$

The first term equals 4, whenever all indices are even or all indices are odd. Together with the second term, we obtain the relation

$$F_{hkl}^{ZB,c} = 4 \cdot \begin{cases} f_{\mathrm{As}}(q) + f_{\mathrm{Ga}}(q) & h,k,l \text{ even and } h+k+l = 4n; n \in \mathbb{Z} \\ f_{\mathrm{As}}(q) - f_{\mathrm{Ga}}(q) & h,k,l \text{ even and } h+k+l \neq 4n; n \in \mathbb{Z} \\ f_{\mathrm{As}}(q) \pm i\, f_{\mathrm{Ga}}(q) & h,k,l \text{ odd} \\ 0 & \text{otherwise} \end{cases} \tag{A.2}$$

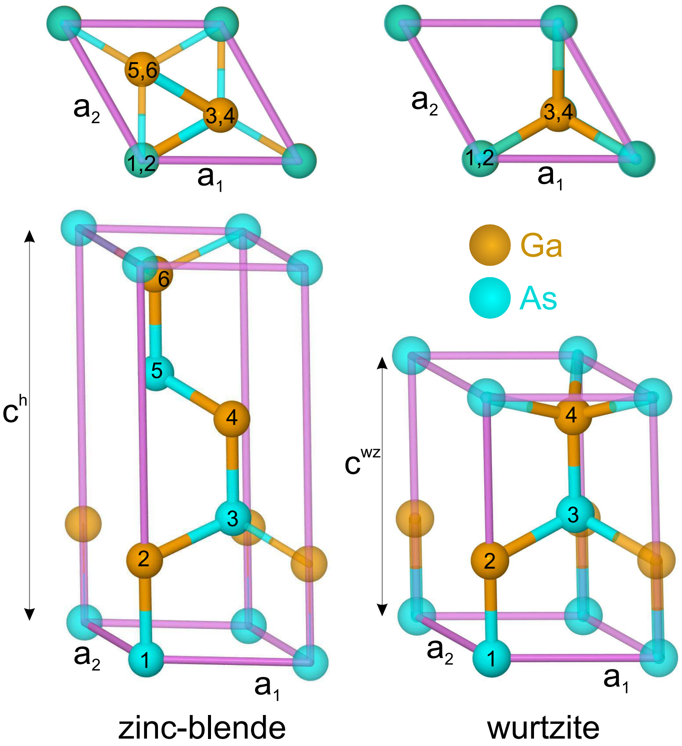

Figure A.1: Unit cells of the zinc-blende (left) and wurtzite (right) crystal structures in the hexagonal surface-coordinate system. The upper row shows a top view along the **c** directions. For the ZB structure, 6 atoms (bold) are found in the unit cell, whereas 4 atoms are present in the WZ case. Note that the bonds of the second Ga atom (#4) are rotated by 30° with respect to each other.

Zinc-blende structure, surface coordinate system As discussed above, for [1 1 1] oriented materials the zinc-blende structure can also be described in a hexagonal surface coordinate system. Figure A.1(left) shows a possible choice of the hexagonal unit cell of this ZB structure, containing six atoms with positions

$$\begin{aligned} As: \mathbf{r}_1 &= (0,0,0) \quad \mathbf{r}_3 = \left(\frac{2}{3},\frac{1}{3},\frac{1}{3}\right) \quad \mathbf{r}_5 = \left(\frac{1}{3},\frac{2}{3},\frac{2}{3}\right) \\ Ga: \mathbf{r}_2 &= \left(0,0,\frac{1}{4}\right) \quad \mathbf{r}_4 = \left(\frac{2}{3},\frac{1}{3},\frac{1}{3}+\frac{1}{4}\right) \quad \mathbf{r}_6 = \left(\frac{1}{3},\frac{2}{3},\frac{2}{3}+\frac{1}{4}\right). \end{aligned}$$

In the hexagonal reciprocal space coordinates we obtain the structure factor

$$\begin{aligned} F_{hkl}^{ZB,h} &= \left(1 + e^{i(2\pi/3)(2h+k+l)} + e^{i(2\pi/3)(h+2k+2l)}\right)\left(f_{\mathrm{As}} + f_{\mathrm{Ga}} e^{i(\pi/2)l}\right) && \text{(A.3)} \\ &= \left(1 + e^{i(2\pi/3)(2h+k+l)} + e^{i2(2\pi/3)(2h+k+l)}\right)\left(f_{\mathrm{As}} + f_{\mathrm{Ga}} e^{i(\pi/2)l}\right) && \text{(A.4)} \end{aligned}$$

The first term equals 3, whenever $2h + k + l = 3n \; ; \; n \in \mathbb{Z}$, and we obtain the result

$$F_{hkl}^{ZB,h} = 3 \cdot \begin{cases} f_{\mathrm{As}}(q) + f_{\mathrm{Ga}}(q) & 2h+k+l = 3n \quad ; l = 0, 4, 8 ... ; n \in \mathbb{Z} \\ f_{\mathrm{As}}(q) - f_{\mathrm{Ga}}(q) & 2h+k+l = 3n \quad ; l = 2, 6, 10 ... ; n \in \mathbb{Z} \\ f_{\mathrm{As}}(q) \pm i f_{\mathrm{Ga}}(q) & 2h+k+l = 3n \quad ; l \,\mathrm{odd}; n \in \mathbb{Z} \\ 0 & \text{otherwise} \end{cases} \tag{A.5}$$

It is worth to realize that the structure factors in equations (A.2) and (A.5) do not give the same result even for the same reflection, expressed in the different coordinate systems, because the size of the chosen unit cell is different for both cases. In addition, a ZB-twin leads to an exchange of the first two coordinates of atoms #(3,4) and #(5,6) in fig. A.1, corresponding to a change in the condition for allowed reflections according to

$$2h + k + l = 3n \quad \xrightarrow{\text{twin}} \quad h + 2k + l = 3n \quad n \in \mathbb{Z} \tag{A.6}$$

Wurtzite structure Finally, the unit-cell of the hexagonal wurtzite structure contains four atoms at the relative coordinates (fig. A.1(right))

$$\begin{aligned} &As : \mathbf{r}_1 = (0,0,0) \quad \mathbf{r}_3 = \left(\frac{2}{3}, \frac{1}{3}, \frac{1}{2}\right) \\ &Ga : \mathbf{r}_2 = \left(0, 0, \frac{3}{8}\right) \quad \mathbf{r}_4 = \left(\frac{2}{3}, \frac{1}{3}, \frac{1}{2} + \frac{3}{8}\right) \end{aligned}$$

leading to the structure factor

$$F_{hkl}^{WZ} = \left(1 + e^{i(2\pi/3)(2h+k)} e^{i\pi l}\right)\left(f_{\mathrm{As}} + f_{\mathrm{Ga}} e^{i(3\pi/8)l}\right). \tag{A.7}$$

The first term vanishes, whenever l is odd and $2h + k = 3n; n \in \mathbb{Z}$.

In the wurtzite structure, the c axis is by a fraction of 2/3 shorter than the native c axis of the zinc-blende structure in figure A.1. Consequently, the reciprocal lattice vector $\mathbf{b}_3^{WZ}$ of the WZ structure is 3/2 longer than $\mathbf{b}_3^{ZB,h}$ of the ZB structure in the surface coordinates. Hence, the reciprocal lattice points of the WZ structure are found at multiples of $1.5\,l$ in the surface coordinate system. This is sketched in figure 3.6.

B Resolution effects in reciprocal space maps

Meanwhile, many diffraction experiments are conducted using a 1- or 2- dimensional pixel detector to collect the diffracted intensity. The intrinsic angular resolution of the detector system therefore allows to cover an extended slice in reciprocal space within a single acquisition. A complete reciprocal space map can then be collected within a single scan, e.g. by rocking the sample in small steps $\Delta\omega$ around a desired Bragg reflection (cf. section 3.4). Figure B.2 depicts this situation in the general case of a Bragg reflection. With respect to the probed lattice planes, the scattering vector $\mathbf{q}$ can be decomposed into components $\mathbf{q}_{rad}$ and $\mathbf{q}_{tang}$ parallel and perpendicular to the reciprocal lattice vector, respectively. In the case of a symmetric diffraction experiment, this components correspond to q_z and q_x. In the case of an asymmetric diffraction experiment, both lattice plane and diffraction vector are inclined by the angle Φ with respect to the surface. The angular resolution of the detector $\Delta 2\theta$ leads to a resolution $\Delta q_{2\theta}$ within each slice of data taken in reciprocal space (fig. B.2 (a)). In addition, the subsequent rotation of the lattice planes by the angle $\Delta\omega$ leads to a translation of the detection plane by the components Δq_{rad} and Δq_{tang}, leading to a triangular shaped region in which no data is acquired (fig. B.2 (b)). In a usual diffraction experiment considered here, $\Delta\omega$ is small and much smaller than the Bragg angle θ_B. In this case, the translations can be calculated as

$$\Delta q_{2\theta} = k \sin(\Delta 2\theta) \tag{B.1}$$

$$\Delta q_{rad} = 2k \cos\theta_B \, \sin\Delta\omega \tag{B.2}$$

$$\Delta q_{tang} = 2k \sin\theta_B \, \sin\Delta\omega \tag{B.3}$$

Note that depending on the chosen step size $\Delta\omega$, the side lengths $\Delta q_{rad/tang}$ may easily exceed the 'intrinsic' resolution $\Delta q_{2\theta}$. Depending on the intensity features to be probed in reciprocal space, appropriate rotations need to be chosen to achieve sufficient resolution.

In addition to the limited resolution in a reciprocal space map, the use of a focussed x-ray beam in nanodiffraction experiments leads to a systematic broadening of Bragg reflections due to the convolution with the beam divergence. In

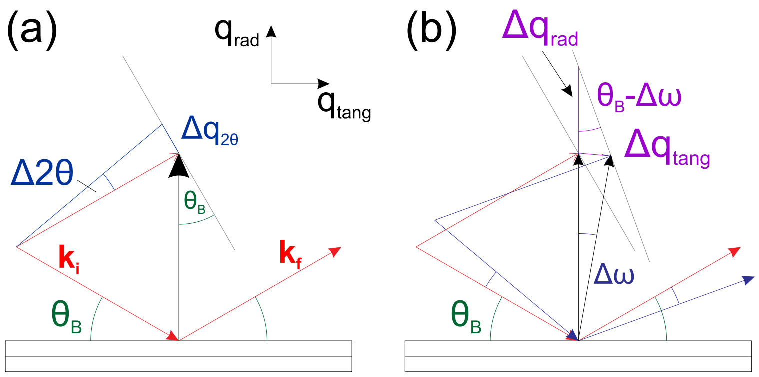

Figure B.1: Definition of the different resolution effects during the acquisition of a reciprocal space map. (a) At any position, the detector covers a slice in reciprocal space. The angular acceptance $\Delta 2\theta$ of the detector determines a resolution $\Delta q_{2\theta}$ along the direction covered by the detector. (b) To obtain a RSM, usually the sample is rocked in steps $\Delta\omega$ around a Bragg position. This results in a triangular shaped area with nearly perpendicular sides Δq_{rad} and Δq_{tang}, inside of which no data is collected.

case of the focussing using a Fresnel zone plate, the incident x-ray beam is not parallel, but has a finite divergence in a cylindrical symmetry around the optical axis. Figure B.2 (a) shows a side-view of the diffraction geometry and angles considered. With respect to the optical axis, the incidence angles on the sample position vary in a range of $\pm\Delta\alpha_i$, determined by the focal distance and the diameter of the FZP. Besides this change in α_i, also the in-plane-angle of the impinging x-rays varies in a range $\pm\Delta\mu$ (b).

To simulate the diffracted intensity within this setup, first the aperture of the FZP is divided into volume elements at positions $\mathbf{r}'$ as indicated in figure B.2 (c). As approximation we assume that each volume element is illuminated by the same incident intensity and focused with equal efficiency onto the sample position, illuminating the sample with angles $\alpha_i^0+\Delta\alpha_i(\mathbf{r}')$ and $\mu^0+\Delta\mu(\mathbf{r}')$ depending on the position $\mathbf{r}'$ itself. Figure B.2(c) shows a plot of the total divergence angle with respect to the optical axis ψ, given by $\cos\psi = \cos\Delta\alpha_i \cdot \cos\Delta\mu = r'/f$ along the FZP. For simulation, a FZP with 190 μm diameter, 100 nm outermost zone width and focal distance f=138 mm at 9keV photon energy have been considered, as used in the measurement of a bulk Bragg reflection. Note that due to the central beamstop in front of the FZP (diameter 50 μm), the central components with small total divergence are not present in the x-ray beam.

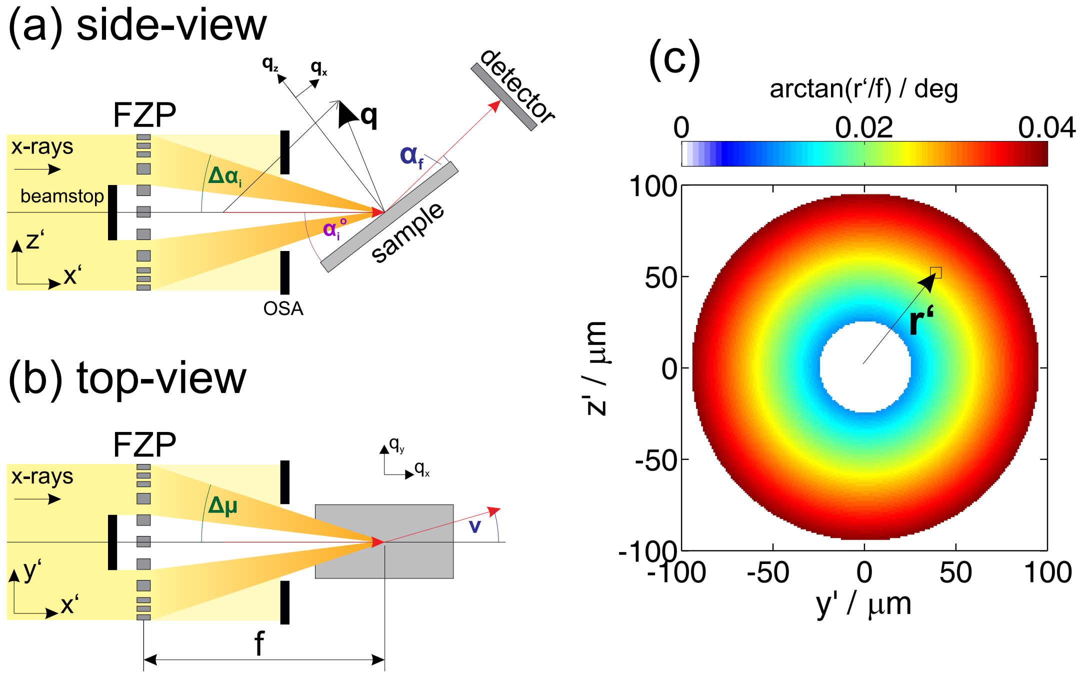

Figure B.2: Definition of angles for a highly focussed x-ray beam behind a zone plate. The zone plate introduces a divergence with rotational symmetry around the optical axis with components $\Delta\alpha_i$ along the incidence angle (a) as well as $\Delta\mu$ along the perpendicular direction (b). For simulation purpose, the FZP is divided into volume elements at positions $\mathbf{r}'$ (c). Colorscale in (c) shows the rotational symmetry of the total divergence r'/f, resulting in changes of the incidence angle of up to $\approx 0.4°$ at the used experimental conditions (see text).

For each angular position α_i^0, the diffracted amplitude in a single pixel of the detector, determining the angles α_f and ν, can be expressed as the integrated amplitude over all partially scattered waves passing the FZP, considering that according to equations (3.26), the components of the scattering vector $\mathbf{q}$ become a function of $\mathbf{r}'$ due to the changing incidence angles

$$A(\alpha_i^0, \alpha_f, \nu) = \int\limits_{\mathbf{r}'} A_0(q_x(\mathbf{r}'), q_y(\mathbf{r}'), q_z(\mathbf{r}'))\, \mathrm{d}\mathbf{r}' \tag{B.4}$$

Here, $A_0(\mathbf{q})$ represents the diffracted amplitude given by equation (3.8). To illustrate the influence of the divergence on the measured intensity distribution, the broadening of a bulk Si reflection has been simulated and compared with experimentally observed data. Figure B.3(a) shows a modeled intensity distribution of the silicon $(3\,3\,1)^c$ reflection in the in the $q_x - q_z$ plane in case of illumination with a parallel beam. The bulk Bragg peak was modeled by a superposition of Lorentzian profiles, taking into account the broadening along q_z due to the crystal truncation rod. In addition, the data was integrated along the detector angle ν, as usually done in the experiments as well. Obviously, this model is only a rough approximation for simulation purposes, neglecting e.g. diffuse scattering. Figure B.3(b) shows the simulated intensity distribution taking into account the divergence introduced by the FZP. As visible, the large divergence causes significant broadening of the Bragg reflection in reciprocal space. For comparison with the experiment, figure B.3(c) presents the measured intensity distribution around the same Bragg reflection, showing good agreement with the simulated broadening. Both simulation and experiment

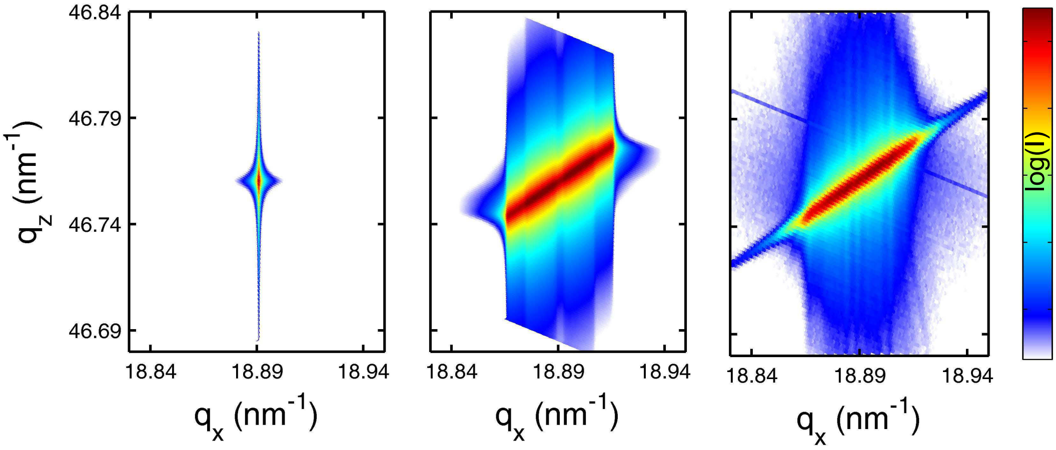

Figure B.3: (a) Model of the $(331)^c$ Bragg peak of the substrate, realized by the superposition of Lorentzian functions. (b) Simulated intensity distribution measured with the divergent x-ray beam produced by a Fresnel zone plate. The plot shows the intensity distribution in the q_x, q_z plane, and data was integrated along the q_y direction (angle ν) on the detector. (c) Measured intensity distribution around a Si $(331)^c$ reflection, showing good agreement with the simulated resolution function.

have been performed at 9keV photon energy in a grazing exit configuration. For a better comparison, figure B.4 shows integrated line profiles along the q_z (top) and q_x (bottom) directions for both experiment and simulation. Good agreement in terms of FWHM and peak profiles is observed. Note that the profiles show a minimum in the center of the peak, caused by the missing part of the x-ray beam blocked by the central beam stop. Based on the measured data, the Bragg peak extents over a range of $\delta q_z \approx 0.026\text{nm}^{-1}$ and $\delta q_x \approx 0.039\text{nm}^{-1}$ in reciprocal space. This spread can be reduced if only a part of the FZP is illuminated using a set of slits, on the expense of total intensity in the focal spot and an increased focal spot size [88].

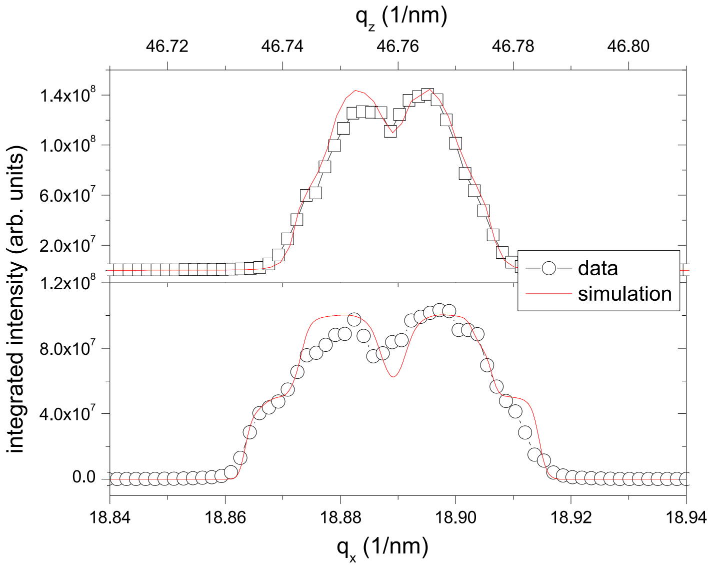

Figure B.4: Comparison of integrated intensity profiles along q_z (top) and q_x (bottom) directions of the simulated and measured intensity distribution in fig. B.3.

C Surface sensitive diffraction techniques

(adapted from paper [IX])

The symmetric and asymmetric diffraction geometries can not be used to access Bragg reflections of planes perpendicular to the surface, e.g. reflections (h k i 0) in the surface coordinate system. However, this Bragg reflections are accessible in a *grazing incidence diffraction* (GID) geometry, making use of the refraction effects of an x-ray wave at small incidence angles, enhancing the signal from surface layers while, at the same time, suppressing strong scattering signals from the substrate. This surface sensitivity is based on the fact that the index of refraction of x-rays for condensed matter is smaller than one, and can be expressed according to

$$n = 1 - \delta + i\beta \tag{C.1}$$

with parameters δ and β describing the refraction and absorption of the x-ray wave, respectively:

$$\delta = \lambda^2 \frac{r_0 N_a \rho_m}{2\pi A}(f_0 + f') \tag{C.2}$$

$$\beta = \lambda^2 \frac{r_0 N_a \rho_m}{2\pi A} f'' = \frac{\lambda\mu}{4\pi} \tag{C.3}$$

where λ is the wavelength of the x-rays, N_a is Avogadro's number, r_0 the classical electron radius, $\rho_{m,e}$ are mass- and electron-density, respectively and A the molar atomic mass. f_0, f', f'' and μ are the atomic scattering factor, the real- and imaginary part of it's dispersion correction (depending again of λ) and the linear absorption coefficient.

Snell's law relates the angles of an incidence α_i and transmitted x-ray wave α' with respect to the surface according to $\cos\alpha_i = n \cos\alpha'$, and thus a critical angle for total external reflection exists, eq. (C.4).

$$\alpha_c = \sqrt{2\delta} = \frac{\sqrt{4\pi\rho_e r_0}}{k} \tag{C.4}$$

For x-rays impinging at angles below this critical angle, an evanescent wave is created below the surface and propagates parallel to it. Its amplitude is maximum at the surface and is attenuated exponentially towards the bulk, with a typical $1/e$ penetration depth of some tens of nanometers, depending on the incident angle and the energy of the x-ray beam. If scattering takes place inside the surface layer and the x-ray beam is observed under a grazing exit angle, the subsequent absorption and refraction of both incident and exit beams contribute to the total *scattering depth* Λ, which can be expressed as [37]

$$\Lambda = \frac{1}{Im(q'_\perp)} = \frac{\lambda}{4\pi(B_i + B_f)} \tag{C.5}$$

where $q'_\perp$ is the vertical momentum transfer inside the material, and

$$B_{i,f} = 2^{-1/2}\{(2\delta - sin^2\alpha_{i,f}) - [(sin^2\alpha_{i,f} - 2\delta)^2 + 4\beta^2]^{1/2}\}^{1/2} \tag{C.6}$$

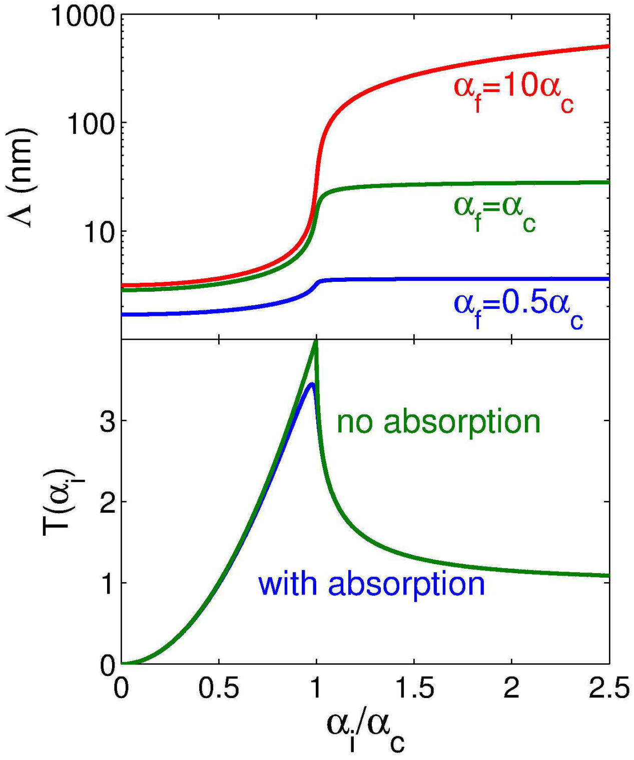

Figure C.1: (a) X-ray penetration depth and (b) X-ray transmission coefficient as function of $\alpha_{i,f}$. Values calculated for a silicon substrate and a x-ray energy of 8keV (adapted from [37]).

Figure C.1(a) shows how the scattering depth varies as a function of the incident angle at three different values of the exit angle α_f. For α_i below the critical angle the probed depth can be of the order of 10Å, then it rapidly increases across the critical angle up to several thousands Å, depending on the actual value of α_f, the absorption by the material and the x-ray energy. The remarkable fact is that adjusting the value of the angles $\alpha_{i,f}$ in an appropriate way, allows a fine tuning of the probed depth to achieve a depth resolution of few Å.

The transmission coefficients T of the x-rays at small angles is determined by the material's refraction index n (see figure C.1(b)). In particular, the transmission coefficient is highest at the critical angle (T=4 with no absorption), which means that the scattering signal from the surface is maximized when $\alpha_{i,f} = \alpha_c$ (cf. Fig. C.1(b)). Consequently, the intensity of the scattering from the surfaces layers is enhanced with respect to the bulk part.

In the grazing incidence configuration, the evanescent x-ray wave can still be diffracted from lattice planes which are strictly perpendicular to the substrate's surface and leave the crystal again under shallow exit angle conditions. This diffraction geometry is denoted as *grazing incidence diffraction* (GID), and schematically illustrated in figure C.2.

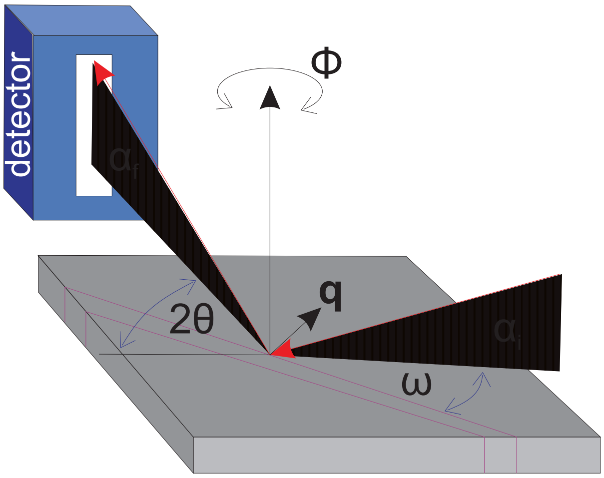

Figure C.2: Sketch of the GID geometry. Incident and exit-angles are small and Bragg's law is fulfilled on lattice planes perpendicular to the surface. Usually, a linear sensitive detector is placed perpendicular to the sample surface to record the intensity distribution along the exit angle.

Here, the incident x-ray beam, with wave-vector $\mathbf{k}_i$, impinges on the surface at a glancing angle α_i, close to the material's critical angle α_c. The out-coming x-ray beam with the wave-vector $\mathbf{k}_f$ is scattered under the angle 2θ with respect to the forward direction and is usually collected by a linear position detector (PSD) or a 2dimensional detector (e.g. CCD or pixel-detector) in a direction forming an exit angle α_f, creating a momentum transfer $\mathbf{q} = \mathbf{k}_f - \mathbf{k}_i$. The momentum transfer measured in GID geometry is often decomposed in a component parallel $\mathbf{q}_{||}$ and perpendicular $\mathbf{q}_{\perp}$ to the surface: $\mathbf{q} = \mathbf{q}_{||} + \mathbf{q}_{\perp}$. At a given wavelength λ, the angle 2θ determines the the value of $q_{||} = \frac{4\pi}{\lambda}\sin(2\theta/2)$. The angles $\alpha_{i,f}$ determine the perpendicular component and, therefore, the scattering depth Λ according to equation (C.5). As the value of both $\alpha_{i,f}$ is small, $\mathbf{q} \approx \mathbf{q}_{||}$ holds, i.e. the probed momentum transfer lies in the surface plane.

Bibliography

[1] R. Agrawal, B. Peng, E. E. Gdoutos, and H. D. Espinosa, *Elasticity size effects in ZnO nanowires – a combined experimental-computational approach*, Nano Letters **8** (2008), 3668.

[2] M. Akabori, J. Takeda, J. Motohisa, and T. Fukui, *InGaAs nano-pillar array formation on partially masked InP(111)B by selective area metal-organic vapour phase epitaxial growth for two-dimensional photonic crystal application*, Nanotechnology **14** (2003), 1071.

[3] P. Alekseev, M. Dunaevskii, A. Stovpyaga, M.I. Lepsa, and A. Titkov, *Measurement of Young's modulus of GaAs nanowires growing obliquely on a substrate*, Semiconductors **46** (2012), 641.

[4] J. E. Allen, E. R. Hemesath, D. E. Perea, J. L. Lensch-Falk, Z.Y. Li, F. Yin, M. H. Gass, P. Wang, A. L. Bleloch, R. E. Palmer, and L. J. Lauhon, *High-resolution detection of Au catalyst atoms in Si nanowires*, Nature Nanotechnology **3** (2008), 168.

[5] Jens Als-Nielsen, *Elements of modern X-ray physics*, Wiley, New York, (2001), ISBN: 0471498580.

[6] André Authier, *Dynamical theory of x-ray diffraction*, Oxford University Press, New York, (2004), ISBN: 9780198528920.

[7] M. Barchuk, V. Holý, D. Kriegner, J. Stangl, S. Schwaiger, and F. Scholz, *Diffuse x-ray scattering from stacking faults in a-plane GaN epitaxial layers*, Physical Review B **84** (2011), 094113.

[8] C. J. Barrelet, Y. Wu, D. C. Bell, and C. M. Lieber, *Synthesis of CdS and ZnS nanowires using Single-source molecular precursors*, Journal of the American Chemical Society **125** (2003), 11498.

[9] Klaus Jürgen Bathe, *Finite element procedures*, Prentice Hall, Englewood Cliffs, N.J, (1996), ISBN: 0133014584.

[10] M. T. Bjork, B. J. Ohlsson, T. Sass, A. I. Persson, C. Thelander, M. H. Magnusson, K. Deppert, L. R. Wallenberg, and L. Samuelson, *One-dimensional heterostructures in semiconductor nanowhiskers*, Applied Physics Letters **80** (2002), 1058.

[11] M. T. Bjork, B. J. Ohlsson, C. Thelander, A. I. Persson, K. Deppert, L. R. Wallenberg, and L. Samuelson, *Nanowire resonant tunneling diodes*, Applied Physics Letters **81** (2002), 4458.

[12] Y. B. Bolkhovityanov and O. P. Pchelyakov, *GaAs epitaxy on Si substrates: modern status of research and engineering*, Physics-Uspekhi **51** (2008), 437.

[13] M. Borgström, K. Deppert, L. Samuelson, and W. Seifert, *Size- and shape-controlled GaAs nano-whiskers grown by MOVPE: a growth study*, Journal Of Crystal Growth **260** (2004), 18.

[14] S. Breuer, M. Hilse, A. Trampert, L. Geelhaar, and H. Riechert, *Vapor-liquid-solid nucleation of GaAs on Si(111): Growth evolution from traces to nanowires*, Physical Review B **82** (2010), 075406.

[15] S. Breuer, C. Pfüller, T. Flissikowski, O. Brandt, H. T. Grahn, L. Geelhaar, and H. Riechert, *Suitability of Au- and self-assisted GaAs nanowires for optoelectronic applications*, Nano Letters **11** (2011), 1276.

[16] Steffen Breuer, *Molecular beam epitaxy of GaAs nanowires and their suitability for optoelectronic applications - comparing Au- and self-assisted growth methods*, Ph.D. thesis, (2012), Humboldt-Universität zu Berlin, Mathematisch-Naturwissenschaftliche Fakultät I.

[17] V. Chamard, J. Stangl, G. Carbone, A. Diaz, G. Chen, C. Alfonso, C. Mocuta, and T. H. Metzger, *Three-dimensional x-ray Fourier transform holography: The Bragg case*, Physical Review Letters **104** (2010), 165501.

[18] V. Chamard, J. Stangl, S. Labat, B. Mandl, R. T. Lechner, and T. H. Metzger, *Evidence of stacking-fault distribution along an InAs nanowire using micro-focused coherent x-ray diffraction*, Journal Of Applied Crystallography **41** (2008), 272.

[19] H. N. Chapman, P. Fromme, A. Barty, T. A. White, R. A. Kirian, A. Aquila, M. S. Hunter, J. Schulz, D. P. DePonte, and U. et al. Weierstall, *Femtosecond X-ray protein nanocrystallography*, Nature **470** (2011), 73.

[20] C. Q. Chen, Y. Shi, Y. S. Zhang, J. Zhu, and Y. J. Yan, *Size dependence of Young's modulus in ZnO nanowires*, Physical Review Letters **96** (2006), 075505.

[21] J. W. Chen and A. G. Milnes, *Energy levels in Silicon*, Annual Review of Materials Science **10** (1980), 157.

[22] G. E. Cirlin, V. G. Dubrovskii, Yu B. Samsonenko, A. D. Bouravleuv, K. Durose, Y. Y. Proskuryakov, B. Mendes, L. Bowen, M. A. Kaliteevski, R. A. Abram, and Dagou Zeze, *Self-catalyzed, pure zincblende GaAs nanowires grown on Si(111) by molecular beam epitaxy*, Physical Review B **82** (2010), 035302.

[23] G. E. Cirlin, V. G. Dubrovskii, I. P. Soshnikov, N. V. Sibirev, Yu B. Samsonenko, A. D. Bouravleuv, J. C. Harmand, and F. Glas, *Critical diameters and temperature domains for MBE growth of III-V nanowires on lattice mismatched substrates*, physica status solidi (RRL) **3** (2009), 112.

[24] C. Colombo, D. Spirkoska, M. Frimmer, G. Abstreiter, and A. F. I. Morral, *Ga-assisted catalyst-free growth mechanism of GaAs nanowires by molecular beam epitaxy*, Physical Review B **77** (2008), 155326.

[25] COMSOL Multiphysics, `www.comsol.com`.

[26] Y. Cui, Z. Zhong, D. Wang, W. U. Wang, and C. M. Lieber, *High performance Silicon nanowire field effect transistors*, Nano Letters **3** (2003), 149.

[27] A. Dadgar, M. Poschenrieder, J. Bläsing, O. Contreras, F. Bertram, T. Riemann, A. Reiher, M. Kunze, I. Daumiller, A. Krtschil, A. Diez, A. Kaluza, A. Modlich, M. Kamp, J. Christen, F. A. Ponce, E. Kohn, and A. Krost, *MOVPE growth of GaN on Si(111) substrates*, Journal Of Crystal Growth **248** (2003), 556.

[28] A. Davydok, S. Breuer, A. Biermanns, L. Geelhaar, and U. Pietsch, *Lattice parameter accommodation between GaAs(111) nanowires and Si (111) substrate after growth via Au-assisted molecular beam epitaxy*, Nanoscale Research Letters **7** (2012), 109.

[29] A. De and C. E. Pryor, *Predicted band structures of III-V semiconductors in the wurtzite phase*, Physical Review B **81** (2010), 155210.

[30] A. Diaz, V. Chamard, C. Mocuta, R. Magalhaes Paniago, J. Stangl, D. Carbone, T. H. Metzger, and G. Bauer, *Imaging the displacement field within epitaxial nanostructures by coherent diffraction: a feasibility study*, New Journal of Physics **12** (2010), 035006.

[31] A. Diaz, C. Mocuta, J. Stangl, M. Keplinger, T. Weitkamp, F. Pfeiffer, C. David, T. H. Metzger, and G. Bauer, *Coherence and wavefront characterization of Si-(111) monochromators using double-grating interferometry*, Journal of Synchrotron Radiation **17** (2010), 299.

[32] A. Diaz, C. Mocuta, J. Stangl, B. Mandl, C. David, J. Vila-Comamala, V. Chamard, T. H. Metzger, and G. Bauer, *Coherent diffraction imaging of a single epitaxial InAs nanowire using a focused x-ray beam*, Physical Review B **79** (2009), 125324.

[33] K. A. Dick, J. Bolinsson, B. M. Borg, and J. Johansson, *Controlling the abruptness of axial heterojunctions in III/V nanowires: Beyond the reservoir effect*, Nano Letters **12** (2012), 3200.

[34] K. A. Dick, P. Caroff, J. Bolinsson, M. E. Messing, J. Johansson, K. Deppert, L. R. Wallenberg, and L. Samuelson, *Control of III-V nanowire crystal structure by growth parameter tuning*, Semiconductor Science and Technology **25** (2010), 24009.

[35] K. A. Dick, K. Deppert, M. W. Larsson, T. Martensson, W. Seifert, L. R. Wallenberg, and L. Samuelson, *Synthesis of branched 'nanotrees' by controlled seeding of multiple branching events*, Nature Materials **3** (2004), 380.

[36] K. A. Dick, S. Kodambaka, M. C. Reuter, K. Deppert, L. Samuelson, W. Seifert, L. R. Wallenberg, and F. M. Ross, *The morphology of axial and branched nanowire heterostructures*, Nano Letters **7** (2007), 1817.

[37] Helmut Dosch, *Critical phenomena at surfaces and interfaces : evanescent x-ray and neutron scattering*, Springer-Verlag, Berlin, (1992), ISBN: 3540545344.

[38] V. G. Dubrovskii, N. V. Sibirev, J. C. Harmand, and F. Glas, *Growth kinetics and crystal structure of semiconductor nanowires*, Physical Review B **78** (2008), 235301.

[39] E. Ertekin, P. A. Greaney, D. C. Chrzan, and T. D. Sands, *Equilibrium limits of coherency in strained nanowire heterostructures*, Journal of Applied Physics **97** (2005), 114325.

[40] J. Eymery, V. Favre-Nicolin, L. Froberg, and L. Samuelson, *X-ray measurements of the strain and shape of dielectric/metallic wrap-gated InAs nanowires*, Applied Physics Letters **94** (2009), 131911.

[41] J. Eymery, F. Rieutord, V. Favre-Nicolin, O. Robach, Y. M. Niquet, L. Fröberg, T. Mårtensson, and L. Samuelson, *Strain and shape of epitaxial InAs/InP nanowire superlattice measured by grazing incidence x-ray techniques*, Nano Letters **7** (2007), 2596.

[42] V. Favre-Nicolin, J. Eymery, R. Koester, and P. Gentile, *Coherent-diffraction imaging of single nanowires of diameter 95 nanometers*, Physical Review B **79** (2009), 195401.

[43] V. Favre-Nicolin, F. Mastropietro, J. Eymery, D. Camacho, Y. M. Niquet, B. M. Borg, M. E. Messing, L. E. Wernersson, R. E. Algra, E. P. A. M. Bakkers, T. H. Metzger, R. Harder, and I. K. Robinson, *Analysis of strain and stacking faults in single nanowires using Bragg coherent diffraction imaging*, New Journal of Physics **12** (2010), 035013.

[44] R. Feidenhans'l, *Surface structure determination by x-ray diffraction*, Surface Science Reports **10** (1989), 105.

[45] J. R. Fienup, *Phase retrieval algorithms: a comparison*, Applied Optics **21** (1982), 2758.

[46] A. Fontcuberta i Morral, C. Colombo, G. Abstreiter, J. Arbiol, and J. R. Morante, *Nucleation mechanism of gallium-assisted molecular beam epitaxy growth of gallium arsenide nanowires*, Applied Physics Letters **92** (2008), 063112.

[47] D. Gabor, G. W. Stroke, D. Brumm, A. Funkhouser, and A. Labeyrie, *Reconstruction of phase objects by holography*, Nature **208** (1965), 1159.

[48] E. Garnett and P. Yang, *Light trapping in silicon nanowire solar cells*, Nano Letters **10** (2010), 1082.

[49] R. W. Gerchberg and W. O. Saxton, Optik (Jena) **35** (1972), 235.

[50] F. Glas, *Critical dimensions for the plastic relaxation of strained axial heterostructures in free-standing nanowires*, Physical Review B **74** (2006), 121302(R).

[51] F. Glas, J. C. Harmand, and G. Patriarche, *Why does wurtzite form in nanowires of III-V zinc blende semiconductors?*, Physical Review Letters **99** (2007), 146101.

[52] P. Godard, G. Carbone, M. Allain, F. Mastropietro, G. Chen, L. Capello, A. Diaz, T. H. Metzger, J. Stangl, and V. Chamard, *Three-dimensional high-resolution quantitative microscopy of extended crystals*, Nature Communications **2** (2011), 568.

[53] I. A. Goldthorpe, A. F. Marshall, and P. C. McIntyre, *Synthesis and strain relaxation of Ge-core/Si-shell nanowire arrays*, Nano Letters **8** (2008), 4081.

[54] J. Grönqvist, N. Sondergaard, F. Boxberg, T. Guhr, S. Åberg, and H. Q. Xu, *Strain in semiconductor core-shell nanowires*, Journal of Applied Physics **106** (2009), 053508.

[55] M. S. Gudiksen, L. J. Lauhon, J. Wang, D. C. Smith, and C. M. Lieber, *Growth of nanowire superlattice structures for nanoscale photonics and electronics*, Nature **415** (2002), 617.

[56] T. Hamano, H. Hirayama, and Y. Aoyagi, *New technique for fabrication of two-dimensional photonic bandgap crystals by selective epitaxy*, Japanese Journal of Applied Physics **36** (1997), L286.

[57] M. Heiss, S. Conesa-Boj, J. Ren, H. H. Tseng, A. Gali, A. Rudolph, E. Uccelli, F. Peiró, J. R. Morante, D. Schuh, E. Reiger, E. Kaxiras, J. Arbiol, and A. Fontcuberta i Morral, *Direct correlation of crystal structure and*

optical properties in wurtzite/zinc-blende GaAs nanowire heterostructures, Physical Review B **83** (2011), 045303.

[58] H. Huang, S. Mao, H. Feick, H. Yan, Y. Wu, H. Kind, E. Weber, R. Russo, and P. Yang, *Room-temperature ultraviolet nanowire nanolasers*, Science **292** (2001), 1897.

[59] ID01 beamline, `www.esrf.eu/UsersAndScience/Experiments/StructMaterials/ID01/`.

[60] K. Ikejiri, J. Noborisaka, S. Hara, J. Motohisa, and T. Fukui, *Mechanism of catalyst-free growth of GaAs nanowires by selective area MOVPE*, Journal Of Crystal Growth **298** (2007), 616.

[61] K. Ikejiri, T. Sato, H. Yoshida, K. Hiruma, J. Motohisa, S. Hara, and T. Fukui, *Growth characteristics of GaAs nanowires obtained by selective area metal-organic vapour-phase epitaxy*, Nanotechnology **19** (2008), 265604.

[62] H. Ishikawa, K. Yamamoto, T. Egawa, T. Soga, T. Jimbo, and M. Umeno, *Thermal stability of GaN on (111) Si substrate*, Journal Of Crystal Growth **189-190** (1998), 178.

[63] F. Jabeen, G. Bulgarini, N. Akopian, G. Patriarche, V. Zwiller, and J. C. Harmand, *Catalyst influence on morphology, crystal structure and optical properties of GaAs/AlGaAs core-shell nanowires*, 6th Nanowire Growth Workshop, St. Petersburg, Russia, June 4-6, 2012.

[64] U. Jahn, J. Lähnemann, C. Pfüller, O. Brandt, S. Breuer, B. Jenichen, M. Ramsteiner, L. Geelhaar, and H. Riechert, *Luminescence of GaAs nanowires consisting of wurtzite and zinc-blende segments*, Physical Review B **85** (2012), 045323.

[65] K. Jefimovs, O. Bunk, F. Pfeiffer, D. Grolimund, J. F. van der Veen, and C. David, *Fabrication of Fresnel zone plates for hard X-rays*, Microelectronic Engineering **84** (2007), 1467.

[66] V. M. Kaganer, M. Wölz, O. Brandt, L. Geelhaar, and H. Riechert, *X-ray diffraction profiles from axial nanowire heterostructures*, Physical Review B **83** (2011), 245321.

[67] T. I. Kamins, X. Li, R. Stanley Williams, and X. Liu, *Growth and structure of chemically vapor deposited Ge nanowires on Si substrates*, Nano Letters **4** (2004), 503.

[68] K. L. Kavanagh, *Misfit dislocations in nanowire heterostructures*, Semiconductor Science and Technology **25** (2010), 024006.

[69] K. L. Kavanagh, J. Salfi, I. Savelyev, M. Blumin, and H. E. Ruda, *Transport and strain relaxation in wurtzite InAs-GaAs core-shell heterowires*, Applied Physics Letters **98** (2011), 152103.

[70] K. L. Kavanagh, I. Saveliev, M. Blumin, G. Swadener, and H. E. Ruda, *Faster radial strain relaxation in InAs–GaAs core–shell heterowires*, Journal of Applied Physics **111** (2012), 044301.

[71] M. Keplinger, T. Mårtensson, J. Stangl, E. Wintersberger, B. Mandl, D. Kriegner, V. Holý, G. Bauer, K. Deppert, and L. Samuelson, *Structural investigations of core-shell nanowires using grazing incidence x-ray diffraction*, Nano Letters **9** (2009), 1877.

[72] Charles Kittel, *Einführung in die Festkörperphysik*, Oldenbourg, München, (2002), ISBN: 3486272195.

[73] Konrad Kopitzki, *Einführung in die Festkörperphysik*, Teubner, Stuttgart, (2004), ISBN: 3519430835.

[74] D. Kriegner, C. Panse, B. Mandl, K. A. Dick, M. Keplinger, J. M. Persson, P. Caroff, D. Ercolani, L. Sorba, F. Bechstedt, J. Stangl, and G. Bauer, *Unit cell structure of crystal polytypes in InAs and InSb nanowires*, Nano Letters **11** (2011), 1483.

[75] P. Krogstrup, R. Popovitz-Biro, E. Johnson, M. H. Madsen, J. Nygård, and H. Shtrikman, *Structural phase control in self-catalyzed growth of GaAs nanowires on silicon (111)*, Nano Letters **10** (2010), 4475.

[76] P. Krogstrup, J. Yamasaki, C. B. Sorensen, E. Johnson, J. B. Wagner, R. Pennington, M. Aagesen, N. Tanaka, and J. Nygård, *Junctions in axial III-V heterostructure nanowires obtained via an interchange of group III elements*, Nano Letters **9** (2009), 3689.

[77] M. W. Larsson, J. B. Wagner, M. Wallin, P. Hakansson, L. E. Froberg, L. Samuelson, and L. R. Wallenberg, *Strain mapping in free-standing heterostructured wurtzite InAs/InP nanowires*, Nanotechnology **18** (2007), 015504.

[78] X. Li, T. Ono, Y. Wang, and M. Esashi, *Ultrathin single-crystalline-silicon cantilever resonators: Fabrication technology and significant specimen size effect on Young's modulus*, Applied Physics Letters **83** (2003), 3081.

[79] Otfried Madelung, *Semiconductors: Data handbook*, Springer, Berlin, Heidelberg, (2004), ISBN: 3540404880.

[80] S. Marchesini, H. He, H.N. Chapman, S.P. Hau-Riege, A. Noy, M. R. Howells, U. Weierstall, and J.C.H. Spence, *X-ray image reconstruction from a difraction pattern alone*, Physical Review B **68** (2003), 140101(R).

[81] S. O. Mariager, *Structure and dynamics of crystalline nano-systems*, Ph.D. thesis, (2010), Niels Bohr Institute, University of Copenhagen.

[82] S. O. Mariager, D. Khakhulin, H. T. Lemke, K. S. Kjaer, L. Guerin, L. Nuccio, C. B. Sorensen, M. M. Nielsen, and R. Feidenhans'l, *Direct observation of acoustic oscillations in InAs nanowires*, Nano Letters **10** (2010), 2461.

[83] S. O. Mariager, S. L. Lauridsen, A. Dohn, N. Bovet, C. B. Sorensen, C. M. Schleputz, P. R. Willmott, and R. Feidenhans'l, *High-resolution three-dimensional reciprocal-space mapping of InAs nanowires*, Journal Of Applied Crystallography **42** (2009), 369.

[84] S. O. Mariager, S. L. Lauridsen, C. B. Sorensen, A. Dohn, P. R. Willmott, J. Nygard, and R. Feidenhans'l, *Stages in molecular beam epitaxy growth of GaAs nanowires studied by x-ray diffraction*, Nanotechnology **21** (2010), 115603.

[85] S. O. Mariager, C. B. Sorensen, M. Aagesen, J. Nygard, R. Feidenhans'l, and P. R. Willmott, *Facet structure of GaAs nanowires grown by molecular beam epitaxy*, Applied Physics Letters **91** (2007), 083106.

[86] R. M. Martin, *Relation between elastic tensors of wurtzite and zinc-blende structure materials*, Physical Review B **6** (1972), 4546.

[87] R.M. Martin, *Elastic properties of ZnS structure semiconductors*, Physical Review B **1** (1970), 4005.

[88] F. Mastropietro, D. Carbone, A. Diaz, J. Eymery, A. Sentenac, T. H. Metzger, V. Chamard, and V. Favre-Nicolin, *Coherent x-ray wavefront reconstruction of a partially illuminated Fresnel zone plate*, Optics Express **19** (2011), 19223.

[89] MATLAB, `www.mathworks.de/products/matlab/`.

[90] J. W. Matthews and A. E. Blakeslee, *Defects in epitaxial multilayers: I. misfit dislocations*, Journal Of Crystal Growth **27** (1974), 118.

[91] M. I. McMahon and R. J. Nelmes, *Observation of a wurtzite form of gallium arsenide*, Physical Review Letters **95** (2005), 215505.

[92] M. E. Messing, J. Wong-Leung, Z. Zanolli, H. J. Joyce, H. H. Tan, Q. Gao, L. R. Wallenberg, J. Johansson, and C. Jagadish, *Growth of straight InAs-on-GaAs nanowire heterostructures*, Nano Letters **11** (2011), 3899.

[93] J. Miao, P. Charalambous, J. Kirz, and D. Sayre, *Extending the methodology of X-ray crystallography to allow imaging of micrometre-sized non-crystalline specimens*, Nature **400** (1999), 342.

[94] Dennis Mills, *Third-generation hard x-ray synchrotron radiation sources : source properties, optics, and experimental techniques*, Wiley, New York, (2002), ISBN: 0471314331.

[95] A. A. Minkevich, E. Fohtung, T. Slobodskyy, M. Riotte, D. Grigoriev, M. Schmidbauer, A. C. Irvine, V. Novák, V. Holý, and T. Baumbach, *Selective coherent x-ray diffractive imaging of displacement fields in (Ga,Mn)As/GaAs periodic wires*, Physical Review B **84** (2011), 054113.

[96] C. Mocuta, J. Stangl, K. Mundboth, T. H. Metzger, G. Bauer, I. A. Vartanyants, M. Schmidbauer, and T. Boeck, *Beyond the ensemble average: X-ray microdiffraction analysis of single SiGe islands*, Physical Review B **77** (2008), 245425.

[97] A. M. Morales and C. M. Lieber, *A laser ablation method for the synthesis of crystalline semiconductor nanowires*, Science **279** (1998), 208.

[98] M. Morita, T. Ohmi, E. Hasegawa, M. Kawakami, and K. Suma, *Control factor of native oxide growth on silicon in air or in ultrapure water*, Applied Physics Letters **55** (1989), 562.

[99] M. C. Newton, S. J. Leake, R. Harder, and I. K. Robinson, *Three-dimensional imaging of strain in a single ZnO nanorod*, Nature Materials **9** (2010), 120.

[100] John F. Nye, *Physical properties of crystals : their representation by tensors and matrices*, Oxford University Press, New York, (1985), ISBN: 0198511655.

[101] P. Offermans, M. Crego-Calama, and S. H. Brongersma, *Gas detection with vertical InAs nanowire arrays*, Nano Letters **10** (2010), 2412.

[102] B. J. Ohlsson, M. T. Bjork, M. H. Magnusson, K. Deppert, L. Samuelson, and L. R. Wallenberg, *Size-, shape-, and position-controlled GaAs nanowhiskers*, Applied Physics Letters **79** (2001), 3335.

[103] H. Paetzelt, V. Gottschalch, J. Bauer, G. Benndorf, and G. Wagner, *Selective-area growth of GaAs and InAs nanowires-homo- and heteroepitaxy using* SiN_x *templates*, Journal Of Crystal Growth **310** (2008), 5093.

[104] Hendrik Paetzelt, *private communication.*

[105] David Paganin, *Coherent x-ray optics*, Oxford University Press, New York, (2006), ISBN: 0198567286.

[106] C. Panse, D. Kriegner, and F. Bechstedt, *Polytypism of GaAs, InP, InAs, and InSb: An ab initio study*, Physical Review B **84** (2011), 075217.

[107] M. A. Pfeifer, G. J. Williams, I. A. Vartanyants, R. Harder, and I. K. Robinson, *Three-dimensional mapping of a deformation field inside a nanocrystal*, Nature **442** (2006), 63.

[108] U. Pietsch, V. Holý, and T. Baumbach, *High-resolution x-ray scattering: From thin films to lateral nanostructures*, Springer, New York, (2004), ISBN: 0387400923.

[109] S. Plissard, K. A. Dick, G. Larrieu, S. Godey, A. Addad, X. Wallart, and P. Caroff, *Gold-free growth of GaAs nanowires on silicon: arrays and polytypism*, Nanotechnology **21** (2010), 385602.

[110] S. Plissard, G. Larrieu, X. Wallart, and P. Caroff, *High yield of self-catalyzed GaAs nanowire arrays grown on silicon via gallium droplet positioning*, Nanotechnology **22** (2011), 275602.

[111] C. Ponchut, J. Clément, J. M. Rigal, E. Papillon, J. Vallerga, D. LaMarra, and B. Mikulec, *Photon-counting x-ray imaging at kilohertz frame rates*, Nucl. Instrum. Meth. A **576** (2007), 109.

[112] C. Ponchut, J. M. Rigal, J. Clément, E. Papillon, A. Homs, and S. Petitdemange, *MAXIPIX, a fast readout photon-counting X-ray area detector for synchrotron applications*, Journal of Instrumentation **6** (2011), C01069.

[113] R. Popovitz-Biro, A. Kretinin, P. Von Huth, and H. Shtrikman, *InAs/GaAs core-shell nanowires*, Crystal Growth & Design **11** (2011), 3858.

[114] M. Povolotskyi and A. D. Carlo, *Elasticity theory of pseudomorphic heterostructures grown on substrates of arbitrary thickness*, Journal of Applied Physics **100** (2006), 063514.

[115] E. Price, *International tables for crystallography volume C: Mathematical, physical and chemical tables*, Springer Netherlands, (2004), ISBN: 9781402019005.

[116] C. Pryor, J. Kim, L. W. Wang, A. J. Williamson, and A. Zunger, *Comparison of two methods for describing the strain profiles in quantum dots*, Journal of Applied Physics **83** (1998), 2548.

[117] M. C. Putnam, M. A. Filler, B. M. Kayes, M. D. Kelzenberg, Y. Guan, N. S. Lewis, J. M. Eiler, and H. A. Atwater, *Secondary ion mass spectrometry of vapor-liquid-solid grown, Au-catalyzed, Si wires*, Nano Letters **8** (2008), 3109.

[118] S. Raychaudhuri and E. T. Yu, *Calculation of critical dimensions for wurtzite and cubic zinc blende coaxial nanowire heterostructures*, Journal of Vacuum Science & Technology B **24** (2006), 2053.

[119] ______, *Critical dimensions in coherently strained coaxial nanowire heterostructures*, Journal of Applied Physics **99** (2006), 114308.

[120] T. Rieger, S. Heiderich, S. Lenk, M. I. Lepsa, and D. Grützmacher, *Ga-assisted MBE growth of GaAs nanowires using thin HSQ layer*, Journal Of Crystal Growth **353** (2012), 39.

[121] T. Rieger, M. Luysberg, T. Schäpers, D. Grützmacher, and M. I. Lepsa, *MBE growth of GaAs/InAs core-shell nanowires and fabrication of InAs nanotubes*, submitted, 2012.

[122] I. Robinson and R. Harder, *Coherent X-ray diffraction imaging of strain at the nanoscale*, Nature Materials **8** (2009), 291.

[123] I. K. Robinson, *Crystal truncation rods and surface roughness*, Physical Review B **33** (1986), 3830.

[124] I. K. Robinson, I. A. Vartanyants, G. J. Williams, M. A. Pfeifer, and J. A. Pitney, *Reconstruction of the shapes of gold nanocrystals using coherent x-ray diffraction*, Physical Review Letters **87** (2001), 195505.

[125] Martin Schmidbauer, *X-ray diffuse scattering from self-organized mesoscopic semiconductor structures*, Springer, Berlin New York, (2004), ISBN: 3540201793.

[126] B. Schmitt, Ch. Brönnimann, E. F. Eikenberry, F. Gozzo, C. Hörmann, R. Horisberger, and B. Patterson, *Mythen detector system*, Nucl. Instrum. Meth. A **501** (2003), 267.

[127] L. Schubert, P. Werner, N. D. Zakharov, G. Gerth, F. M. Kolb, L. Long, U. Gosele, and T. Y. Tan, *Silicon nanowhiskers grown on <111>Si substrates by molecular-beam epitaxy*, Applied Physics Letters **84** (2004), 4968.

[128] O. H. Seeck, C. Deiter, K. Pflaum, F. Bertam, A. Beerlink, H. Franz, J. Horbach, H. Schulte-Schrepping, B. M. Murphy, M. Greve, and O. Magnussen, *The high-resolution diffraction beamline P08 at PETRA III*, Journal of Synchrotron Radiation **19** (2012), 30.

[129] M. M. Seibert, T. Ekeberg, F. R. N. C. Maia, M. Svenda, J. Andreasson, O. Jonsson, D. Odic, B. Iwan, A. Rocker, and D. et al. Westphal, *Single mimivirus particles intercepted and imaged with an X-ray laser*, Nature **470** (2011), 78.

[130] V. A. Shchukin and D. Bimberg, *Spontaneous ordering of nanostructures on crystal surfaces*, Reviews of Modern Physics **71** (1999), 1125.

[131] H. Shtrikman, R. Popovitz-Biro, A. Kretinin, L. Houben, M. Heiblum, M. Bukala, M. Galicka, R. Buczko, and P. Kacman, *Method for suppression of stacking faults in wurtzite III-V nanowires*, Nano Letters **9** (2009), 1506.

[132] A. Snigirev, V. Kohn, I. Snigireva, and B. Lengeler, *A compound refractive lens for focusing high-energy X-rays*, Nature **384** (1996), 49.

[133] D. Spirkoska, J. Arbiol, A. Gustafsson, S. Conesa-Boj, F. Glas, I. Zardo, M. Heigoldt, M. H. Gass, A. L. Bleloch, S. Estrade, M. Kaniber, J. Rossler, F. Peiro, J. R. Morante, G. Abstreiter, L. Samuelson, and A. Fontcuberta i Morral, *Structural and optical properties of high quality zinc-blende/wurtzite GaAs nanowire heterostructures*, Physical Review B **80** (2009), 245325.

[134] M. Tchernycheva, J. C. Harmand, G. Patriarche, L. Travers, and G. E. Cirlin, *Temperature conditions for GaAs nanowire formation by Au-assisted molecular beam epitaxy*, Nanotechnology **17** (2006), 4025.

[135] C. Thelander, P. Agarwal, S. Brongersma, J. Eymery, L.F. Feiner, A. Forchel, M. Scheffler, W. Riess, B.J. Ohlsson, U. Gösele, and L. Samuelson, *Nanowire-based one-dimensional electronics*, Materials Today **9** (2006), 28.

[136] K. Tomioka, Y. Kobayashi, J. Motohisa, S. Hara, and T. Fukui, *Selective-area growth of vertically aligned GaAs and GaAs/AlGaAs core-shell nanowires on Si(111) substrate*, Nanotechnology **20** (2009), 145302.

[137] K. Tomioka, J. Motohisa, S. Hara, and T. Fukui, *Control of InAs nanowire growth directions on Si*, Nano Letters **8** (2008), 3475.

[138] K. Tomioka, J. Motohisa, S. Hara, K. Hiruma, and T. Fukui, *GaAs/AlGaAs core multishell nanowire-based light-emitting diodes on Si*, Nano Letters **10** (2010), 1639.

[139] K. Tomioka, T. Tanaka, S. Hara, K. Hiruma, and T. Fukui, *Nanowires on Si substrate: Selective-area growth and device applications*, Selected Topics in Quantum Electronics, IEEE Journal of **17** (2011), 1112.

[140] I. A. Vartanyants and I. K. Robinson, *Partial coherence effects on the imaging of small crystals using coherent x-ray diffraction*, Journal of Physics: Condensed Matter **13** (2001), 10593.

[141] B. A. Wacaser, K. Deppert, L. S. Karlsson, L. Samuelson, and W. Seifert, *Growth and characterization of defect free GaAs nanowires*, Journal Of Crystal Growth **287** (2006), 504.

[142] R. S. Wagner and W. C. Ellis, *Vapor-liquid-solid mechanism of single crystal growth*, Applied Physics Letters **4** (1964), 89.

[143] Y. Wang, V. Schmidt, S. Senz, and U. Gosele, *Epitaxial growth of silicon nanowires using an aluminium catalyst*, Nature Nanotechnology **1** (2006), 186.

[144] Y. B. Wang, L. F. Wang, H. J. Joyce, Q. Gao, X. Z. Liao, Y. W. Mai, H. H. Tan, J. Zou, S. P. Ringer, H. J. Gao, and C. Jagadish, *Super deformability and Young's modulus of GaAs nanowires*, Advanced Materials **23** (2011), 1356.

[145] B. E. Warren, *X-ray diffraction*, Dover Publications, New York, (1990), ISBN: 0486663175.

[146] W. J. Williams, M. A. Pfeifer, I. A. Vartanyants, and I. K. Robinson, *Three-dimensional imaging of microstructure in Au nanocrystals*, Physical Review Letters **90** (2003), 175501.

[147] H. Yamaguchi, J. G. Belk, X. M. Zhang, J. L. Sudijono, M. R. Fahy, T. S. Jones, D. W. Pashley, and B. A. Joyce, *Atomic-scale imaging of strain relaxation via misfit dislocations in highly mismatched semiconductor heteroepitaxy: InAs/GaAs(111)A*, Physical Review B **55** (1997), 1337.

[148] R. Yan, D. Gargas, and P. Yang, *Nanowire photonics*, Nature Photonics **3** (2009), 569.

[149] P. Yang, R. Yan, and M. Fardy, *Semiconductor nanowire: What's next?*, Nano Letters **10** (2010), 1529.

[150] H. Yao, G. Yun, N. Bai, and J. Li, *Surface elasticity effect on the size-dependent elastic property of nanowires*, Journal of Applied Physics **111** (2012), 083506.

[151] H. Ye, P. Lu, Z. Yu, Y. Song, D. Wang, and S. Wang, *Critical thickness and radius for axial heterostructure nanowires using finite-element method*, Nano Letters **9** (2009), 1921.

[152] X. Zhang, V. G. Dubrovskii, N. V. Sibirev, and X. Ren, *Analytical study of elastic relaxation and plastic deformation in nanostructures on lattice mismatched substrates*, Crystal Growth & Design **11** (2011), 5441.

[153] G. Zheng, F. Patolsky, Y. Cui, W. U. Wang, and C. M. Lieber, *Multiplexed electrical detection of cancer markers with nanowire sensor arrays*, Nature Biotechnology **23** (2005), 1294.

Acknowledgements

It turns out that this is one of the most difficult chapters to write in a thesis, and I decided to keep this short.

I am grateful to Prof. Dr. Ullrich Pietsch, for his guidance and constant support through all the years.
I thank all my colleagues, friends and all people with whom I worked in the past years, and who contributed to the results by measurements, sample preparations, assistance and discussions and helped making this thesis possible. In particular Anton Davydok, who shared most of the long days at the synchrotrons with me.

And I thank Katharina, for her love and patience.

Parts of this work have been supported by the Deutsche Forschungsgemeinschaft (DFG) under grant Pi217/38 and Ge2224/2.